(Quantum-) critical dynamics of magnetoelectric materials

I n a u g u r a l - D i s s e r t a t i o n

zur

Erlangung des Doktorgrades

der Mathematisch-Naturwissenschaftlichen Fakultät

der Universität zu Köln

vorgelegt von

Christoph Grams
aus Bergisch Gladbach

Köln, 2016

Berichterstatter:	Prof. Dr. Joachim Hemberger Prof. Dr. Markus Braden
Vorsitzender der Prüfungskommission:	Prof. Dr. Simon Trebst
Tag der mündlichen Prüfung:	25.11.2015

Contents

List of symbols

$\log(x)$	: natural logarithm
$\log_{10}(x)$	: common logarithm
$PV\int$	: Cauchy principal value of an integral
ν	: ordinary/technical frequency
$\omega = 2\pi\nu$	: angular/radial frequency
$\underline{Z} = Z' + \mathrm{i}Z''$	: complex impedance
$\underline{\varepsilon} = \varepsilon' - \mathrm{i}\varepsilon''$	: complex dielectric function
ε_∞	: contribution to ε' from processes at higher frequencies
$C_0 = \varepsilon_0 \cdot A/d$	: geometric capacitance with area A and thickness d
P_{sw}, P_{sat}, P_{rem}	: switchable, saturation, and remanent polarization
E_{ac}	: amplitude of an electric ac field
E_{crcv}	: coercive field
M	: magnetization
$H = H_{\mathrm{external}}$	: external magnetic field strength
$H_{\mathrm{i}} = H_{\mathrm{internal}} = H - DM$	: internal magnetic field strength with demagnetization factor D
$B_{\mathrm{i}} = B_{\mathrm{internal}} = \mu_0(H_{\mathrm{i}} + M)$	: magnetic flux density
$k_{\mathrm{B}} = 1.380\,62 \times 10^{-23}\,\mathrm{J\,K^{-1}}$	: Boltzmann constant
$\varepsilon_0 = 8.854 \times 10^{-12}\,\mathrm{A\,s\,V^{-1}\,m^{-1}}$	: vacuum permittivity
$\mu_0 = 4\pi \times 10^{-7}\,\mathrm{V\,s\,A^{-1}\,m^{-1}}$	: vacuum permeability

Introduction

Magnetoelectrics are materials characterized by a coupling between their magnetic and dielectric properties, namely magnetization M and polarization P. This coupling can be of different forms and origins, some of which will be explained in the introductory chapters of this thesis.

Merely the existence of such a connection between two different physical properties offers, on top of purely academic interest in the nature of the coupling, many interesting possibilities for applications. The most often named idea concerning magnetoelectric materials is data storage. Here the advantages of materials combining magnetic and electric properties are easily understood. For all mobile devices, laptop computers, mobile phones, etc., their battery life, measured in current $\cdot$ time, is one of their key features. These devices also have a common capacity, the need to store data. Because a current is required in order to write or read magnetically stored data this is very energy consuming when using conventional magnetic storage media. But magnetic storage also has a very important benefit: the lifetime of magnetic domains is much larger compared to electric domains and the stored data is retained for a very long time.

Today storage devices already use the giant magneto resistance effect where the resistance of a material depends on the relative magnetization direction of two ferromagnetic layers separated by a non-magnetic spacer. Here the data is still stored via arrangement of magnetic domains using a high current, but reading the information can be done by measuring the resistance, which only requires a very small current.

Magnetoelectric and multiferroic materials would improve this advantage even further, because they remove the need for a current to save the data. A high electric field E could be used to store data by switching the magnetization M while a lower electric field would we sufficient to read the information. Due to the coupling between polarization and magnetization the retention time in this case would be similar to purely magnetic storage.

But not only the potential to store data cheap, *i.e.* without investing much battery current, but also the time required to store any meaningful amount of data is important. This is where the most prominent measurement technique in the work comes in, the dielectric spectroscopy. Here electric ac voltages of different frequencies and amplitudes can be applied to the sample while measuring its response. This can be used to find the maximum frequency where the polarization of the sample can be switched with a given voltage and thereby measuring the possible write speed of the materials.

The aim of this thesis was not a specific application of magnetoelectric materials but instead the focus is on purely academic aspects of the fluctuation dynamics in the critical regime close to phase transitions. Most of the materials in this work only gain their magnetoelectric character at very low temperatures, where in this case "very low" means temperatures well below 10 K. The truly novel and unexpected phenomena can only be observed at temperatures even lower than this by more than one order of magnitude.

The required low temperature itself was one of the most challenging aspects

during the experimental work presented in this thesis. Additionally, measurements of the dielectric properties at frequencies of the order of 100 MHz and higher are subject to many error sources, for example the change of the cable length and resistivity while cooling. Their sensitivity towards this undesired effects only increases when working towards higher frequencies.

This work was supported by the DFG through SFB 608, research grant HE-3219/2-1, and the "Quantum Matter and Materials" (QM^2) Center of Excellence at the University of Cologne.

1 Basics

On the next pages the basic concepts that are the foundation of this work are briefly introduced. Mostly a short review is given, only for few topics some mathematical deliberations are presented that will be important for the evaluation of the experimental data.

Contents

1.1 Polarization dynamics

In general three different mechanisms of electrical polarization are observed in crystals. The origins of these processes are, in the order of their typical resonance frequencies:

- electronic - caused by the shifting of the electrons with respect to the atomic core
- ionic - movement of oppositely charged ions in different directions with optical phonons
- orientation - shift of the orientation of existing dipoles

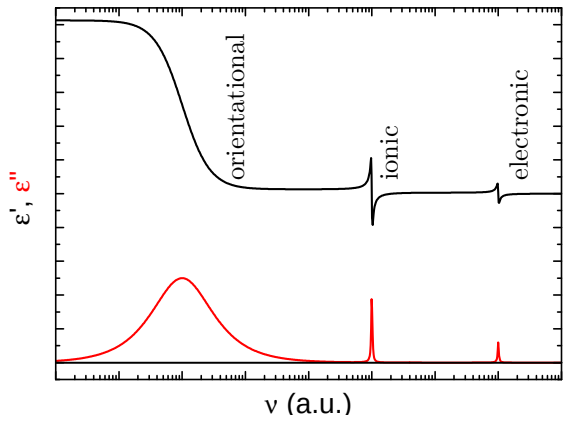

Figure 1.1: Polarization processes in spectroscopic measurements.
Schematic representation of different polarization processes typically observed with spectroscopic measurements.

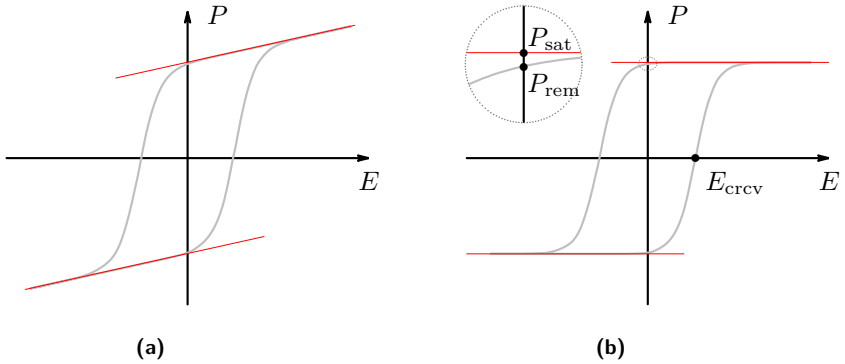

Figure 1.2: Sketch of a hysteresis loop.
(a) A typical hysteresis loop as could be measured in a ferroelectric material. (b) The same hysteresis loop without the slope caused by ε' . In the inset the distinction between P_{sat} and P_{rem} can be seen more clearly.

Figure 1.1 shows a schematic representation of the previously mentioned mechanisms of polarization dynamics. The relaxational processes associated with shifts of dipol orientation are typically the slowest mechanism observed and are characterized by high damping. Faster are ionic and electronic contributions but for the frequency range discussed in this thesis, 10 GHz and below, they cause only a frequency-independent offset in the permittivity ε' that is called ε_∞.

1.1.1 Hysteresis loops

Typically, electrical polarization is observed by either measuring the pyroelectric current $P(T)$ or, at constant temperature, the electric-field dependence of the polarization $P(E)$. In the scope of this section the general form of the latter curves is discussed as some knowledge of the terminology regarding hysteresis loops is required for the discussion of the experimental results in chapters 4 and following.

A generic hysteresis loop as could have been measured in a ferroelectric material is shown in figure 1.2a. Before analyzing the actual hysteresis loop the slope observed in the saturation regime has to be taken into account. This slope is

caused by the dielectric constant ε' of the material and the latter can be calculated from the slope s in the linear regime on both sides of the curve using

$$s = \frac{\mathrm{d}P}{\mathrm{d}E} = \chi \cdot \varepsilon_0 = (\varepsilon' - 1) \cdot \varepsilon_0. \tag{1.1}$$

After subtracting this slope the hysteresis loop has the more common form shown in figure 1.2b where some points are of special interest. First the saturation polarization P_{sat}, *i.e.* the maximum value of P realized for strong electric fields. This can be found from the P-intercept of fits in the linear regime. Slightly lower than P_{sat} is the remanent polarization P_{rem} that denotes the polarization value measured at $E = 0$ after reaching the saturation polarization. On the electric-field axis the coercive field E_{crcv} is the field value that is required to suppress the remanent polarization, *i.e.* $P(E_{\mathrm{crcv}}) = 0$. This can be understood as a measure of the stability of the ferroelectric phase against perturbations by *e.g.* temperature induced disorder.

1.1.2 Relaxations

Opposed to both electronic and ionic polarization the orientation polarization requires the existence of permanent dipole moments that try to reorient in the applied electric ac field due to a (small) time-dependent inhomogeneity induced into their potential. This leads to a time dependence of the polarization that is driven by the difference between the polarization $P(t)$ at time t and the equilibrium polarization $P_\infty(t)$ that would be observed if the system were to stay at the current voltage for infinite time:

$$\frac{\mathrm{d}P(T)}{\mathrm{d}t} = -\frac{P(t) - P_\infty(t)}{\tau} \tag{1.2}$$

The relaxation time τ of the thermally activated reorientation can be given as

$$\tau = \tau_0 \mathrm{e}^{\frac{U_\mathrm{b}}{k_\mathrm{B} T}} \tag{1.3}$$

where τ_0 is the time between two tries to change the orientation by passing the potential barrier U_b.

1.1.3 Ferroelectric phase transitions

Ferroelectricity can be induced by two different mechanisms. The order-disorder transition where the polarization is present in both the ferroelectric and the paraelectic phase and only its long-range order is lost when crossing T_c, resulting in a vanishing net polarization. Secondly, the displacive phase transition where the shifting of two sublattices with differently charged ions in opposite directions creates net polarization during this structural phase transition.

Critical slowing down / soft phonon modes

Ionic polarization can only be observed with low frequencies close to a displacive (anti-)ferroelectric phase transition when the transverse optical phonon branch slows down into the measurable frequency range.

This behavior is called critical slowing down and the corresponding phonon mode is called soft [5]. In terms of a description with critical exponents,

$$1/\tau \propto 2\pi\nu_\mathrm{p} \propto |T - T_\mathrm{c}|^\gamma$$

this behavior is described with a positive exponent $\gamma > 0$.

Magnetic field as control parameter

If a magneto-electric coupling exists a ferroelectric phase transition can also be driven by the magnetic field because in this case the energy barrier U_b in equation (1.3) depends on the magnetic field. Changing the magnetic field at constant temperature now has essentially the same influence on τ as the temperature at constant - or zero - magnetic field. An example for this behavior is the multiferroic $MnWO_4$ where the critical dynamics has recently been studied [64, 63]. Here it was shown that the critical dynamics at the phase transition are independent of the control parameter used to drive the transition.

1.2 (Non-)Linear response theory

The interaction of electromagnetic waves with matter can be described theoretically as perturbations and lead to the response functions $\underline{\varepsilon}(k,\omega)$ and $\underline{\chi}(k,\omega)$ that depend on the momentum and the frequency of the electromagnetic wave.

As the highest frequencies used for the spectroscopic measurements presented in this work are in the GHz range the corresponding wavelength[1] is clearly much larger than the atomic length scale of any sample. Thus, the momentum dependence can be ignored and k is assumed to be zero for the following deliberations. Furthermore, using specific geometries of the sample holder it can be selected whether the electric or magnetic component couples to the sample. Therefore, it is sufficient to consider this argument only for either $\underline{\varepsilon}(\omega)$ or $\underline{\chi}(\omega)$, here the latter will not be discussed in detail.

Depending on the strength of the perturbation, in this case the amplitude of the electric ac field, this description can be done in two limits that will be described in the following two sections.

1.2.1 Linear response theory

If the applied electrical field E is small enough the polarization $P(E)$ can be described as a linear function of E: $P(E) \propto E$ and terms of higher order in E can be ignored. In this case the dielectric constant is independent of the actual strength E of the electric field: $\underline{\varepsilon} = \mathrm{d}P/\mathrm{d}E * 1/\varepsilon_0 + 1$.

1.2.2 Non-linear response theory

Once the applied electrical field is high enough a linear description of $P(E)$ is insufficient and the higher order terms have to be taken into account:

$$P(E) = \alpha_1\varepsilon_0 E + \alpha_2\varepsilon_0 E^2 + \alpha_3\varepsilon_0 E^2 + ... = \varepsilon_0 \sum_{n=1}^{\infty} a_n E^n.$$

When applying an oscillating electrical field $E(t) = E_\mathrm{ac}\sin(\omega t)$ the expression for the polarization can be written as

[1] 10 GHz translate to a wavelength of 29.98 mm ≈ 3 cm in vacuum.

$$P(t) = \varepsilon_0 E_{\mathrm{ac}} \sum_{n=1}^{\infty} a_n E_{\mathrm{ac}}^{(n-1)} \sin^n(\omega t) = \varepsilon_0 E_{\mathrm{ac}} \sum_{n=1}^{\infty} a_n E_{\mathrm{ac}}^{(n-1)} \frac{\mathrm{i}^n}{2^n} \left(\mathrm{e}^{-\mathrm{i}\omega t} + \mathrm{e}^{\mathrm{i}\omega t}\right)^n .$$

Using the binomial expansion this equation can be rewritten as

$$\begin{aligned} P(t) &= \varepsilon_0 E_{\mathrm{ac}} \sum_{n=1}^{\infty} a_n \frac{\mathrm{i}^n E_{\mathrm{ac}}^{(n-1)}}{2^n} \sum_{k=0}^{n} \binom{n}{k} \mathrm{e}^{-\mathrm{i}(n-k)\omega t + \mathrm{i}k\omega t} \\ &= \varepsilon_0 E_{\mathrm{ac}} \sum_{n=1}^{\infty} a_n \frac{\mathrm{i}^{(n-1)} E_{\mathrm{ac}}^{(n-1)}}{2^n} \sum_{k=0}^{n} \binom{n}{k} \mathrm{i}\mathrm{e}^{-\mathrm{i}(n-2k)\omega t}. \end{aligned} \tag{1.4}$$

Due to the symmetry of the binomial coefficients and the exponential function[2] the latter sum can be reduced to half its elements:

$$P(t) = \mathrm{Re}\left[\varepsilon_0 E_{\mathrm{ac}} \sum_{n=1}^{\infty} a_n \frac{\mathrm{i}^{(n-1)} E_{\mathrm{ac}}^{(n-1)}}{2^n} \sum_{k=0}^{<n/2} 2\binom{n}{k} \mathrm{i}\mathrm{e}^{-\mathrm{i}(n-2k)\omega t}\right] + P_{\mathrm{even}}$$

where the time-independent contributions for $k = n/2$ from even n are combined into P_{even} and only the real part is taken into account.

From this equation two things can be derived. First, contributions from even and odd n do not mix, as only multiples of 2 are subtracted from n. Secondly the contributions for even n produce a contribution that is independent of ωt when $k = {}^{n}/_{2}$.

Sorting the elements of the summation by the multiple $(n - 2k)$ of ω and combining the corresponding prefactors into a common factor called $\underline{\varepsilon}_n$ while keeping in mind that only the real part of the polarization is relevant leads to

$$\begin{aligned} P(t) &= \mathrm{Re}\left[\varepsilon_0 E_{\mathrm{ac}} \sum_{n=1}^{\infty} \underline{\varepsilon}_n \mathrm{i}\mathrm{e}^{-\mathrm{i}n\omega t}\right] \\ &= \varepsilon_0 E_{\mathrm{ac}} \sum_{n=1}^{\infty} \varepsilon'_n \sin(n\omega t) - \varepsilon''_n \cos(n\omega t). \end{aligned} \tag{1.5}$$

Thus the hysteresis curve of the sample can be evaluated by measuring the polarization for integer multiples of the excitation frequency.

As hysteresis curves in general are centered around the point of origin and no offset is observed this indicates that the even contributions of this expansion are expected to be small or vanish. This is also consistent with the point symmetry of the $P(E)$ curves, $P(E) = -P(-E)$, that is consistent only with the symmetry observed for odd exponents in E.

For the model case of a perfectly rectangular hysteresis loop it was argued in [63] that the first order harmonic contributions, ε'_1 and ε''_1, can be used to calculate both the switchable polarization P_{sw} and the coercive field E_{crcv}:

[2] This argument can be found in the appendix A.1 on page 113 in more detail.

$$|\Delta\varepsilon_1| = \sqrt{(\varepsilon'_1 - \varepsilon_\infty)^2 + \varepsilon''^2_1}$$

$$P_{\mathrm{sw}} = \frac{\pi}{4}\varepsilon_0 |\Delta\varepsilon_1| E_{\mathrm{ac}} \tag{1.6}$$

$$E_{\mathrm{crcv}} = \frac{\varepsilon''_1}{|\Delta\varepsilon_1|} E_{\mathrm{ac}} \tag{1.7}$$

Using this relations with measured data will provide a good approximation of both P_{sw} and E_{crcv} as long as $E_{\mathrm{ac}} > E_{\mathrm{crcv}}$.

1.3 Lorentz oscillator model

A simple model for the description of the polarization mechanisms introduced in section 1.1 is the Lorentz[3] oscillator model. This standard model of electrical polarization can be found in many textbooks, *e.g.* [28]. It describes the frequency-dependent permittivity as a sum over many resonant processes:

$$\underline{\varepsilon} = 1 + \sum_s \frac{n_s e^2}{\varepsilon_0 m_s} \cdot \frac{1}{\omega_{0,s}^2 - \omega^2 + \mathrm{i}\omega\Gamma_s} \tag{1.8}$$

with

n_s	in m^{-3}	: number of electrons per volume
$\omega_{0,s}$	in s^{-1}	: resonant frequency
e	in C	: charge of the electron
m_s	in kg	: effective mass
ω	in s^{-1}	: operating angular frequency of the measurement
Γ_s	in s^{-1}	: damping factor

For the low frequency limit the contributions of all faster processes can be assumed to be constants and are combined into ε_∞ in the following. This reduces equation (1.8) to

$$\underline{\varepsilon} = \frac{ne^2}{\varepsilon_0 m} \cdot \frac{1}{\omega_0^2 - \omega^2 + \mathrm{i}\omega\Gamma} + \varepsilon_\infty \tag{1.9}$$

leaving only the polarization mechanism in the measured frequency range. Dividing this equation into its real and imaginary part leads to equations (1.10a) and (1.10b) using the definition of $\underline{\varepsilon} = \varepsilon' - \mathrm{i}\varepsilon''$.

$$\varepsilon' = \frac{ne^2}{\varepsilon_0 m} \cdot \frac{\omega_0^2 - \omega^2}{(\omega_0^2 - \omega^2)^2 + \omega^2\Gamma^2} + \varepsilon_\infty \tag{1.10a}$$

$$\varepsilon'' = \frac{ne^2}{\varepsilon_0 m} \cdot \frac{\omega\Gamma}{(\omega_0^2 - \omega^2)^2 + \omega^2\Gamma^2} \tag{1.10b}$$

The quotient of real and imaginary part, called the loss angle $\tan(\delta)$, is also useful to see a change in damping or resonance frequency:

$$\tan(\delta) = \frac{\varepsilon''}{\varepsilon' - \varepsilon_\infty} = \frac{\Gamma\omega}{\omega_0^2 - \omega^2}. \tag{1.11}$$

[3] The model is named after Hendrik Antoon Lorentz, * 18.07.1853, † 04.02.1928, who received the Nobel Prize in Physics in 1902 together with Pieter Zeeman for their discovery and explanation of the Zeeman effect.

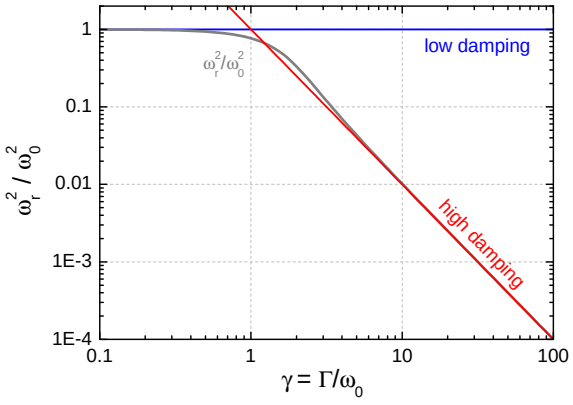

Figure 1.3:
Resonance frequency of a damped Lorentz oscillator.
The dependence of the resonance frequency ω_r^2/ω_0^2 on the damping $\gamma = \Gamma/\omega_0$ as given in equation (1.13). In the case of low damping, $\gamma \ll 1$, the resonance frequency is identical to ω_0. For high damping the γ dependence is found as $\omega_r^2/\omega_0^2 \propto 1/\gamma^2$.

1.3.1 Resonance frequency and relaxation time

With this model the dependence of the resonance frequency ω_r on both the damping Γ and the undamped eigenfrequency ω_0 can be calculated from the zero of the first derivative of the dielectric loss in equation (1.10b):

$$\frac{d\varepsilon''}{d\omega} = \Gamma \frac{\omega_0^4 + 2\omega_0^2\omega^2 - 3\omega^4 - \Gamma^2\omega^2}{((\omega_0^2 - \omega^2)^2 + \Gamma^2\omega^2)^2} = 0.$$

Solving this equation for ω_0^2 leads to two solutions, one of which is always negative and will be ignored as non physical. The remaining solution

$$\omega_0^2 = \sqrt{4\omega_r^4 + \Gamma^2\omega_r^2} - \omega_r^2 \tag{1.12}$$

is always positive and yields the expected result $\omega_0^2 = \omega_r^2$ for the limit of non damping ($\Gamma = 0$).

To study the influence of the damping on the resonance frequency in more detail equation (1.12) is solved for ω_r^2:

$$\omega_r^2 = \frac{-\Gamma^2 + \sqrt{\Gamma^4 - 4\Gamma^2\omega_0^2 + 16\omega_0^4} + 2\omega_0^2}{6}.$$

By introducing a normalized damping factor $\gamma = \Gamma/\omega_0$ the resonance frequency ω_r can be expressed in units of ω_0,

$$\frac{\omega_r^2}{\omega_0^2} = \frac{-\gamma^2 + \sqrt{\gamma^4 - 4\gamma^2 + 16} + 2}{6}. \tag{1.13}$$

This result is plotted in figure 1.3 in combination with plots showing the limits of low and high damping.

For very high damping, $\gamma \gg 1$ ($\Gamma \gg \omega_0$), as expected in all relaxation processes, equation (1.13) yields

$$\frac{\omega_r^2}{\omega_0^2} = \gamma^{-2} = \left(\frac{\Gamma}{\omega_0}\right)^{-2}$$

as can also be seen in figure 1.3. Further simplification yields

$$2\pi\nu_r = \omega_r = \frac{\omega_0^2}{\Gamma} = \frac{1}{\tau} \tag{1.14}$$

with the characteristic relaxation time τ of the system.

1.4 Model functions for dielectric spectra

Assuming a high damping factor, $\Gamma \gg \omega_0$, equation (1.9) can be simplified using (1.14). After bracketing ω_0^2 in the denominator, defining $\Delta\varepsilon = ne^2/(\varepsilon_0 m\omega_0^2)$, and setting $\omega^2/\omega_0^2 \approx 0$ due to the high damping this leads to the most common model function for dielectric spectra, the Debye function

$$\underline{\varepsilon}\,(\omega) = \frac{\Delta\varepsilon}{1 + \mathrm{i}\omega\tau_\mathrm{D}} + \varepsilon_\infty \tag{1.15}$$

with

$$\begin{aligned} \Delta\varepsilon &: \text{dielectric relaxation strength} \\ \tau_\mathrm{D} &: \text{Debye relaxation time} \end{aligned}$$

where τ_D can be calculated from the peak position ν_P in the dielectric loss by $2\pi\nu_\mathrm{P} = 1/\tau_\mathrm{D}$.

If a distribution of several contiguous relaxation times is observed they can either be described by a sum of Debye relaxations or with a single empirical model function. The most general model function is the Havriliak-Negami function [31]:

$$\underline{\varepsilon}_\mathrm{HN}\,(\omega) = \frac{\Delta\varepsilon}{\left(1 + (\mathrm{i}\omega\tau_\mathrm{HN})^\beta\right)^\gamma} + \varepsilon_\infty \tag{1.16}$$

$$\begin{aligned} \beta &: \text{symmetric peak broadening, } 0 < \beta \leq 1 \\ \gamma &: \text{asymmetric peak broadening, } 0 < \beta\gamma \leq 1 \end{aligned}$$

the exponents β and γ lead to a broadening of the peak in the dielectric loss, the influence of the exponents on the form of the curves can be seen in figure 1.4.

Opposed to τ_D the relaxation time τ_HN is not directly related to the peak position in the dielectric loss but depends on the parameters γ and β [47]:

$$2\pi\nu_\mathrm{P} = \frac{1}{\tau_\mathrm{HN}} \left[\sin\frac{\beta\pi}{2+2\gamma}\right]^{1/\gamma} \left[\sin\frac{\beta\gamma\pi}{2+2\gamma}\right]^{-1/\beta}. \tag{1.17}$$

Other model functions can be deduced from the Havriliak-Negami function by setting one of the exponents γ or β to one. With $\gamma = 1$ equation (1.16) is changed into the Cole/Cole function. $\beta = 1$ reduces the Havriliak-Negami function to the Cole/Davidson function. If both exponents are one the Havriliak-Negami function and the Debye function are identical.

1.5 Temperature dependence of dielectric spectra

Not only the frequency dependence of the dielectric function is of interest but also its temperature dependence. For further analysis an assumption has to be made where to enter the temperature dependence into the Debye function, equation (1.15). Here we assume $\tau(T)$ to be depending on the temperature T via a typical temperature activated process,

$$\tau = \tau_0 \mathrm{e}^{\frac{U_\mathrm{b}}{k_\mathrm{B}T}}, \tag{1.18}$$

with τ_0 and the potential barrier U_b as previously mentioned in section 1.1.2. Using this approach the Debye function now has the more complicated form

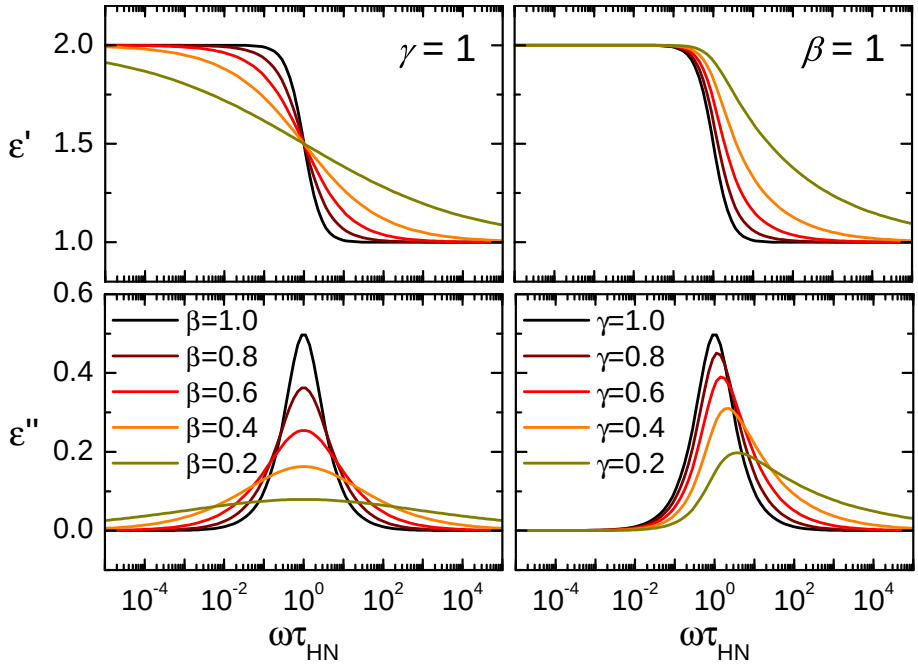

Figure 1.4: Influence of β and γ on the Havriliak-Negami function.
Plot of the Havriliak-Negami function with $\gamma = 1$ (Cole/Cole function) on the left and $\beta = 1$ (Cole/Davidson function) on the right. The black line (━) in all plots ($\gamma = \beta = 1$) represents the Debye function.

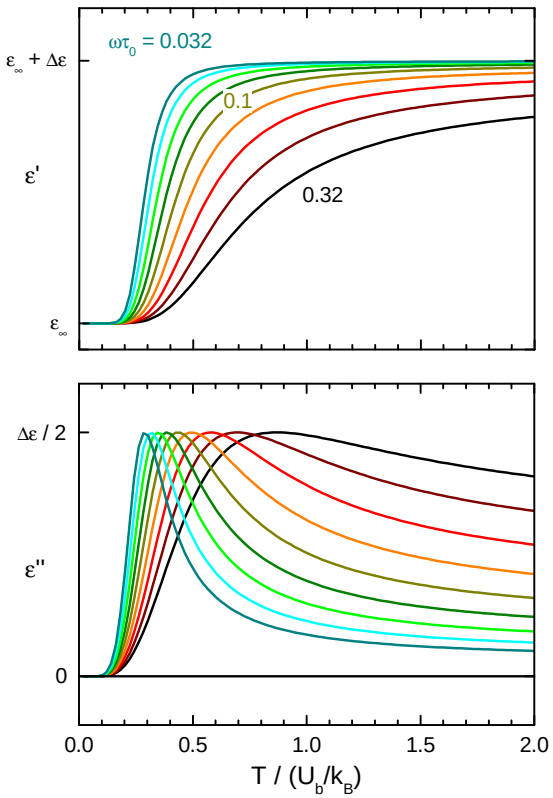

Figure 1.5: Temperature-dependent Debye relaxation. Both real (upper panel) and imaginary part (lower panel) of the complex dielectric function $\underline{\varepsilon}(\omega, T)$ given in equation (1.19) for different normalized frequencies $\tau_0\omega$ as function of normalized temperature T in units of $U_\mathrm{b}/k_\mathrm{B}$. The real part shows a step with a corresponding peak in the imaginary part. For higher frequencies both step and peak are shifted to higher temperatures and less well-defined.

$$\underline{\varepsilon}(\omega, T) = \frac{\Delta\varepsilon}{1 + \mathrm{i}\omega\tau_0 \mathrm{e}^{\frac{U_\mathrm{b}}{k_\mathrm{B}T}}} + \varepsilon_\infty. \tag{1.19}$$

For further analysis this complex function is separated into its real and imaginary part

$$\varepsilon'(\omega, T) = \frac{\Delta\varepsilon}{1 + \omega^2\tau_0^2 \mathrm{e}^{\frac{2U_\mathrm{b}}{k_\mathrm{B}T}}} + \varepsilon_\infty, \qquad \varepsilon''(\omega, T) = -\frac{\Delta\varepsilon\omega\tau_0 \mathrm{e}^{\frac{U_\mathrm{b}}{k_\mathrm{B}T}}}{1 + \omega^2\tau_0^2 \mathrm{e}^{\frac{2U_\mathrm{b}}{k_\mathrm{B}T}}}$$

where the latter is expected to have a maximum. To find the position of this maximum the zero of the first derivative of the imaginary part with respect to T can be calculated as

$$T_\mathrm{max} = -\frac{U_\mathrm{b}}{k_\mathrm{B}} \cdot \frac{1}{\log(\tau_0\omega)}. \tag{1.20}$$

More details on this can be found in appendix A.2 on page 114.

Figure 1.5 shows a plot of both real and imaginary part of equation (1.19) for different normalized frequencies $\tau_0\omega$ as a function of the temperature in units of the activation energy $U_\mathrm{b}/k_\mathrm{B}$. The logarithmic spacing in the normalized frequencies was chosen to show as broad a range of different curves as possible and was inspired by equation (1.20) that predicts a logarithmic spacing of the maxima with respect to $\tau_0\omega$. In real systems not only the relaxation time but also the $\Delta\varepsilon$ may vary with T and its temperature dependence is harder to model.

1.6 Quantum paraelectrics

Quantum paraelectric materials are characterized by a non vanishing dielectric function at $T \to 0\,\mathrm{K}$ that is caused by quantum fluctuations. The name quantum paraelectic has been introduced by Müller and Burkhard [58] who researched the dielectric function of $SrTiO_3$ at temperatures down to and below 4 K. They found that the quantum fluctuations causing the high value of ε' are ferroelectric fluctuations. As the transition temperature in to the ferroelectric phase is expected for $T < 0\,\mathrm{K}$ quantum paraelectic materials are also called incipient ferroelectrics.

1.6.1 Barrett formula

In 1952 Barret [3] proposed a formula to describe the temperature dependence of quantum fluctuations that was derived for χ' in [34]:

$$\chi' = \frac{n k_\mathrm{B} \mu^2}{\left(\frac{\Omega}{2k_\mathrm{B}}\right) \coth\left(\frac{\Omega}{2k_\mathrm{B}} \cdot \frac{1}{T}\right) - \frac{J_0}{4k_\mathrm{B}}} \tag{1.21}$$

with

Ω/k_B : integral of the tunneling probability
n : dipole density
μ : dipole strength
J_0/k_B : $J_0 = \sum_j J_{ij}$ effective coupling constant

In the limit of $\Omega \to 0$ all quantum fluctuations vanish and the equation is reduced to

$$\lim_{\Omega \to 0} \chi' = \frac{n k_\mathrm{B}^2 \mu^2}{k_\mathrm{B} T - J_0/4}, \tag{1.22}$$

because $\lim\limits_{x \to 0} x \cdot \coth(x/a) = a$.

Identifying T_0 with $J_0/4k_\mathrm{B}$ this equation matches the Curie-Weiss law:

$$\lim_{\Omega \to 0} \chi' = \frac{n k_\mathrm{B} \mu^2}{T - T_0} = \frac{C}{T - T_0}. \tag{1.23}$$

1.6.2 Nearly constant loss

A second property discussed in connection with quantum paraelectic materials is the so-called nearly constant loss behavior, meaning that the dielectric loss is observed to have a nearly constant value grater zero over a wide frequency range. In the following section this assumption will be examined theoretically after introducing the Kramers-Kronig relations that are a necessary tool for this considerations.

Kramers-Kronig relations

A function $\underline{f}(\underline{z})$ is complex analytic on an open set D in the complex plane if for any $\underline{z}_0$ in D one can write

$$\underline{f}(\underline{z}) = \sum_{n=0}^{\infty} \underline{a}_n (\underline{z} - \underline{z}_0)^n$$

in which the coefficients $\underline{a}_n$ are complex numbers and the series is convergent to $\underline{f}(\underline{z})$ for $\underline{z}$ in a neighborhood of $\underline{z}_0$ [73]. For every function that is complex analytic in the upper half-plane the Kramers-Kronig relations describe the correlation between real and imaginary part of said function. Due to the implication of analyticity by causality the Kramers-Kronig relations are valid for all response functions of physical systems [89].

The most common notation of the Kramers-Kronig relations, found *e.g.* in [47], is

$$\varepsilon'(\omega) - \varepsilon_\infty = \frac{2}{\pi} PV \int_0^{\omega_0} \frac{u\varepsilon''(u)}{u^2 - \omega^2} \cdot \mathrm{d}u \tag{1.24}$$

where the Cauchy principal value (PV) of the integral has to be used to integrate over the divergence at $\omega = u$.

A more convenient representation of the Krames-Kronig relations for $\underline{\varepsilon}$ that does not rely on the Cauchy principal value is given in equations (1.25), that were derived for the complex Impedance $\underline{Z}$ in [6].

$$\varepsilon'(\omega) - \varepsilon_\infty = \frac{2}{\pi} \int_0^{\omega_0} \frac{u\varepsilon''(u) - \omega\varepsilon''(\omega)}{u^2 - \omega^2} \cdot \mathrm{d}u \tag{1.25a}$$

$$\Delta\varepsilon = \frac{2}{\pi} \int_0^{\omega_0} \frac{\varepsilon''(u)}{u} \cdot \mathrm{d}u \tag{1.25b}$$

$$\varepsilon''(\omega) = -\frac{2\omega}{\pi} \int_0^{\omega_0} \frac{\varepsilon'(u) - \varepsilon'(\omega)}{u^2 - \omega^2} \cdot \mathrm{d}u \tag{1.25c}$$

$$\delta(\omega) = \frac{2\omega}{\pi} \int_0^{\omega_0} \frac{\log|\underline{\varepsilon}(\omega)|}{u^2 - \omega^2} \cdot \mathrm{d}u \tag{1.25d}$$

Many spectroscopic measurement methods rely on the Kramers-Kronig relations to get information on the complex response function while measuring *e.g.* only absolute values without phase information. While this is not the case for the measurements presented in this work it can be quite instructional to use the Kramers-Kronig relations to examine the influence of simple assumptions for the dielectric loss ε'' on ε' as shown in the following section.

Kramers-Kronig and constant loss

If the dielectric loss $\varepsilon'' = a \cdot \omega + b$ is assumed to be a linear function for frequencies below ω_L and still satisfies the analyticity condition for all frequencies up to ω_0 equation (1.25a) becomes

$$\begin{aligned}\varepsilon'(\omega) - \varepsilon_\infty =& \frac{2}{\pi} \int_0^{\omega_\mathrm{L}} \frac{u(a \cdot u + b) - \omega(a \cdot \omega + b)}{u^2 - \omega^2} \cdot \mathrm{d}u \\ &+ \frac{2}{\pi} \int_{\omega_\mathrm{L}}^{\omega_0} \frac{u\varepsilon''(u) - \omega\varepsilon''(\omega)}{u^2 - \omega^2} \cdot \mathrm{d}u\end{aligned} \tag{1.26}$$

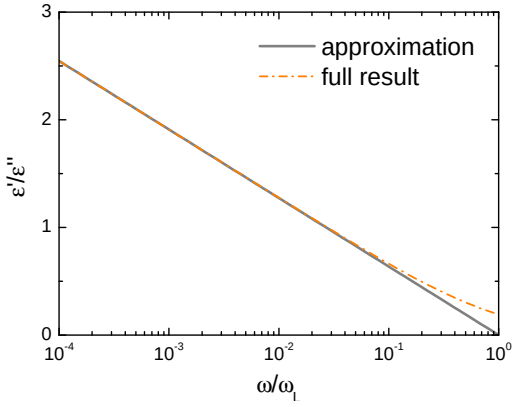

Figure 1.6: Permittivity for a constant loss material. Plot of the Kramers-Kronig equation (1.29) for a constant loss scenario with the slope a and all constant terms set to zero. The constant loss leads to a change of $\varepsilon'(\omega)$ that is proportional to $-\log(\omega)$ if $\omega \ll \omega_\mathrm{L}$.

The second integral yields a finite value that will be called $c(\omega)$ in the following while the first integral can be solved:

$$\begin{aligned}
\varepsilon'(\omega) - \varepsilon_\infty &= \frac{2}{\pi} \int_0^{\omega_\mathrm{L}} \frac{u^2 a + ub - \omega^2 a - \omega b}{u^2 - \omega^2} \cdot \mathrm{d}u + c(\omega) \\
&= \frac{2}{\pi} \Big[a(u+\omega) + b \log(u+\omega) \Big]_{u=0}^{\omega_\mathrm{L}} + c(\omega) \\
&= \frac{2}{\pi} \left[a(\omega_\mathrm{L}+\omega) + b \log\left(\frac{\omega_\mathrm{L}+\omega}{\omega} \right) \right] + c(\omega) \\
&= -\frac{2b}{\pi} \log\left(\frac{\omega}{\omega_\mathrm{L}+\omega} \right) + \frac{2a(\omega_\mathrm{L}+\omega)}{\pi} + c(\omega)
\end{aligned} \tag{1.27}$$

If $\omega \ll \omega_\mathrm{L}$ than equation (1.27) can be reduced to

$$\varepsilon'(\omega) = -\frac{2b}{\pi} \log(\omega) + \frac{2}{\pi} \Big[b \log(\omega_\mathrm{L}) + a(\omega_\mathrm{L}+\omega) \Big] + c(\omega) + \varepsilon_\infty \tag{1.28}$$

where the slope a in ε'' adds both a constant offset and a linear term in ω to ε' . $c(\omega) = c$ can be assumed to be independent of ω as long as the latter is much smaller than ω_L. In the case of a constant loss with $a = 0$ and, therefore, $b = \varepsilon''(\omega) = \varepsilon_\mathrm{c.l.}$ this equations can be further simplified to

$$\varepsilon'(\omega) = -\frac{2\varepsilon_\mathrm{c.l.}}{\pi} \log(\omega) + \text{const.} \tag{1.29}$$

The resulting function $\varepsilon'(\omega)$ is shown in figure 1.6 in comparison to the more extensive equation (1.27) (orange). Here the quality of the approximation can be assessed and only small deviations are visible as long as $\omega \lesssim 0.1\omega_\mathrm{L}$.

1.7 Multiferroics and magnetoelectric materials

1.7.1 Dzyaloshinskii-Moriya interaction

The Dzyaloshinskii-Moriya interaction, sometimes also called anisotropic superexchange interaction, was first postulated by Igor Dzyaloshinskii in 1958 [20].

From symmetry considerations based on the Landau theory he postulated the existence of a contribution to the total magnetic exchange interaction that can be written as $\mathcal{H} = \mathbf{D}_{i,i+1} \cdot (\mathbf{S}_i \times \mathbf{S}_{i+1})$. Two years later Tôru Moriya [55] explained the origin of the anisotropic superexchange interaction with the spin-orbit coupling, giving the phenomenological model from Dzyaloshinskii a firm theoretical basis.

The effects of the Dzyaloshinskii-Moriya interaction are sketched in figure 1.7. The Dzyaloshinskii vector $\mathbf{D}_{i,i+1}$ is proportional to the spin-orbit coupling constant and the position $\mathbf{x}$ of the superexchange ion, typically O^{2-}, the open circle in the sketch. Therefore, the anisotropic superexchange can shift the position $\mathbf{x}$ of the superexchange ion and slightly deform the crystal structure and in some cases breaking the inversion symmetry and creating an electric dipole moment. The latter only happens in spiral spin states where the induced dipole moment $\mathbf{P}$ can be expressed as

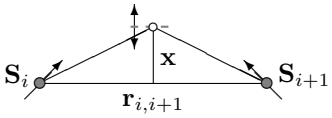

Figure 1.7: Effects of the Dzyaloshinskii-Moriya interaction.

$$\mathbf{P} \propto \mathbf{r}_{i,i+1} \times (\mathbf{S}_i \times \mathbf{S}_{i+1}).$$

In non-spiral spin configurations the spin current $\mathbf{j}_{i,i+1} = \mathbf{S}_i \times \mathbf{S}_{i+1}$ does not have the same sign for all i thus the sum of all $\mathbf{j}_{i,i+1}$ vanishes.

More comprehensive information on the Dzyaloshinskii-Moriya interaction can be found *e.g.* in [13].

1.7.2 Multiferroics

In general multiferroics are materials that combine any two or more ferroic properties, *i.e.* ferroelectric, ferromagnetic, ferrotoroidicity, or ferroelasticity. Though typically only the coexistence of ferromagnetic and ferroelectric ordering is thought of when calling a material multiferroic.

In this case not only a coupling, *e.g.* $P \propto H$, exists but both P and M are switchable equally by H or E.

Type I

Type I multiferroics are materials where the ferromagnetic and ferroelectric are caused by separate effects and in general also exhibit different transition temperatures. For this materials the coupling between ferromagnetic and ferroelectric is very weak.

Type II

For the type II multiferroics this is not true. Here the magnetic order causes the ferroelectric behavior and a strong coupling exists between the magnetic and electric properties. The downside of type II multiferroics is their weak polarization, that is smaller compared to canonical ferroelectric materials by four orders of magnitude.

For more information on multiferroic materials see *e.g.* [13, 38]

1.8 Magnetic monopoles

The search for magnetic monopoles has its origin in the symmetry of the field equations of electrodynamics with respect to electric and magnetic field. However, the symmetry between both fields is disturbed by the absence of experimental prove of a single magnetic charge on a particle.

1.8.1 Dirac monopoles

This problem was studied by Dirac in the 1930s and in the course of 20 years he published several papers [17, 18] on this topic. In [18] he summarizes his ideas that will be roughly explained in the following.

The typical approach to the vector potential in magnetism,

$$\mathbf{F} = \nabla \times \mathbf{A} \tag{1.30}$$

only works if there are no magnetic monopoles. In this case equation (1.30) also means that for any closed surface at any moment the flux through this surface has to vanish.

If there exists a magnetic monopole this cannot be true for any surface of a volume that contains the monopole, *e.g.* a sphere centered on the monopole, as the magnetic flux from the monopole cannot vanish. But it can be assumed that the flux from the monopole only crosses the surface at one point for each closed surface surrounding the monopole. Tracing this point through space as the volume expands leads to the so called Dirac string that connects the monopole either with infinity or with their corresponding anti monopole. The key to Dirac's theory is that the strings are invisible for the magnetic monopoles and their length does not influence the monopoles. For this reason the strings are sometimes also called tensionless.

1.8.2 't Hooft monopoles

A different approach on magnetic monopoles was introduced by 't Hooft in [35] were he showed that the Dirac string is not necessary in gauge theories where the electromagnetic group is a subgroup of a larger group with compact covering group.

While 't Hooft monopoles are closer to the intuitive notion of a monopole than the Dirac monopoles as they can be seen as single entities they are only mentioned here for the sake of completeness. For the experimental work in this thesis only the former type of monopoles is important.

1.9 Piston effect

In the early 1990s the critical properties of liquids close to the critical point of their liquid-gas transition have been studied [7, 66, 94]. The focus of these studies was the thermal equilibration of ^{3}He in zero gravity that were experimental observed [14] to be much faster than expected. This was explained by the adiabatic change of temperature and density in compressible liquids. Close to the critical point this process dominates due to the divergence of c_P and the adiabatic process dominates the distribution of temperature throughout the bulk. The authors conclude that for a fixed volume of the sample cell their numerical calculations reproduce the observed critical speeding up.

2 Experimental minutiae

Following the theoretical topics in the previous chapter here the measurement techniques used will be introduced. Again, an in-depth explanation is left to literature. Instead only a brief summary of the working principles of the instruments used is provided.

Contents

2.1 Sample preparation

For all measurements of the polarization and related quantities such as the complex impedance the sample has to be prepared correctly before measuring. The most important consideration is the sample geometry. Besides the basic need to align the magnetic and electric fields with certain crystallographic axes the geometric capacitance $C_0 = \varepsilon_0 \cdot A/d$ should be optimized. This can be done by either reducing the thickness d of the sample or increasing the area A of the capacitor plates that have to be applied to both sides of the sample. The material of the capacitor plates can be varied to check for effects of contact resistance on the measurements.

For this reason a thin slab is the best option, even though depending on the orientation of the sample with respect to the magnetic field the demagnetization (section 2.6) has to be taken into account when applying a magnetic field.

Finally, the sample has to be glued on the sample holder and both sides are connected to the cables using silver paint. Figure 2.1 shows a sketch of the microstrip sample holder with a sample.

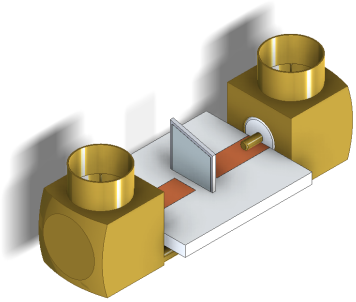

Figure 2.1:
Sketch of the sample holder.
The external magnetic field is oriented in z direction while the electric field for the depicted sample orientation is perpendicular to H along the copper stripe.

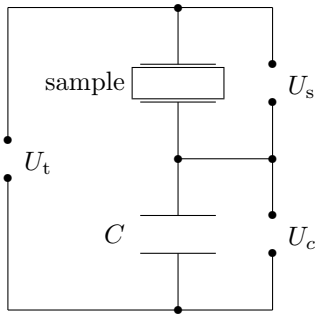

Figure 2.2:
Sawyer-Tower circuit.
Simplified diagram of the Sawyer-Tower circuit. The dielectric constant of the sample can be calculated from the ratio of U_S and U_C if the value of C is known.

2.2 Sawyer-Tower circuit

For measurements of the polarization of ferroelectric materials Sawyer and Tower [77] introduced an electric circuit that is sketched in figure 2.2.

The sample is mounted as dielectric in a plate capacitor with a reference capacitor C of known capacity in series. Applying a voltage U_t leads to a shift of charges $Q = C \cdot U_c$ at the reference capacitor. Due to the serial setup the same amount of charge is moved at the sample. From the evaluation of the two partial voltages U_s and U_c both the polarization P and the applied electric field can be calculated from the electric displacement field $D = Q/A$ and the electric field $E = U_s/d$ of a plate capacitor:

$$\begin{aligned} E &= \frac{1}{d} U_s \\ P = D - \varepsilon_0 E = \frac{Q}{A} - \frac{\varepsilon_0 U_s}{d} &= \frac{\varepsilon_0}{d}\left(\frac{C}{C_0} U_c - U_s\right) \end{aligned} \tag{2.1}$$

From the combination of equations (2.1) and $P = \chi \varepsilon_0 E + P_s$ the sample specific quantities can be found.

Using a reference capacitor with a much higher capacity than the sample, $C \gg C_s$, and measuring both the total voltage $U_t = U_s + U_c$ and the voltage U_c at the reference capacity reduces the complexity of the analysis and also has additional advantages, see [32]. In this case the voltage at the sample can be approximated with the total voltage $U_s \approx U_t$.

In the original presentation of the circuit an oscilloscope was used to monitor the results. All measurements shown in this work were obtained using a *Keithly*

6517B Electrometer to measure either the charge Q for hysteresis loops or the current I for Pyro-Current measurements.

More information on the experimental details of the Sawyer-Tower circuit used can be found in [32].

2.2.1 Hysteresis loops

From the measurement of the applied voltage U_t and the charge Q the $P(E)$ hysteresis loop can be calculated from measurements with different voltages if the geometry of the sample is known.

If $C \gg C_\mathrm{s}$ is satisfied the electric field applied to the sample can be approximated to $E \approx U_\mathrm{t}/d$. Due to the serial setup of both capacitors the amount of charges moved through the circuit also has to reside on the sample and thus $P = Q/A$.

2.2.2 Pyro-Current

Typical pyro-current measurements are done by cooling the sample with an applied electric field from the paralectric to the ferroelectric phase. This causes all ferroelectric domains in the sample to fully nucleate in an advantageous orientation with respect to the electric field and thereby maximizes the electric polarization. Once the cooling of the sample is complete the electric field is disabled, $U_\mathrm{t} = 0$.

The actual measurement of the Pyro-Current is performed during the reheating of the sample with a constant temperature drift without electric field. Both the discharge current of the fully polarized sample and the temperature are recorded as a function of time. Due to the large amounts of charge that are shifted at the ferroelectric phase transition and the technical limitations of the instrument it is more convenient to measure charge indirectly via the displacement current $I = \mathrm{d}Q/\mathrm{d}t$.

Integrating the current I over the time t leads to the charge Q and thus also to the polarization $P = Q/A$.

2.3 Measuring the complex dielectric function

To achieve as broad a frequency range as possible different measurement techniques have to be used. In the following sections the spectroscopy techniques used in this work and the methods to calculate $\underline{\varepsilon}(\nu)$ from the measured quantities are briefly introduced.

2.3.1 Impedance spectroscopy

For frequencies up to roughly 10 MHz impedance spectroscopy can be used to measure the complex impedance $\underline{Z}$ of the sample. In this thesis a *Novocontrol Alpha-A Analyzer* was used that covers a broad frequency range from 1 mHz to 10 MHz. For the measurement of the complex impedance it uses the gain-phase method that measures current $\underline{I}$, voltage $\underline{U}$, and phase angle ϕ to calculate $\underline{Z}$ using

$$\underline{Z} = \frac{\underline{U}}{\underline{I}}$$

In earlier measurements using the Novocontrol Alpha-A Analyzer the results were saved in an alternative form from $\underline{Z}$, R_p and C_p. Using the equivalent circuit

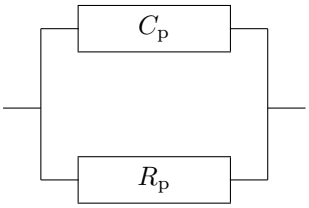

Figure 2.3: Equivalent circuit diagram: R_p and C_p.
For the calculation of $\underline{Z}$ from R_p and C_p an ideal resistor is assumed to be connected in parallel with an ideal capacitor.

diagram in figure 2.3 $\underline{Z}$ can be calculated by $1/\underline{Z} = 1/R_\mathrm{p} + \mathrm{i}2\pi\nu C_\mathrm{p}$. Solving this equation for Z' and Z'' leads to

$$Z' = \frac{\dfrac{1}{R_\mathrm{p}}}{\left(\dfrac{1}{R_\mathrm{p}}\right)^2 + (2\pi\nu C_\mathrm{p})^2}, \qquad Z'' = \frac{-2\pi\nu C_\mathrm{p}}{\left(\dfrac{1}{R_\mathrm{p}}\right)^2 + (2\pi\nu C_\mathrm{p})^2}. \tag{2.2}$$

2.3.2 Vector network analysis

When increasing the frequency ν at some point the corresponding wavelength λ will be equal or shorter than the length of the cables in the setup[1]. In this case the simple method described earlier will no longer yield accurate information on the phase ϕ and a different approach has to be used. This is done by using a complex network analyzer that measures the scattering parameters, which are the ratios between the amplitudes of the outgoing and incoming signal. The convention for the notation of the four scattering parameters is $\underline{S}_\mathrm{sr}$ where the electromagnetic wave is applied at the source port s and the measurement of the reflected (r = s) or transmitted (r ≠ s) wave is done at the receiver on port r. In figure 2.4 the scattering parameters are shown in a sketch. For the measurements in the higher frequency range two diveces were used. The *Rhode & Schwartz ZVB4* for frequencies from 100 kHz to 4.2 GHz and the *Agilent PNA-X* in the range of 10 MHz to 20 GHz.

Calibration

Opposed to the measurement of the complex impedance for this measurements extensive calibrations have to be done beforehand. For the calibration the four standards open, load, short, and through are used. The first three standards are used to individually calibrate each of the semi rigid coaxial cables of the setup by changing the resistivity between the inner conductor and the outer shield at the sample location from $R_\mathrm{open} \to \infty$ via $R_\mathrm{load} = 50\,\Omega$ to $R_\mathrm{short} = 0\,\Omega$. Finally, the through connects the inner conductors of both cables with $R_\mathrm{through} = 0\,\Omega$ and is used to match both ports. For the best result the calibration standards have been build in sample holders that are as close to the geometry used for the

[1] For the dilution refrigerator the cable length was roughly 6 m ≈ 50 MHz, for the PPMS 2 m ≈ 150 MHz.

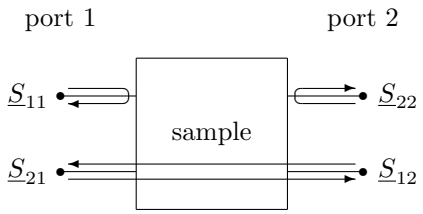

Figure 2.4: Scattering parameters.
The four scattering parameters of a transmission setup originate from the dual purpose of ports 1 and 2 that can act as both source and receiver. For a perfectly symmetrical setup it would be irrelevant which port acts as receiver, meaning that $\underline{S}_{12} = \underline{S}_{21}$ and $\underline{S}_{11} = \underline{S}_{22}$.

measurements as possible. The principle used for the calibration and an in-depth explanation of calibration methods can be found *e.g.* in [11].

Due to the relatively short wavelength in the higher frequency range the position of the sample has to be very well defined by the calibration and changes in the position, *e.g.* due to thermal expansion or different thermal gradients on the coaxial cables, result in an error in the measured phase ϕ that is frequency-dependent. As most of the cables in the dilution refrigerator are subjected to a constant temperature gradient the influence of this errors is smaller in this setup compared to the PPMS. To correct this error different approaches can be used. Either a reference spectrum can be subtracted that should be measured in a region of the (H, T) phase diagram where no peaks are located or the phase shift can be corrected mathematically using an electrical length. The electrical length l_e can be understood as a virtual length of cable that has to be traversed by the electromagnetic wave and induces a frequency-dependent phase shift $\Delta\phi(\nu)$ according to

$$\Delta\phi(\nu) = \frac{2\pi\nu \cdot l_\mathrm{e}}{c} \tag{2.3}$$

with the speed of light c.

Calculating Z from S_{21}

After the calibration the setup can in principal be used for reflection ($\underline{S}_{11}/\underline{S}_{22}$) or transmission ($\underline{S}_{12}/\underline{S}_{21}$) measurements. As can be seen in figure 2.5 the best results for insulating samples are expected for transmission measurements. For this type of measurement the complex impedance can be calculated from the transmission parameter $\underline{S}_{12}$ or $\underline{S}_{21}$ using

$$\underline{Z} = \frac{100\,\Omega}{\underline{S}_{12/21}} - 100\,\Omega. \tag{2.4}$$

For the sake of convenience the notation with separated real and imaginary part is also given:

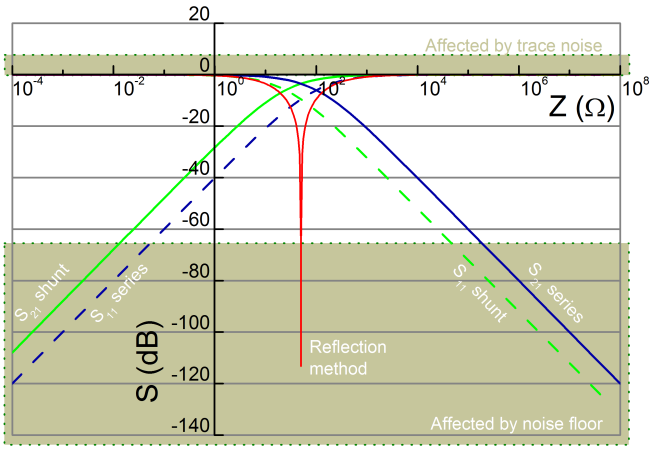

Figure 2.5: Scattering parameters vs. $|Z|$.
The quality of the measured signal depends on the scattering parameter measured and the resistivity of the sample. For the insulating samples that are used in this thesis the transmission parameters $\underline{S}_{12}$ and $\underline{S}_{21}$ are expected to yield the best results.

$$Z' = \frac{100\,\Omega\, S'_{12/21}}{S'^2_{12/21} + S''^2_{12/21}} - 100\,\Omega, \qquad Z'' = -\frac{100\,\Omega\, S''_{12/21}}{S'^2_{12/21} + S''^2_{12/21}}. \tag{2.5}$$

A similar but slightly different equation has to be used when calculating the impedance from the reflection measurements. Here the corresponding equation for the transformation is

$$\underline{Z} = 100\,\Omega \cdot \frac{\underline{S}_{11/22}}{1 - \underline{S}_{11/22}}. \tag{2.6}$$

Combining both equations (2.4) and (2.6) leads to a third equation for the calculation of $\underline{Z}$:

$$\underline{Z} = 100\,\Omega \cdot \frac{\underline{S}_{11/22}}{\underline{S}_{12/21}} \tag{2.7}$$

Using this equation has the advantage to mostly remove the electrical delay caused by the temperature gradient on the coaxial cables as this is picked up by both the transmission and reflection parameters.

Sample induced electrical delays

Note that this assumption ignores an electrical length correction that should take into account the time the electromagnetic wave needs to traverse the sample. In principle this leads to a phase correction of

$$\Delta\phi = \frac{2\pi\nu}{c} d\sqrt{\underline{\varepsilon}} \tag{2.8}$$

that depends on the sample thickness d and the complex refractive index $\sqrt{\underline{\varepsilon}}$. The importance of this correction for measurements at higher frequencies is immediately apparent. To estimate the frequency limit below which this effect can

be ignored a thickness of $d = 1\,\mathrm{mm}$ and a phase resolution of the instrument of $\Delta\phi = 0.01$ is assumed. Accordingly, frequencies below $\nu_\varepsilon \approx 477\,\mathrm{MHz}/\sqrt{\underline{\varepsilon}}$ show no significant phase shift from this contribution.

The actual application of this correction is difficult as the permittivity would have to be solved self-consistently. One method is the Nicolson-Ross-Weir (NRW) algorithm [62, 91] that was first published in 1970 and has been refined multiple times ever since. As most measurements in this work are well below the limiting frequency ν_ε, even when taking into account the high permittivity in quantum paraelectric materials, no detailed description of the NRW algorithm is given. More information on both the original NRW algorithm as well as the enhanced versions can be found *e.g.* in [11].

2.3.3 Calculation of ε from Z

For the calculation of $\underline{\varepsilon}$ from $\underline{Z}$ the simple ansatz of a series circuit with a resistive and a capacitive element is sufficient. Here the impedance of a capacitor with complex dielectric function is assumed to be equal to the measured complex impedance.

$$\frac{1}{\mathrm{i}2\pi\nu C_0\underline{\varepsilon}} = Z' + \mathrm{i}Z''$$

Solving this equation for $\underline{\varepsilon} = \varepsilon' - \mathrm{i}\varepsilon''$ and separating real and imaginary part by multiplication with the complex conjugate leads to

$$\varepsilon' = -\frac{1}{2\pi\nu C_0}\cdot\frac{Z''}{Z'^2 + Z''^2}, \qquad \varepsilon'' = \frac{1}{2\pi\nu C_0}\cdot\frac{Z'}{Z'^2 + Z''^2} \tag{2.9}$$

2.4 Heating effects due to electric ac currents

When measuring the dielectric properties of a sample in general the signal to noise ratio can be improved by using higher voltages. But during measurements at low temperatures an additional unwanted effect has to be taken into account, namely the heating of the sample due to the applied ac voltage. For electric dc circuits the electric power is defined as:

$$P_\mathrm{dc} = U_\mathrm{dc}\cdot I_\mathrm{dc}. \tag{2.10}$$

If only the voltage U_dc is known this equation can be solved with the help of Ohm's law, $R = U_\mathrm{dc}/I_\mathrm{dc}$, and the power can be expressed as $P_\mathrm{dc} = U_\mathrm{dc}^2/R$. Here the sensitivity of the dissipated electrical power to the applied voltage can be seen in the power of two observed for U_dc.

For electric ac circuits the notation on voltages and currents is more complicated and figure 2.6 explains the different relevant designations. Using this notation the active power (sometimes also called real power) can be defined as

$$P_\mathrm{ac} = U_\mathrm{rms}\cdot I_\mathrm{rms}\cos(\phi) \tag{2.11}$$

with the effective voltage U_rms, effective current I_rms, and the phase change ϕ. Using again Ohm's law, now with a complex impedance $\underline{Z} = Z' + \mathrm{i}Z''$, the current can be replaced by $U_\mathrm{rms}/|\underline{Z}^2|$. Similarly the phase shift can be given as $\cos(\phi) = Z'/|\underline{Z}|$ leading to

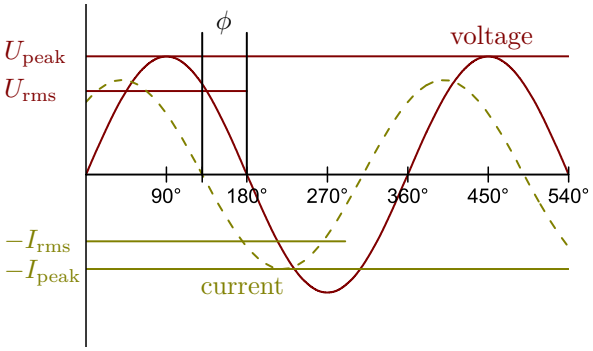

Figure 2.6:
ac voltage and current.
Simple picture of the ac voltage (red) and current (yellow) to explain the notation used. The peak voltage U_{peak} is related to the root mean square value U_{rms} as $U_{\mathrm{peak}} = \sqrt{2}\,U_{\mathrm{rms}}$ with the crest factor $\sqrt{2}$. ϕ describes the phase shift between current and voltage.

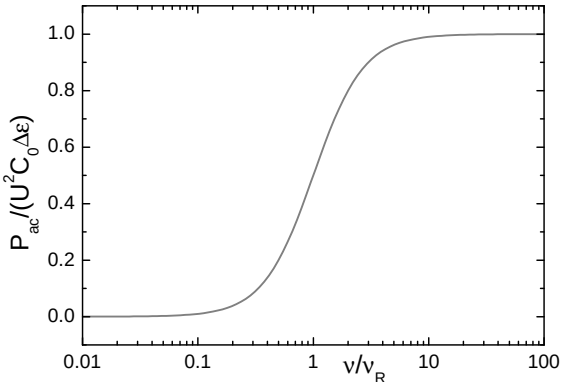

Figure 2.7:
Heating power for a Debye relaxation.
Normalized heating power for a Debye relaxation as a function of normalized frequency. Close to the resonance frequency ν_{R} the heating power strongly increases until it saturates at $\nu \gg 10\,\nu_{\mathrm{R}}$. Thus the frequency dependence of ε'' offsets the increase in heating power with frequency. Still the intuitive expectation that higher frequencies lead to stronger heating is confirmed with this example.

$$P_{\mathrm{ac}} = U_{\mathrm{rms}} \cdot \frac{U_{\mathrm{rms}}}{|\underline{Z}|} \cdot \frac{Z'}{|\underline{Z}|} = U_{\mathrm{rms}}^2 \cdot \frac{Z'}{|\underline{Z}|^2} \tag{2.12}$$

Combining this result with the second part of equation (2.9) leads to

$$P_{\mathrm{ac}} = U_{\mathrm{rms}}^2 \cdot 2\pi\,\nu\,\varepsilon''(\nu)\;C_0. \tag{2.13}$$

While in an electric ac circuit the applied voltage still enters the dissipated electric power with a power of two the result is also directly proportional to the frequency ν and the dielectric loss $\varepsilon''(\nu)$. This leads to a convoluted frequency-dependent heating power, as shown in figure 2.7 for a Debye relaxation. In this example the heating power does not diverge. Instead it saturates at a finite value due to the frequency dependence of the dielectric loss present in a perfect Debye relaxation. Nevertheless, as expected from equation (2.13), higher frequencies lead to stronger heating even when considering a realistic model for ε'' .

Therefore, the intrinsic sample properties have to be taken into account when selecting the appropriate ac voltage and for every sample the measured sample

temperature should be observed closely during the ac measurements to exclude unintended changes of the sample temperature.

2.5 Open-Short-Load calibration for the Novocontrol Alpha-A Analyzer

Capacitive and inductive effects of the coaxial cables and the sample holder used for 2-wire measurements cause additional contributions to the measured impedance of the sample.

One method to compensate this error is the Open-Short-Load calibration, that requires frequency-dependent measurements of the three standards Open, Load, and Short. For the calibration of our probe we use an empty sample holder as Open, a mostly frequency-independent capacitor as Load, and a shorted sample holder as Short.

Using this measurements equation (2.14) can be used to correct the results for a fixed frequency ν:

$$\underline{Z}(\nu) = \frac{\underline{Z}_\mathrm{S}(\nu) - \underline{Z}_\mathrm{M}(\nu)}{\underline{Z}_\mathrm{M}(\nu) - \underline{Z}_\mathrm{O}(\nu)} \cdot \frac{\underline{Z}_\mathrm{L}(\nu) - \underline{Z}_\mathrm{O}(\nu)}{\underline{Z}_\mathrm{S}(\nu) - \underline{Z}_\mathrm{L}(\nu)} \cdot \underline{Z}_\mathrm{DCL}. \tag{2.14}$$

$\underline{Z}$	: true impedance of the sample
$\underline{Z}_\mathrm{M}$	: uncorrected measurement of the sample
$\underline{Z}_\mathrm{O}$	: measured value for the Open
$\underline{Z}_\mathrm{S}$	: measured value for the Short
$\underline{Z}_\mathrm{L}$	: measured value for the Load
$\underline{Z}_\mathrm{DCL}$	: DC resistivity of the Load

A derivation of this formula is given in appendix B.1 from page 115 onward. When taking into account that the calibration standards might not be perfect a similar but more complicated equation can be calculated from the same approach used. The generalized equation can also be found in the appendix.

For better comparability with the experiment the Load was implemented using a 5.1 pF capacitor. The value of $\underline{Z}_\mathrm{DCL}$ in equation (2.14) for this Load is now frequency-dependent and its complex value has to be calculated with equation (2.2).

2.6 Demagnetization

If a ferromagnetic sample is located in a homogeneous external magnetic field strength H the internal magnetic field strength H_i will be reduced by the (anisotropic) demagnetization factor D times the magnetization M. D is strongly dependent on the geometry of the sample and theoretical descriptions of the demagnetization factors have been published for three different sample shapes: ellipsoids [67], cylinders [46] and prisms [1].

While the ellipsoids are found to have an uniform demagnetization factor of ⅓ in an external field the other two sample shapes considered are much more complicated and depend on the direction of H with respect to the sample.

The for this work most important—and at the same time most complicated in terms of demagnetization—geometry is the prism as this is the typical geometry of single crystalline samples prepared for measurements. High resolution dielectric

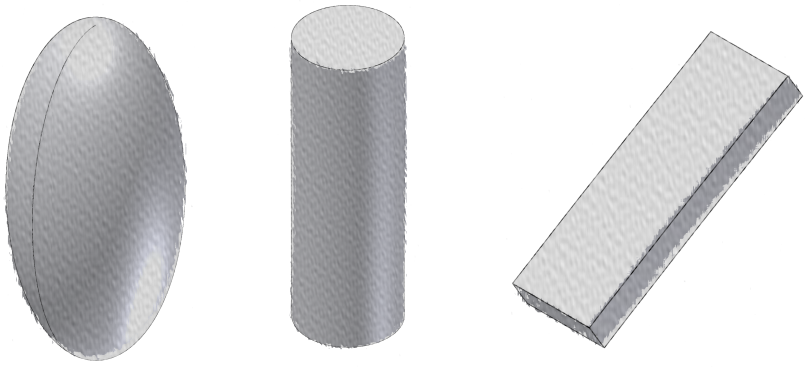

(a) Ellipsoid **(b)** Cylinder **(c)** Prism

Figure 2.8: Prominent sample shapes for demagnetization considerations. Three sample shapes considered for the theoretical description of the demagnetization.

measurements also have requirements on the sample shape that have to be met. For a high signal the sample thickness d should be small while the area A used for the conductor plates should be as big as possible. An extreme example for the optimal geometry would be an infinite plane of vanishing thickness. In this case the demagnetization factor perpendicular to the plane is unity while the demagnetization parallel to the plane vanishes. Real samples deviate from this approximation; here $D_\perp$ is slightly smaller than 1 and $D_\parallel$ not exactly zero. The correct values for the demagnetization factors depend on the length of the edges a, b, and c as well as the angles between them and can be either calculated with the formula given in [1] or by means of numerical simulations. In the course of this work the latter approach was used to calculate H_i from magnetization data and sample geometry using a finite elements approach by means of the radia software package, see appendix B.3.

2.6.1 Notation of magnetic fields

The demagnetization discussed previously also gives rise to the need to carefully define which magnetic field related quantity is used for the deliberations made in the following chapters. Also, the practice of using the same unit, namely Tesla, for both the magnetic flux density B and the magnetic field strength H complicates the distinction even further. The latter is then multiplied with $\mu_0 = 4\pi \times 10^{-7}\,\mathrm{V\,s\,A^{-1}\,m^{-1}}$ in order to convert its unit from $\mathrm{A\,m^{-1}}$ to T. Therefore, the rest of this work will follow a strict notation that is explained in the following.

The external applied magnetic field strength H_external, short H, will denote the homogeneous magnetic field produced by the superconducting magnets in the different cryostats and is the quantity that can be controlled in the experiments. Keeping in mind the deliberations on demagnetization the internal magnetic field strength $H_\mathrm{internal} = H_\mathrm{i} = H_\mathrm{external} - DM$ can be calculated from the magnetization M and the shape of the sample that results in the unit less demagnetization factor $0 \leq D \leq 1$ in the direction of the applied external magnetic field strength H. Finally, the magnetic flux density of the sample $B_\mathrm{internal} = B_\mathrm{i} = \mu_0(H_\mathrm{i} + M) =$

$\mu_0(H + (1 - D)M)$ denotes the magnetic flux density within the sample.

It is interesting to note that in the case of a infinite plane perpendicular to the external magnetic field strength H the demagnetization factor D becomes unity and the magnetic flux density

$$B_{\mathrm{i,plane}} = \mu_0 H \tag{2.15}$$

is equal to the external magnetic field strength times μ_0 and the magnetization of the sample is irrelevant. This is also a very good approximation for real samples that are smaller but still have a similar sample shape, *i.e.* thin slabs, and has been discussed for the (quantum) hall effect where a similar geometry is required.

2.7 Cooling devices

The measurements presented in this work were done at a broad range of temperatures and magnetic fields to fully access the phase diagram. To achieve the necessary precise control of the temperature the measurements were done in magneto-cryostats whose working principles will be explained in the following sections.

2.7.1 ^{4}He cryostat

In simplest terms a ^{4}He cryostat can be though of as a vacuum insulated barrel where liquid Helium is stored at its boiling temperature of 4.2 K. Within this liquid Helium bath the sample space is realized as a vacuum insulated tube in the center of the cryostat. Here the temperature of the sample is regulated by electric heating with a resistor and cooling by funneling a controlled amount of Helium gas through the sample space. Figure 2.9a shows a sketch of the cryostat used as environment for the dilution refrigerator unit explained in the next section.

For measurements above 1.8 K a *Quantum Design "Physical Properties Measurement System"* (PPMS) was used. Here a specially designed sample platform, figure 2.9b, was created to maximize thermal coupling of the sample to the temperature controlled heat bath of the cryostat. In the PPMS this coupling only occurs through the lower part of the platform. The oddly shaped part in the center in combination with the brace forces the sample holder shown in figure 2.1 to have mechanical contact with the platform. This has the additional advantage that the sample thermometer can be fixed onto the sample platform in the proximity of the sample thus considerably reducing the time required for sample changes and the wear of the thermometer wiring.

2.7.2 ^{3}He/^{4}He dilution refrigerator

When measurements at very low temperatures are required two systems based on the use of the less common isotope ^{3}He are employed. The first system uses the evaporation of pure ^{3}He and reaches a base temperature of 0.25 K, as can be seen in 2.10b. Even lower temperatures can be achieved using not the heat of vaporization but the mixing enthalpy of both He isotopes, ^{3}He and ^{4}He.

This only works due to a peculiarity of Helium, namely the finite solubility of ^{3}He in ^{4}He at absolute zero temperature. Caused by the different quantum mechanical nature of both isotopes, ^{3}He being fermionic as opposed to the bosonic ^{4}He, this gives the potential for cooling at very low temperatures. Figure 2.10b shows that

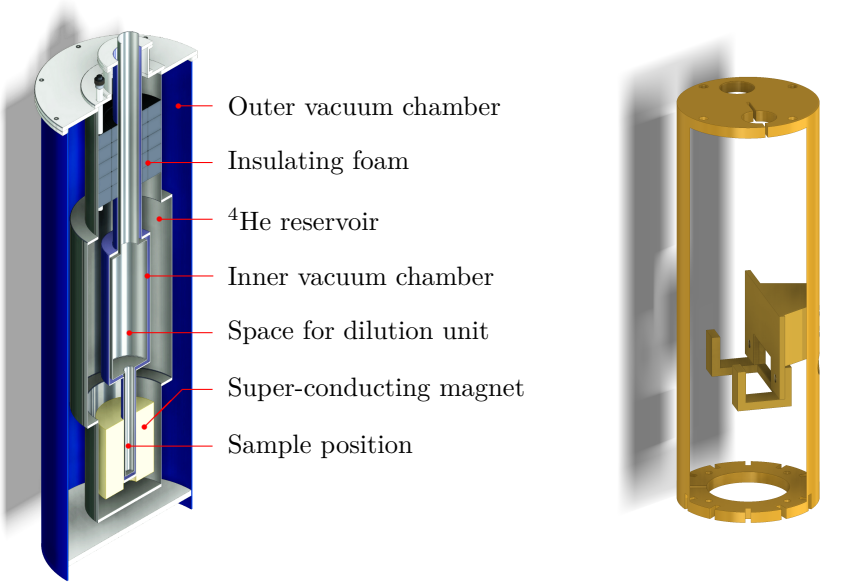

(a) ^{4}He bath cryostat. **(b)** PPMS Sample platform.

Figure 2.9: ^{4}He bath cryostat.
(a) shows a sketch of the basic components of a ^{4}He bath cryostat. The model is based on the specifications of the cryostat of the dilution refrigerator used on this work. In (b) a sketch of the sample platform used in the PPMS is shown.

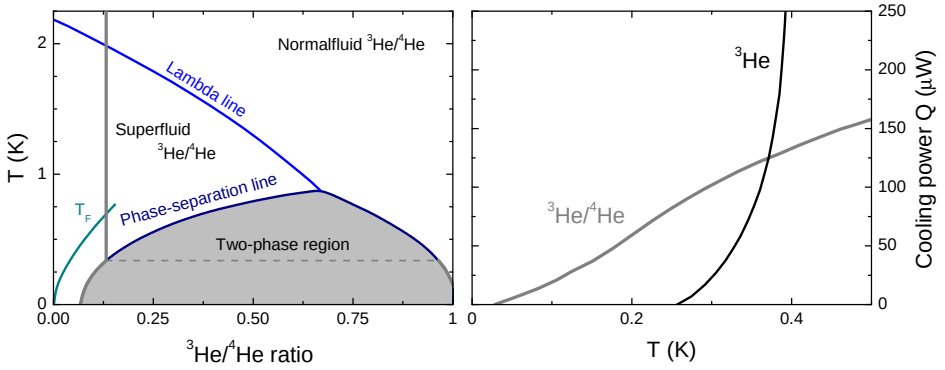

(a) Phase diagram of diluted ^{3}He.

(b) Cooling power of ^{3}He/^{4}He cooling systems.

Figure 2.10: ^{3}He/^{4}He phase diagram and cooling power.
(a) Phase diagram of diluted ^{3}He. The gray lines indicate the ^{3}He/^{4}He ratio of 15% used in the dilution refrigerator. Phase separation for this concentration set in at roughly 0.35 K as indicated by the dashed line. At lower temperatures the ^{3}He concentration of both phases changes independently and the mixed phase still has 6.6% ^{3}He left at absolute zero. (b) compares the cooling power of a pure ^{3}He system to a dilution refrigerator. The latter has less cooling power at temperatures above 0.35 K but reaches much lower base temperatures. Both plots are based on data from [68]

a finite cooling power from a dilution refrigerator can be expected at temperatures much lower than achieved with pure ^{3}He.

The finite solubility can be seen in figure 2.10a where phase separation between the isotopes sets in at above 6.6% ^{3}He. In the cryostat a mixture with 15% ^{3}He is used, marked by the gray (—) line. Below 2 K this mixture enters a superfluid phase and below roughly 0.35 K the phase separation happens. Now within the mixing chamber two phases exist, one of which consists almost purely of ^{3}He. Due to the weight difference in the isotopes the ^{3}He rich phase will arise on top of the ^{4}He rich phase. This stacking of the phases is important for the technical realization of the dilution refrigerator that is shown in figure 2.11a.

During the operation of the dilution refrigerator the phases in the mixing chamber are separated. A capillary is used to connect the diluted phase with the distillation unit, short still, where the ^{3}He is removed from the liquid by heating the still to approximately 0.7 K. This causes a gradient in the ^{3}He concentration and the ensuing osmotic pressure causes more ^{3}He to flow from the mixing chamber to the still. As it is energetically favorable to maintain the saturation ratio between the He isotopes new ^{3}He atoms will crossover from the pure ^{3}He phase, thereby cooling the mixing chamber due to the mixing enthalpy.

The almost pure ^{3}He vapor produced in the still is removed by pumping and the ^{3}He is heated to room temperature. In the next step the ^{3}He gas is fed through a series of heat exchangers where it is cooled down before it is returned into the concentrated phase in the mixing chamber.

This closed cycle approach has the advantage of allowing for continuous operation without the need to periodically re-condense the liquid ^{3}He as is required for pure ^{3}He cooling.

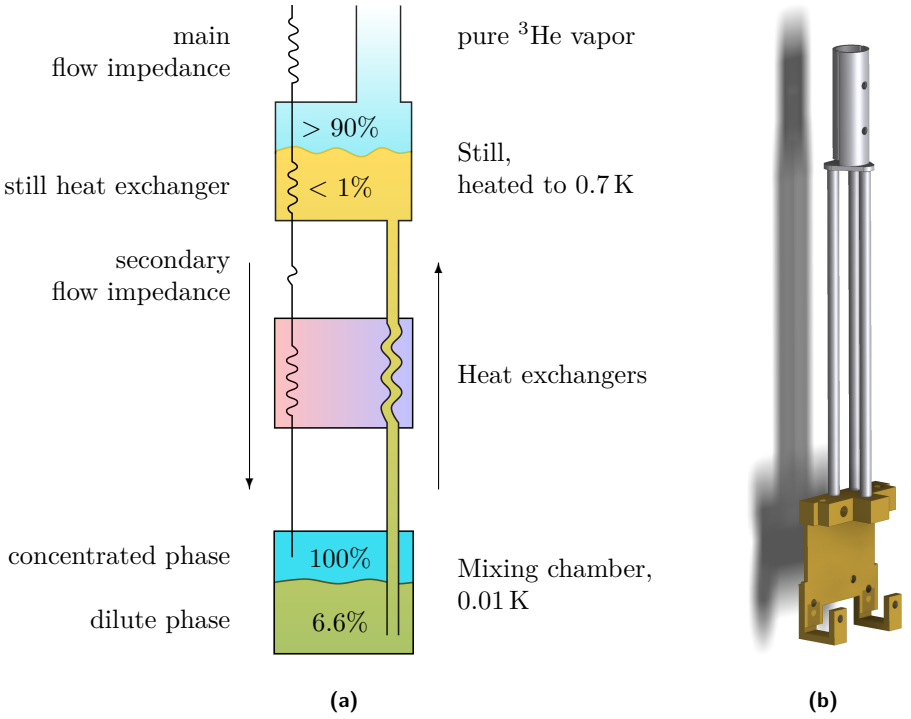

Figure 2.11: The dilution refrigerator.
In (a) a sketch of the dilution refrigerator is shown that is explained in the main text. (b) shows the sample platform build for the dilution refrigerator.

In the dilution refrigerator used for this work, a top loading *Oxford Instruments "Kelvinox"* system, the sample is immersed in the liquid Helium in the mixing chamber. While this has no consequence for the dielectric measurements it precludes measurements of thermodynamic properties. As for the PPMS a sample platform for the dilution refrigerator was constructed that is shown in figure 2.11b. Here the main purpose of the platform is fixing the sample in the center of the magnetic field, as well as controlling the sample temperature. Thus, a resistive heater and the sample thermometer are fixed onto the sample platform.

3 $TbMnO_3$

In this chapter the results of temperature- and magnetic-field-dependent permittivity measurements on $TbMnO_3$ are discussed. It turns out that at temperatures close to the phase transition in zero field, approximately 27 K, measurements with frequencies below the MHz regime show contributions of the so-called *c*-axis relaxation that could not be clearly separated from the dynamics of the phase transition. From measurements at higher frequency the dynamics could be evaluated and a critical exponent $\gamma_{\nu_p} = 0.8(2)$ was found for both temperature and magnetic field dependent data.

Contents

3.1 Introduction

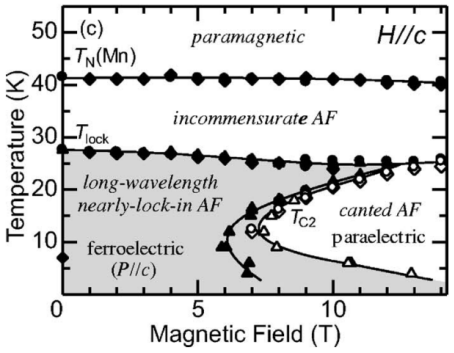

Figure 3.1: Phase diagram of $TbMnO_3$ in a [001] magnetic field obtained by dielectric constant, pyroelectric current, and magnetization measurements.[1]

The first compound to be presented in this work is chosen to be the classical multiferroic material $TbMnO_3$.

In 2003 it was reported that in $TbMnO_3$ the electric polarization can be controlled with an external magnetic field [41]. A few years later the phase diagrams for various magnetic field directions have been added [40]. More recently the relaxation processes in $TbMnO_3$ have been measured [79].

Due to the extensive existing work $TbMnO_3$ is an excellent material to probe the dynamics as function of two different control parameters, temperature and magnetic field. Using the phase information from [40], shown for $\mathbf{H} \parallel \mathbf{c}$ also in figure 3.1, it was decided to measure $TbMnO_3$ in an external magnetic field oriented in the *c*-direction where the ferroelectric polarization $\mathbf{P} \parallel \mathbf{c}$ is not shifted to a dif-

[1] Reprinted figure with permission from Kimura et al., *PRB* **71**, 224425 (2005). Copyright 2005 by the American Physical Society.

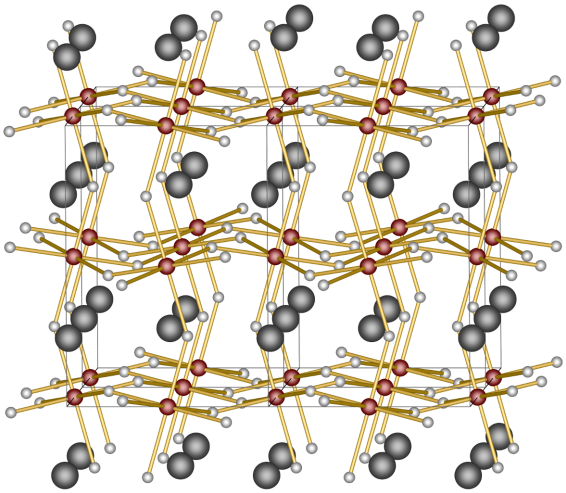

Figure 3.2: Crystal structure of $TbMnO_3$.
The perovskite structure of $TbMnO_3$ with lattice parameters from [12]. The Mn^{3+} ions (red) are surrounded by O^{2+} ions (white) forming planes of canted stripes in the *b*-direction. In the *c*-direction this planes are separated by the Tb^{3+} ions (gray).

ferent direction but completely suppressed by the magnetic field. Thus, the magnetic field can be used to drive the sample through the same phase transition—incommensurate anti-ferromagnetic (paraelectric) to nearly-locked-in anti-ferromagnetic (ferroelectric)—as the temperature at fixed or zero field.

The *c*-axis relaxation

Previously, it has been reported [27] that materials of the $R\mathrm{MnO_3}$ type with R = Eu,Gd,Tb,Dy exhibit a strong relaxation process during polarization measurements along their *c*-direction. This is also true for Y doped $\mathrm{Eu}_{1-x}\mathrm{Y}x\mathrm{MnO_3}$ [33]. In [79] this so-called *c*-axis relaxation in the $R\mathrm{MnO_3}$ compounds was examined in detail and the authors proposed that it was caused by a shallow double-well potential of the Mn^{3+} ions along the *c*-direction. They conclude that all perovskite manganites are close to a ferroelectric order-disorder instability and that the multiferroic manganites need the support of the magnetic spiral spin structure to establish long-range polar order.

3.2 The perovskite structure

The first material discovered with perovskite structure was $CaTiO_3$ that has been described in 1839 [71, 72]. Generally perovskites follow the ABO_3 schema but only when the difference in the ionic radii of the constituents is high the material crystallizes in the orthorhombic perovskite structure of space group *Pbnm*. Otherwise crystallization in a cubic structure occurs, *e.g.* in the famous dielectric material $SrTiO_3$.

In the case of $TbMnO_3$ the lattice parameters at room temperature were reported as $a = 5.301(1)$ Å, $b = 5.847(1)$ Å, and $c = 7.401(1)$ Å [12].
Figure 3.2 shows a representation of four unit cells of the corresponding structure while figure 3.3 shows cuts of the *ab*- and *bc*-plane respectively.

From the electron configuration of the Mn^{3+}, $[\mathrm{Ar}]3d^4$, and Tb^{3+}, $[\mathrm{Xe}]4f^8$, the expected paramagnetic moment of the compound can be calculated. For Mn^{3+} the Hund rules predict a spin $S = 2$ for the $3d^4$ electrons.

Due to orbital quenching caused by strong crystal fields the total paramagnetic

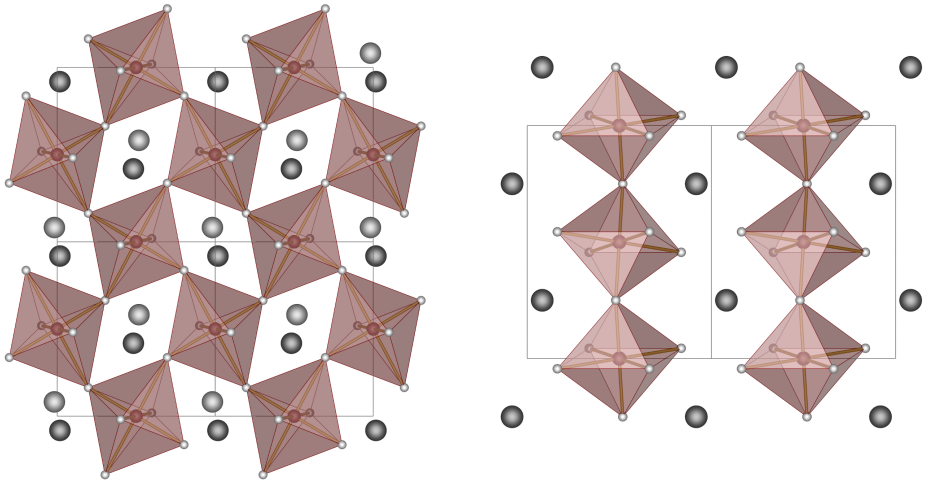

(a) *ab*-plane **(b)** *bc*-plane

Figure 3.3: *ab*- and *bc*-plane of the perovskite structure.
(a) shows a cut of the *ab*-plane of $TbMnO_3$. The Tb^{3+} ions above the plane are shown as light gray, those below the plane are dark gray. Here the corner sharing Mn-O tetrahedrons are arranged in a canted lattice. In (b) the stacking of the *ab*-planes shown in (a) is visualized. Also in this direction neighboring tetrahedrons are canted against each other.

moment is found as $p_{Mn^{3+}} = 2 \cdot \sqrt{2(2+1)}\,\mu_B = 4.9\,\mu_B$. The Tb^{3+} on the other hand hold a spin $S = 3$ and an orbital angular momentum $L = 3$. As the $4f$ shell is more than half full the total angular momentum $J = L + S = 6$ in combination with the free atom Landé factor $g = 1.5$ for Tb^{3+} leads to a paramagnetic moment $p_{Tb^{3+}} = 1.5 \cdot \sqrt{6(6+1)}\,\mu_B = 9.72\,\mu_B$.

Due to the two magnetic ions present in $TbMnO_3$ the total paramagnetic moment for the compound is found to be

$$p_{TbMnO_3} = \sqrt{p^2_{Mn^{3+}} + p^2_{Tb^{3+}}} = 10.89\,\mu_B.$$

Below $T_N = 41\,K$ the onset of sinusoidal antiferromagnetic ordering of the magnetic moments of Mn^{3+} has been observed [69]. Lowering the temperature will reduce the wavenumber of the incommensurate spin order from 0.295 at T_N down to 0.280 at $T = 27.2\,K$ [41]. Here a second transition occurs where the magnetic moments of the Mn^{3+} are ordered in a nearly commensurate antiferromagnetic structure and are oriented within the *ab*-plane. This transition is accompanied by the onset of ferroelectric order where the polarization in zero magnetic field is oriented in the *c*-direction.

Using an external magnetic field the magnetic and electric order can be suppressed as already shown in figure 3.1. While this effect is strongly dependent on the direction of the magnetic field in the following only the case of $\mathbf{H} \parallel \mathbf{E} \parallel \mathbf{c}$ will be discussed.

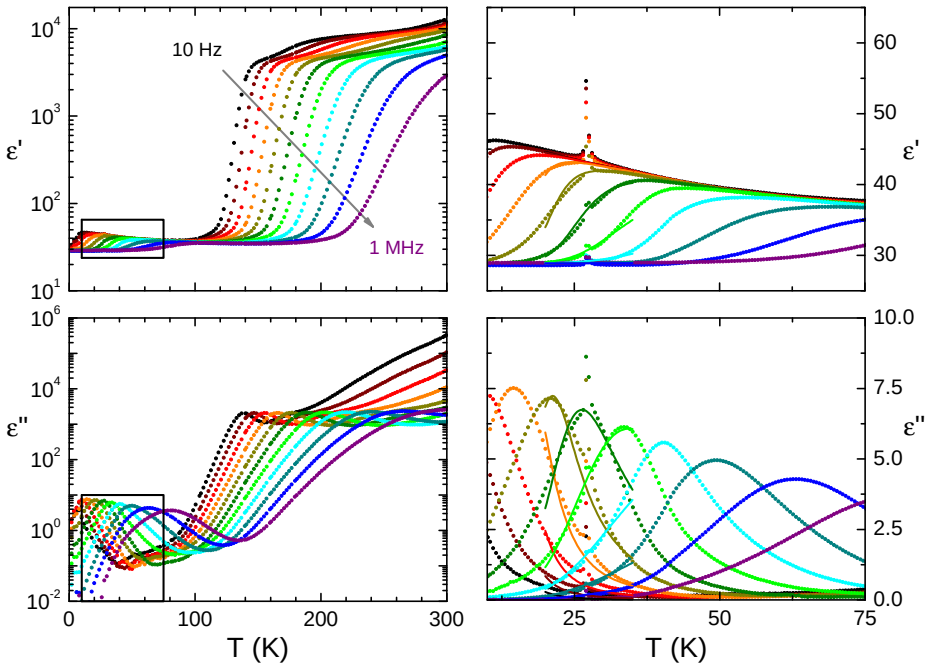

(a) Permittivity $\underline{\varepsilon}$. **(b)** Zoom of the region close to T_c.

Figure 3.4: $TbMnO_3$ in zero magnetic field.
Temperature-dependent measurement of $TbMnO_3$ in magnetic zero field are shown in (a) with both permittivity and dielectric loss in logarithmic scale. Above 100 K the results are dominated by contact effects that cause two pronounced steps. At lower temperatures the frequency-dependent dynamics of the *c*-axis relaxation are observed. The zoom in both panels in (b) shows a set of data with higher resolution (points) in the low temperature regime with fits (lines) of the model in equation (3.1) to the *c*-axis relaxation in the vicinity of the phase transition observed at 27.1 K. Table 3.1 contains the parameters obtained from the fit.

3.3 Low frequency measurements

Using frequencies up to 1 MHz the permittivity $\underline{\varepsilon}$ of $TbMnO_3$ was measured using a Novocontrol Alpha-A Analyzer with an ac voltage $U_{\mathrm{rms}} = 1\,\mathrm{V}$.

3.3.1 Temperature dependence

Initially the dynamics of the phase transition have been examined for their temperature dependence. To that end the sample was measured in a *Quantum Design "Physical Properties Measurement System"* (PPMS) in zero magnetic field, the results are shown in figure 3.4a.
At high temperatures the response of the sample is dominated by two step-like contributions that are caused by contact effects. Their origin is either extrinsic, *i.e.* the Schottky diode formed by the insulating/semi-conducting sample and the metallic capacitor plates applied for the measurement, or an intrinsic effect caused by depletion layers at grain boundaries. The exact nature of the observed

$\Delta\varepsilon$	1104(705)
τ_0	$4.99(3) \times 10^{-7}$ s
β	0.9601(7)
γ	0.990(2)
U_b	123.8(1) K
T_cw	−50(9) K
ε'_∞	28.869(4)

Table 3.1:
Best parameters found to describe the background observed of $TbMnO_3$ in zero magnetic field. The model used was a Havriliak-Negami function with the assumption of a temperature activated relaxation rate τ and a Curie-Weiss law in $\Delta\varepsilon$ given in equation (3.1).

contribution can not be distinguished from a single measurement. With decreasing temperature the relaxation time of these relaxation processes increases and the peak position shifts towards the lower end of the frequency range until they are too slow to be observed below 100 K.

Below 150 K the onset of an additional frequency-dependent contribution can be observed that is magnified for temperatures below 75 K in figure 3.4b. This relaxation process, called the *c*-axis relaxation, has previously been reported [79] and obscures the dynamics of the phase transition into the ferroelectric phase that is observed as sharp peak at the transition temperature of 27.1 K. Therefore, its contribution has to be removed before further analysis of the polarization dynamics at the phase transition can be done.

To this end a simple empirical model consisting of a combination of the Havriliak-Negami function with a temperature-dependent τ and $\Delta\varepsilon$ as discussed in chapter 1.5 on page 10 was fitted to the complete set of data between 20 and 30 K where a qualitative agreement between model and background was found. In figure 3.4b the fit results are shown as lines on top of the measured data (points).

The equation used for the description of the background was

$$\underline{\varepsilon}(\omega, T) = \frac{\Delta\varepsilon / (T - T_\mathrm{cw})}{\left(1 + \left(\mathrm{i}\omega\tau_0 \mathrm{e}^{\frac{U_\mathrm{b}}{k_\mathrm{B}T}}\right)^{\beta}\right)^{\gamma}} + \varepsilon'_\infty. \tag{3.1}$$

and the fitted parameters and their errors are given in table 3.1.

Figure 3.5 shows the phase transition in zero field after subtracting the modeled background from a measurement with very high temperature and frequency resolution.

Typically, when observing the dynamics of a ferroelectric phase transition a so-called critical slowing down is observed that can be understood as a freezing of the Goldstone mode, *i.e.* the increase of the size and lifetime of ferroelectric ordered fluctuations in the paraelectric phase. Here these fluctuations are overshadowed by the remnants of the contribution from the *c*-axis relaxation when measuring below the MHz regime as can be seen in figure 3.5. Remarkably, the peak height in the dielectric loss does not show the expected frequency dependence where the height of the peak is greatest at the lowest frequency. Instead the highest peak is observed for 316 Hz, $\Delta\varepsilon''_{316\,\mathrm{Hz}} \approx 30$, almost three times the value of the lowest frequency, $\Delta\varepsilon''_{0.1\,\mathrm{Hz}} = 11.3$.

An overview of the results obtained from the dielectric loss in the vicinity of the phase transition is given in figure 3.6. In the left panel, figure 3.6a, the dielectric loss after subtraction of the fitted background is plotted in logarithmic color code.

When comparing the data to the model data for the *c*-axis relaxation on the right (figure 3.6b) it becomes clear that the correction of the background via subtraction

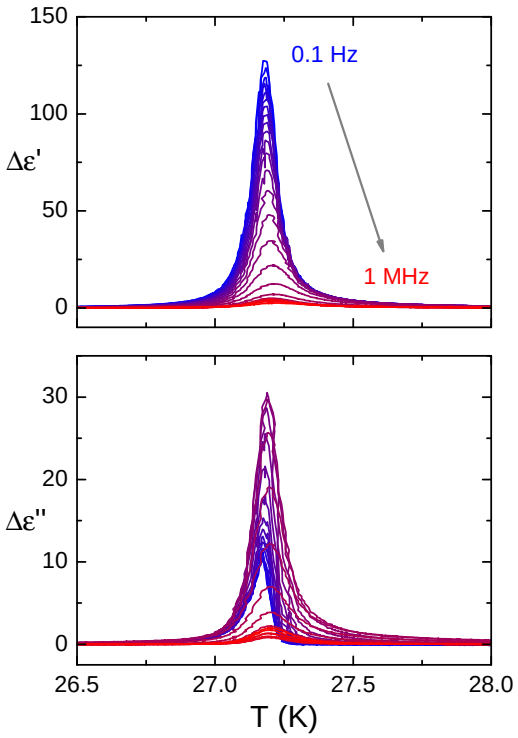

Figure 3.5:
Corrected zero field measurements.
After subtracting the background the signature of the ferroelectric phase transition can be observed more clearly. Notably the frequency dependence of the dielectric loss is atypical as the peaks do not shrink continuously with increasing frequency. The results above $T_c = 27.1\,\mathrm{K}$ only show a very weak frequency dependence. This can be seen in the lack of intersections of the individual ε'' curves above the transition temperature where the highest value is always found in the 1 kHz curve.

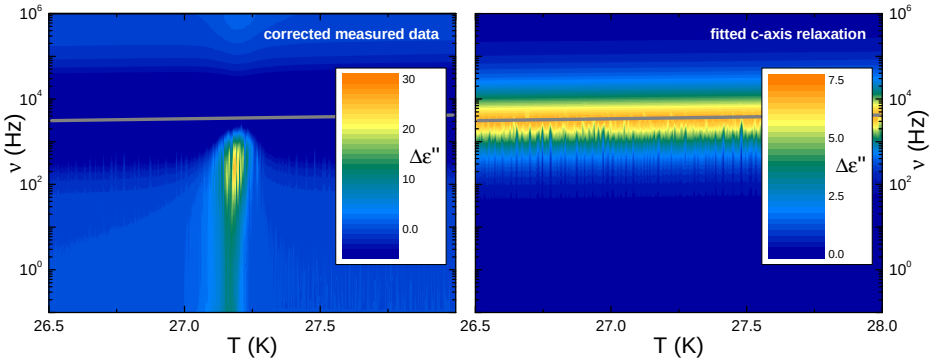

(a) Measured dielectric loss with background correction.

(b) Dielectric loss from the fit of the c-axis relaxation.

Figure 3.6: Colorplot of the dielectric loss $\Delta\varepsilon''$.
The corrected dielectric loss in (a) still shows many features that are remnants of the c-axis relaxation in (b). This can be seen *e.g.* in the peak position of the background model, the gray line that is shown in (a). Here the modeled background value is to high and the resulting $\Delta\varepsilon''$ is negative.

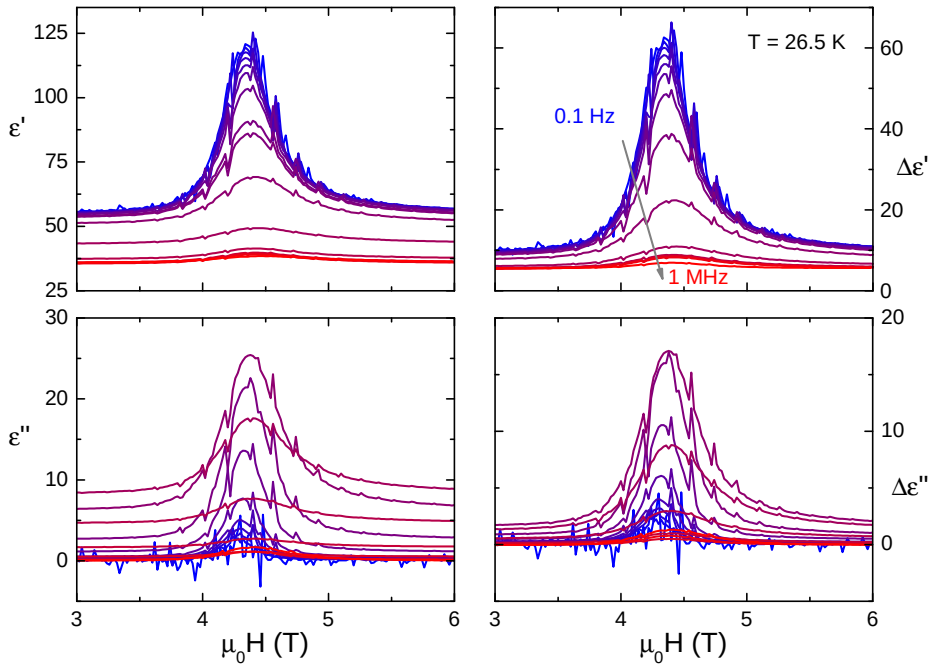

(a) Uncorrected complex permittivity. **(b)** Results with background correction.

Figure 3.7: Field-dependent measurement at 26.5 K.
Permittivity of $TbMnO_3$ as function of the magnetic field at 26.5 K. (a) Similar to the temperature-dependent measurement the peak of the phase transition at a critical field of $\mu_0 H_c = 4.3\,\mathrm{T}$ lies on top of a frequency-dependent background that seems to be independent of the magnetic field. Subtracting the model data for this temperature the visibility of the dynamics at the phase transition in (b) is enhanced. Note that the data quality in this measurement is poorer compared to the zero field measurements and a small contribution of the *c*-axis relaxation still remains after subtracting the background.

did not remove the influence of the *c*-axis relaxation completely. The temperature-dependent position of the maximum of the *c*-axis relaxation is marked by the gray line (▬) that was transferred over into the left panel. It can be observed that at the peak position the model overestimates the height of the background contribution in ε'' .

More importantly, the peak observed in the corrected data shows that the polaron contribution of the *c*-axis relaxation is amplified at the magneto-electric phase transition. This coupling of both processes prevents the evaluation of measurements without simultaneously taking both processes into account when working with low frequency data.

3.3.2 Magnetic field dependence at 26.5 K

As mentioned in the introduction of the compound the idea was to compare the dynamics of the phase transition for different control parameters. The low frequency results for the second control parameter, the magnetic field, will be discussed in the following.

Figure 3.7a shows the measurement close to the critical field $\mu_0 H_c = 4.3\,\mathrm{T}$ where the spins order incommensurate antiferromagnetic. Thereby the long range order required for ferroelectric polarization is destroyed. The field-dependent measurement also has a frequency-dependent background that in principle should be described by the same model and parameters as before when using a constant temperature $T = 26.5\,\mathrm{K}$ in equation (3.1). After the subtraction of the background a part of the c-axis contribution remains, thus showing that the model used is not a perfect description of its dynamics.

When looking at the corrected data in figure 3.7b the main difference to the zero field data observed is the data quality. For the field-dependent measurement the signal to noise ratio is significantly poorer. An explanation for this might be torque on the sample in magnetic field due to its high magnetic moment. This causes some strain on the contacts used for the dielectric measurements even though the sample was glued to the sample holder with two component epoxy adhesive.

Still, the same anomalies in the measurements are observed when compared to the zero field measurements. Again, the biggest peak in the dielectric loss is not observed at 0.1 Hz but at 560 Hz, the latter being higher by a factor of approximately 3.7.

3.4 High-voltage measurements

Using high-voltage measurements, here with $E_{ac} = 200\,\mathrm{V/mm}$, the switchable polarization and the evolution of the coercive field at the ferroelectric phase transition were observed. For these results the c-axis relaxation has not been corrected.

Temperature-dependent measurements

First the data of a temperature-dependent measurement in zero field is plotted in the left panels of figure 3.8. Here the same behavior as discussed in the prior sections is observed where the frequency-dependent c-axis relaxation causes a step in $\varepsilon'(\nu)$ that is accompanied by a peak in $\varepsilon''(\nu)$. The temperature dependence of this contribution can be seen in the 3.16 kHz curve that is located at the center of the step and shows a discernible downward gradient towards lower temperatures. In the plot of ε' the gray (—) curve marks the offset $\varepsilon_\infty = 26.292$ chosen from the lowest value measured at 100 kHz.

Using this offset the switchable polarization $P_{sw} = \pi/4\,\varepsilon_0 |\Delta\varepsilon_1|\, E_{ac}$ can be calculated from $\underline{\varepsilon}$ with $|\Delta\varepsilon_1| = \sqrt{(\varepsilon' - \varepsilon_\infty)^2 + \varepsilon''^2}$. The corresponding plot in the upper frame of figure 3.8b shows that the c-axis relaxation causes a finite amount of switchable polarization above the phase transition, roughly $20\,\mu\mathrm{C/m^2}$ at 30 K. At the transition temperature up to $130\,\mu\mathrm{C/m^2}$ can be switched. Below T_c the lowest frequencies seem to be slightly higher than above but due to the limited temperature range measured in the ferroelectric phase this can not be seen clearly.

Also the coercive field can be evaluated via $\varepsilon''/|\Delta\varepsilon_1| \approx E_{crcv}/E_{ac}$ as shown in the lower panel of the same figure. Here the coercive field for frequencies of 3.61 kHz and lower increases at the phase transition while it is observed to be reduced for higher frequencies. Once $\varepsilon''/|\Delta\varepsilon_1|$ is of the order of 1 the applied electric field is insufficient to switch the polarization.

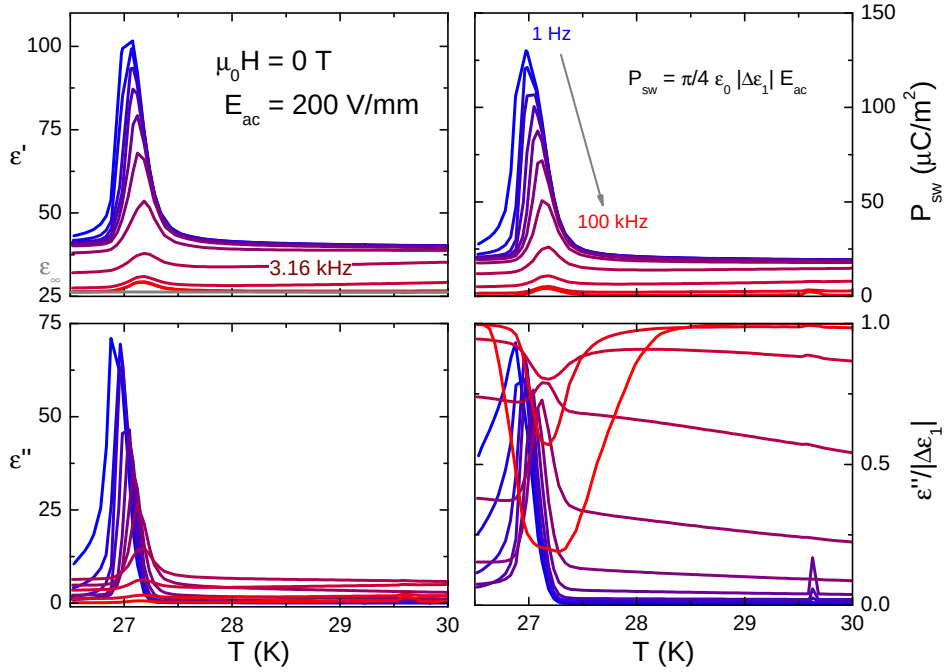

(a) Permittivity $\underline{\varepsilon}$. **(b)** P_{sw} and $\varepsilon''/|\Delta\varepsilon_1|$

Figure 3.8: High-voltage measurements in magnetic zero field.
In (a) the measured complex permittivity is shown as function of temperature. In gray (▬) the offset $\varepsilon_\infty = 26.292$ is shown that was used for the calculation of P_{sw} (upper panel in (b)) and $\varepsilon''/|\Delta\varepsilon_1|$ (lower panel in (a)). The switchable polarization at low frequencies is observed to be highest at the phase transition and drops down sharply in the ferroelectric phase.

Magnetic field dependent measurements

Measurements with the same electric ac field were done magnetic field dependent at 26.5 K as shown in figure 3.9. Here the background caused by the *c*-axis relaxation is again observed with same the frequency of the central curve, 3.16 kHz, as observed in zero magnetic field. Compared to the field-dependent measurements with lower electric field it stands out that both the 1 and 3.16 Hz curves do not coincide with the curves at higher frequencies.

Calculating the switchable polarization for this measurement, here the offset $\varepsilon_\infty = 26.35$ was again chosen from the 100 kHz curve, emphasizes this observation in the upper right panel. In the inset of this panel the frequency dependence of the switchable polarization, $P_{\mathrm{sw}}(\nu)$, is plotted for two fields far below (0 T, black •) and above (8 T, green •) the critical field. Here an additional low-frequency contribution in the ferroelectric phase is observed. The origin of this contribution is either the spontaneous polarization of the ferroelectric phase or a change in the properties of the *c*-axis relaxation due to the coupling between the polaron and the internal fields present in the ferroelectric phase.

Its exact nature can not be discerned form this measurements alone.

The field dependence of $\varepsilon''/|\Delta\varepsilon_1| \propto E_{\mathrm{crcv}}$ in the lower right frame is similar to the plot for the zero field measurements. At the phase transition frequencies up to 3.16 kHz show an increase of the coercive field while it is reduced for higher frequencies.

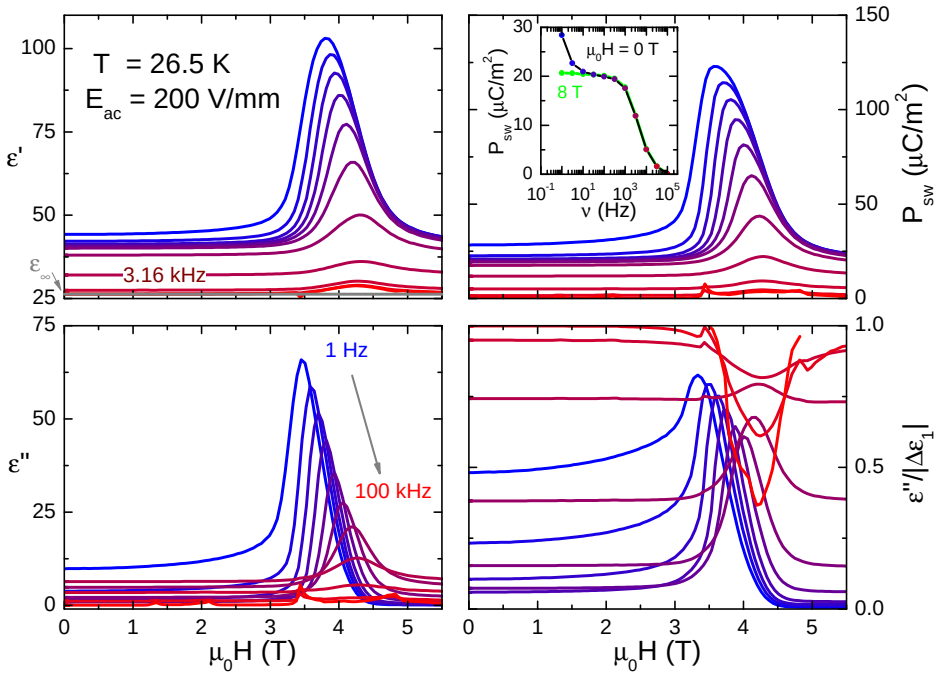

(a) Permittivity $\underline{\varepsilon}$. **(b)** P_{sw} and $\varepsilon''/|\Delta\varepsilon_1|$.

Figure 3.9: High-voltage measurements at 26.5 K.
For the field-dependent measurements the plot is structured identical to the temperature-dependent results in figure 3.8. Here the offset is slightly higher, $\varepsilon_\infty = 26.35$, and the background from the c-axis relaxation is independent of the magnetic field for high frequencies. The results show quantitative agreement with the measurements in zero field and the additional inset in the P_{sw} panel in (b) shows the frequency dependence of the switchable polarization in the ferro- and paraelectric phases. At 8 T the c-axis relaxation causes a frequency-dependent contribution (green •). In zero field for low frequencies an additional contribution to P_{sw} can be observed.

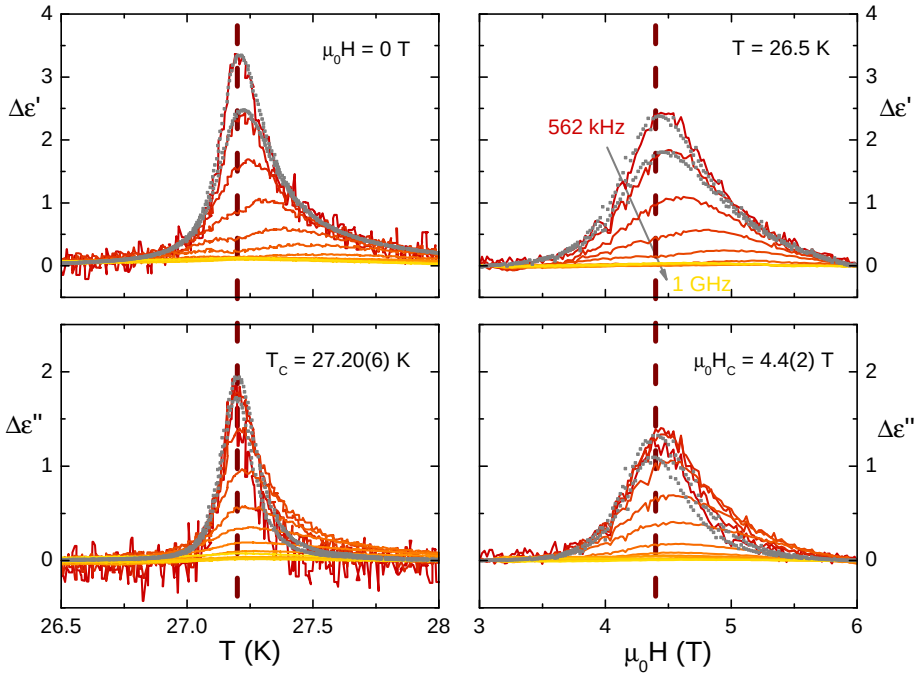

Figure 3.10: High-frequency measurements on $TbMnO_3$.
Measurements on $TbMnO_3$ from 562 kHz to 1 GHz in zero field (left) and at 26.5 K (right) exhibit a strong resemblance. The gray (•) curves are data from the previous low-frequency sections shown to demonstrate the agreement between the different methods of measurement. At 5.62 MHz the 'dispersion' minimum is observed in both measurements.

3.5 High-frequency measurements

To find data free of the major contributions of the c-axis relaxation measurements at high frequencies up to 1 GHz were performed in zero field and field-dependent at 26.5 K.

At frequencies above 1 MHz the frequency-dependent data is subject to an instrumental offset due to unwanted inductive contributions from the cables used in the setup that depend, amongst others, on their temperature distribution. To compensate this offsets figure 3.10 shows the results corrected for a linear offset in T or B as the c-axis relaxation can be neglected for frequencies above 1 MHz.

The panels on the left show permittivity and dielectric loss in zero field, those on the right feature the magnetic-field-dependent data. For comparison with the previous results the lowest two frequencies, 562 kHz and 1 MHz, are also shown from the low-frequency data in gray (•). They are in very good agreement with the results from the high-frequency measurements.

In this figure the similarity between both temperature- and magnetic-field-dependent measurements is apparent and the 'dispersion' minimum known from ferroelectric materials [61, 30, 60] is unanimously observed at 5.62 MHz. The reduced peak height in the field-dependent measurement can be attributed to the reduced temperature in this measurement compared to the critical temperature in zero field. Using the 'dispersion' minimum and the peak position at 1 MHz both $T_\mathrm{c} = 27.20(6)\,\mathrm{K}$ and $\mu_0 H_\mathrm{c} = 4.4(2)\,\mathrm{T}$ can be found and are marked by dashed lines in the plots.

To compare the dynamics the critical exponents for both the field- and temperature-dependent measurements have been evaluated. For both measurements they can be found via $1/\Delta\varepsilon \propto \nu_\mathrm{p} \propto |H - H_\mathrm{c}|^{\gamma_H}$ or $1/\Delta\varepsilon \propto \nu_\mathrm{p} \propto |T - T_\mathrm{c}|^{\gamma_T}$ respectively. The evaluation of the peak positions for the data shown in figure 3.10 was done by fitting a Debye relaxation, equation (1.15) on page 10, in plots of $\Delta\underline{\varepsilon}(\nu)|_{T=\mathrm{const}}$ or $\Delta\underline{\varepsilon}(\nu)|_{H=\mathrm{const}}$. Some exemplary spectra from the measurements in magnetic zero field with the corresponding fits are plotted in figure 3.11 to demonstrate the agreement of data and fit.

Similar fits were done for many additional curves and the resulting parameters ν_p and $\Delta\varepsilon$ are shown in figure 3.12. There the field-dependent quantities, $\nu_\mathrm{p}(H)$ and $\Delta\varepsilon(H)$, are presented on the left next to their temperature-dependent counterparts on the right. All four plots show the parameters from the Debye fits as black dots and fits of

$$\Delta\varepsilon(x)^{-1} = a \cdot |x/x_\mathrm{c} - 1|^{\gamma_x} \qquad \text{or} \qquad \nu_\mathrm{p}(x) = a \cdot |x/x_\mathrm{c} - 1|^{\gamma_x}$$

where $x \in \{T, B\}$ in red (▬). For all fits T_c and H_c were fixed at 27.2 K and 4.2 T respectively. The ranges used for fitting are marked with gray background, and their choice is explained with help of the lower right panel, $1/\Delta\varepsilon(T)$. When correcting the offset in the data specific temperatures were used for the subtraction of the linear background making their selection a very important issue for evaluation of $\Delta\varepsilon$. If the selected temperatures are not far enough away from the phase transition the fluctuation contributions are not completely gone and the resulting $\Delta\varepsilon$ is to small. In the lower frames the blue dots demonstrate the influence of the absolute value of the offset on the data. They were created by adding 0.05 to $\Delta\varepsilon$ before calculating the inverse used for fitting. The deviation between both datasets was the basis for the chosen areas with different weights in the fits.

Fitting the critical exponent for both sets of data, the red and blue curves in the plot, reveals a difference of 0.2, thus demonstrating that the absolute accuracy

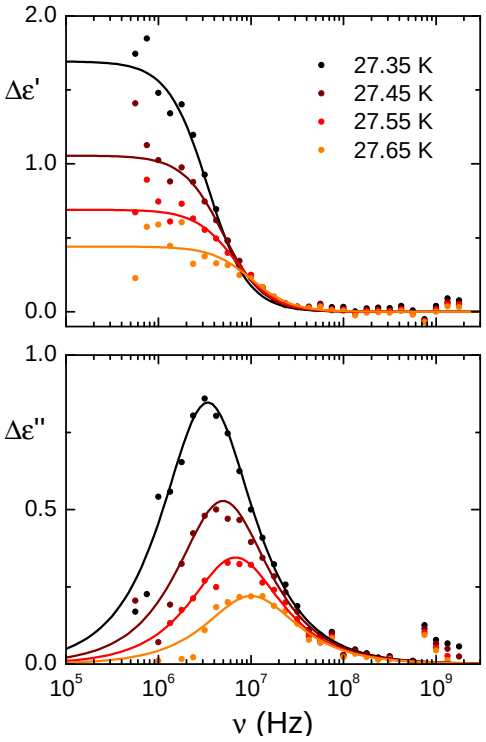

Figure 3.11: Frequency-dependent spectra in zero field. Above the transition temperature of $T_c = 27.2\,\mathrm{K}$ the fluctuation dynamics show critical slowing down. The frequency-dependent measured data (point) can be described by a Debye relaxation (lines).

of the results found from $\Delta\varepsilon$ is poorer compared to the results from the peak position. For both the magnetic-field- and temperature-dependent measurements the fitted exponents are not in agreement but are both greater then 1.

For the peak positions ν_p the results are not influenced strongly by the absolute value of the subtracted background. Here the fits of the exponents (red) are in qualitative agreement and find $\gamma_{H,\nu_\mathrm{p}} \approx \gamma_{T,\nu_\mathrm{p}} \approx 0.8$. Both measurements can also be described reasonably well with curves using $\gamma_{H,T} = 1$ (green), thus the critical exponent as found from the peak positions in the fluctuation regime will be given as $\gamma_{H,\nu_\mathrm{p}} = \gamma_{T,\nu_\mathrm{p}} = 0.8(2)$.

For $DyMnO_3$, a sister compound of $TbMnO_3$, it has been proposed [78] that the order-disorder type of the phase transition changes the dynamical properties. Here the P^2M^2 coupling is said to lead to an Arrhenius-like contribution to the temperature dependence of ν_p. In this paper a pseudo spin model was developed that predicts the dynamical properties above the phase transition as:

$$\nu_\mathrm{p} = \frac{\nu_0}{\pi} \cdot \frac{T - T_c}{T} \exp\left(-\frac{E_a}{k_\mathrm{B} T}\right).$$

At the same time the relaxation strength above the phase transition is proportional to

$$\Delta\varepsilon^{-1} = \frac{\varepsilon_0 k_\mathrm{B}}{n q^2 (\Delta x)^2} (T - T_\mathrm{c}),$$

which is basically a power law with exponent 1 that was already fitted. This alternative proposition for the dynamical properties has also been fitted for ν_p and is plotted in figure 3.12 as solid black (—) lines. For this fits the critical field and temperature have again been kept fixed and for the field-dependent fit the

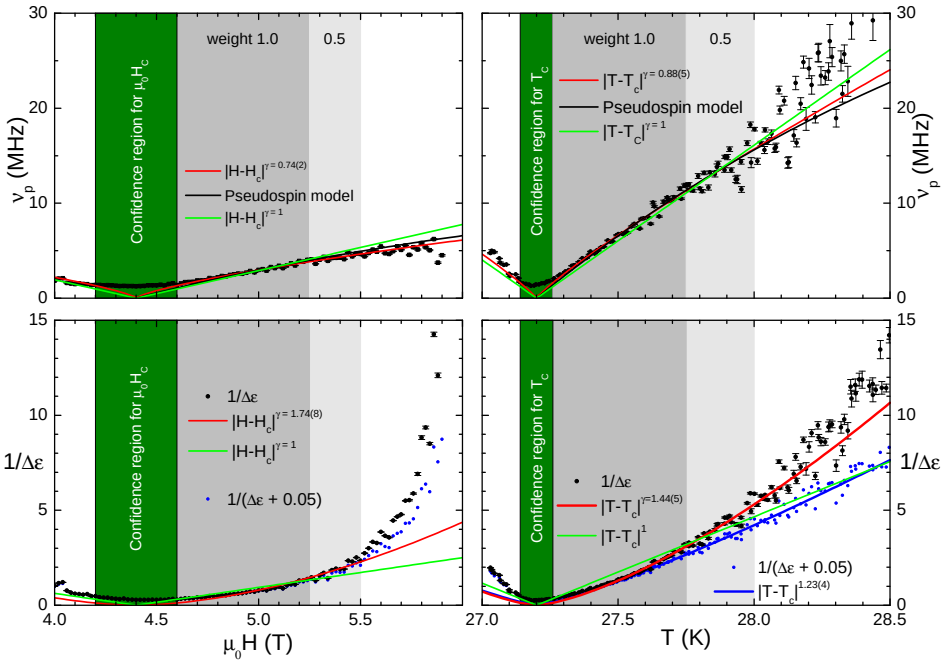

(a) $T = 26.5\,\mathrm{K}$ **(b)** $\mu_0 H = 0\,\mathrm{T}$

Figure 3.12: Critical exponents.

Different models for the critical behavior are fitted to both ν_p (upper panels) and $1/\Delta\varepsilon$. The coloring of the background indicates the weight and range of points used for the fits. In green (▬) the critical exponent $\gamma = 1$ as well as the critical field/temperature have been fixed. For the red (▬) fits only the latter was fixed and the black lines in the upper panels are fits of the pseudospin model.

The fit of ν_p finds $\gamma \approx 0.8(2)$ for both measurements and no significant deviation between the description with this critical exponent and the pseudospin model. For the relaxation strength the subtracted offset is very important and the results for the critical exponents are less reliable, as discussed in the main text.

Arrhenius contribution used the activation energy found from the zero magnetic field measurement and the fixed temperature of 26.5 K. While this model also describes the dynamics an advantage compared to the simpler model of critical exponents could not be observed.

3.6 Conclusion

While $TbMnO_3$ is an interesting candidate for the observation and comparison of the fluctuation dynamics for different control parameters, T and H, these results are masked by additional intrinsic contributions to the polarization dynamics. Measurements below $\lesssim$ 1 MHz show a strong coupling between the c-axis relaxation and the polarization created at the magneto-electric phase transition observed at 27.20(6) K. This coupling leads to an amplification of the polaron contribution of the c-axis relaxation due to the internal fields present at the phase transition.

Simple subtraction of the contribution of this relaxation process is not sufficient to clearly see the critical dynamics at the phase transition. As shown in the previous sections not only temperature-dependent data but also the magnetic-field-dependent measurements are strongly influenced by this background contribution. The most obvious consequence of the mixing of both dynamical processes is the anomalous frequency dependence of the dielectric loss where the peak is highest not at the lowest frequency but at 560 Hz. Therefore, the low-frequency dynamics at the phase transition could not be evaluated.

Using high electric ac fields both the dynamics and switchable polarization close to the phase transition were observed. Here the c-axis relaxation causes the observation of switchable polarization even in the paraelectric phase. At the phase transition a maximum switchable polarization of roughly 130 $\mu C/m^2$ was observed for 1 Hz in both measurements. From the frequency dependence of the switchable polarization in zero field it stands to reason that this value would be even higher at lower frequencies as a saturation is not observed. Instead it could be seen that the c-axis relaxation dominates the polarization dynamics both in the para- and ferroelectric phases. In the latter an additional contribution could be observed mainly for frequencies below 10 Hz. The cause of this contribution could be either the pure ferroelectric polarization in this phase or a change in the c-axis relaxation due to the coupling between the polaron and the internal electric fields present in the ferroelectric phase.

For frequencies above 1 MHz the fluctuation dynamics could be described qualitatively in terms of critical exponents. The results obtained from measurements in the MHz regime show critical slowing down, $\gamma > 0$, at the phase transition. Also the critical exponents γ_H and γ_T from the evaluation of the peak position ν_p are both of the order of 0.8. Due to the uncertainty in T_c and H_c that have a strong influence on the fit result, the exponent can only be given as $\gamma_{\nu_\mathrm{p}} = 0.8(2)$. The evaluation of the critical exponent from the relaxation strength $\Delta\varepsilon$ depends strongly on the chosen offset and therefore only a qualitative statement of $\gamma_{\Delta\varepsilon} \gtrsim 1$ can be made.

4 $LiCuVO_4$

The following chapter comprises both magnetic and dielectric measurements on $LiCuVO_4$ at very low temperatures. Here the anisotropy of the material is demonstrated via orientation-dependent magnetization measurements that also show the 1D nature of the compound at higher temperatures. Additionally, the phase diagrams for two orientations, namely $\mathbf{H} \parallel [001]$ and $\mathbf{H} \parallel [100]$, are explored down to very low temperatures using dielectric spectroscopy. A change of the dynamics at the phase transition is observed below 0.4 K. Here nearly gapless soliton excitations are observed that were predicted in theoretical work.

Contents

4.1 Introduction

One of the first experiments that started the interest in $LiCuVO_4$ was the revelation of the low dimensionality of its magnetic structure that was apparent in temperature-dependent measurements of the magnetic susceptibility [4]. Thenceforward the interest has focused on the quasi one dimensionality of the Cu^{2+} spin system[1] with $S = J = 1/2$ as Cu^{2+} is the only magnetic ion in $LiCuVO_4$. At elevated temperatures the three dimensional correlations can be neglected.

The low dimensionality of the spin system can already be inferred from the structure of $LiCuVO_4$. It has an orthorhombic distorted inverse spinel structure[2] of the space group *Imma* with lattice parameters $a = 5.662(1)$ Å, $b = 5.809(1)$ Å, and $c = 8.758(2)$ Å [49]. The spin 1/2 copper oxide ions form chains oriented along the crystallographic [010] direction as shown in detail in figures 4.1 and 4.2. In the [100] direction the copper oxide chains are separated by VO_4 tetrahedrons, in [001] direction by the Li atoms, all of which are non-magnetic.

[1] The $3d^9$ configuration of a free Cu^{2+} ion theoretically results in $S = 1/2$, $L = 2$, and $J = 5/2$. Due to the strong crystal field the orbital angular moment is quenched ($L = 0$) and thus the total angular moment is equal to S.

[2] The original compound of this structure, $MgAl_2O_4$, was dicovered by F. Rinne in 1928.

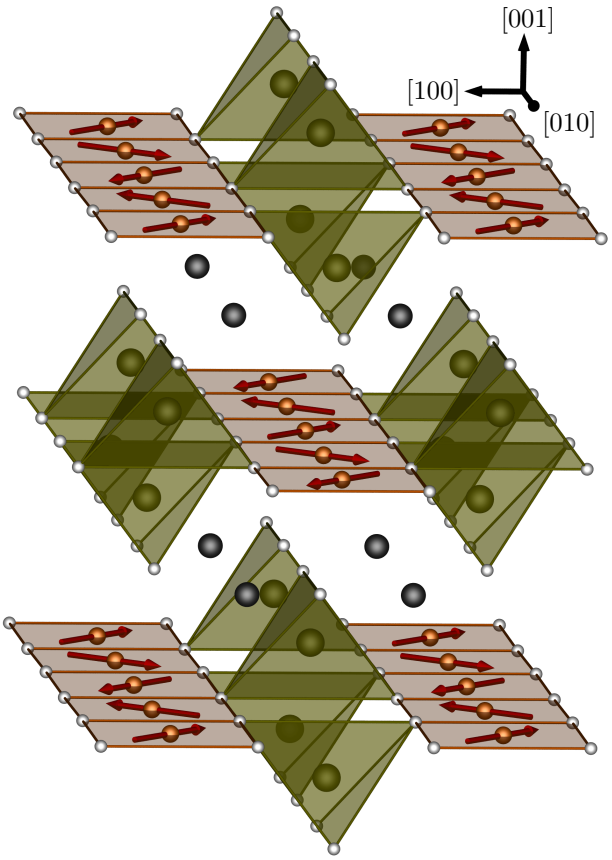

Figure 4.1: Crystal structure of $LiCuVO_4$.
Structure of $LiCuVO_4$ with copper oxide chains along the [010] direction. The copper spins form cycloids in the (001)-plane. Due to the spin supercurrent mechanism (equation (4.1)) this leads to a polarization in the crystallographic [100] direction.

Frustration

Many measurements on poly- or single crystalline samples could be explained by antiferromagnetic exchange interactions between neighboring Cu^{2+}, for example NMR [88] and ESR [48] data, when elastic neutron diffraction experiments were done at low temperatures. These experiments showed an additional magnetic structure with an incommensurate propagation vector $\mathbf{k} = (0, 0.532, 0)$ that was attributed to frustration along the Cu^{2+} chains due to competing exchange interactions between nearest (J_1) and next nearest neighbors (J_2) [26]. Furthermore, adjoining spins were found to enclose an angle of $\Phi_{\text{n.n.}} \approx 90°$ and the local spin axes are rotated by 44° with respect to the [100] direction of the crystal. Figure 4.2 shows the resulting spin configuration in the crystal lattice and explains the designations of the different coupling parameters.

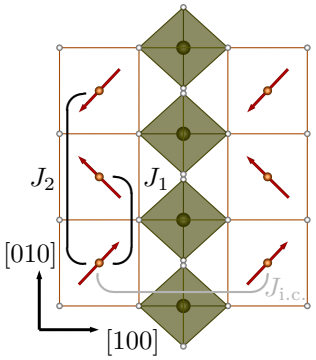

Figure 4.2: Magnetic coupling parameters in the (001) plane of $LiCuVO_4$.

The nearest neighbor coupling constant $J_1 < 0$ is ferromagnetic while the next nearest neighbor coupling $J_2 > 0$ is of antiferromagnetic nature. The interchain coupling $J_{\text{i.c.}}$ is ferromagnetic but very small, suitable for the 1D nature of the magnetic structure at temperatures above 10 K.

The typical disorder in 1D systems that never order completely is enhanced by the interplay of both ferro- and antiferromagnetic coupling within the 1D spin chain that leads to a frustrated ground state.

Multiferroic phase

This frustration of the Cu^{2+} ions and the resulting cycloidal spin order of the Cu-O chains at low temperatures makes $LiCuVO_4$ a good candidate for having additional ferroelectric properties as the transition into (planar) spiral spin order is accompanied by a breaking of the inversion symmetry. Indeed, a multiferroic phase transition at approximately 2.3 K in zero magnetic field was found [59]. Neutron diffraction experiments at 1.6 K show no structural change compared to higher temperatures and only a slight temperature induced lattice contraction [45] demonstrating that this phase transition is of second order.

The spontaneous polarization $\mathbf{P}$ of the ferroelectric phase is driven by the spin supercurrent mechanism [57]. Using the propagation vector $\mathbf{k}$ that is parallel to [010] and the the outer product of neighboring spins $\mathbf{S}_i$ and $\mathbf{S}_j$ parallel to [001] the direction of polarization from the cycloidal spin structure can found as being parallel to [100]:

$$\mathbf{P} \propto \mathbf{k} \times (\mathbf{S}_i \times \mathbf{S}_j). \tag{4.1}$$

$LiCuVO_4$ in a magnetic field

Above, only the physical properties in zero magnetic field were discussed. As the ground state is determined by the frustrated magnetic interactions it has to be expected that it depends on the magnetic field. Furthermore, from the one-dimensionality of the magnetic system a dependence on the direction of the mag-

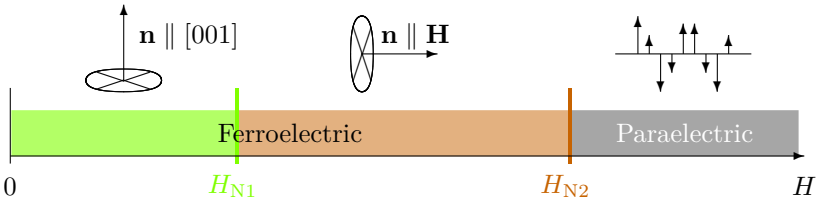

Figure 4.3: Magnetic field dependent spin configurations in $LiCuVO_4$. Below H_{N1} $LiCuVO_4$ is in a cycloidal spin ordered phase where the spins are oriented in the (001) plane. At H_{N1} the plane of spin orientation is tilted to be perpendicular to the magnetic field. Above H_{N2} the cycloidal spin order is destroyed in favor of a collinear spin-modulated phase.

netic field has to be considered with a pronounced difference between magnetic fields in the (001) plane and perpendicular to it.

Both these expectations were proven experimentally, first in angular-dependent NMR and antiferroelectric resonance measurements at relatively small fields [9] and later on with field-dependent magnetization measurements up to 60 T [86]. The latter paper concludes that the magnetic field can shift the plane of the spin cycloids to be perpendicular to the magnetic field for an angular-dependent critical field $2.5\,\mathrm{T} \leq \mu_0 H_{N1} \leq 3.0\,\mathrm{T}$ if applied in [100] or [010] direction. Using equation (4.1) and keeping in mind that $\mathbf{H} \parallel \mathbf{S}_i \times \mathbf{S}_j$ is enforced in this phase the polarization direction can be calculated with

$$\mathbf{P} \propto \mathbf{k} \times \mathbf{H}. \tag{4.2}$$

The magnetic field dependence of the spin systems at low temperatures is sketched in figure 4.3. Applying a magnetic field $H > H_{N1}$ in [100] direction will, therefore, change the polarization direction from the [100] direction to the [001] direction. A magnetic field in [010] direction on the other hand will destroy the polarization as $\mathbf{k}$ and $\mathbf{H}$ are parallel and their outer product vanishes. Lastly, a magnetic field in the [001] direction should show no phase transition at H_{N1} as the spins are already perpendicular to the [001] direction. In this case only one phase transition is observed, from ferroelectric to paraelectric, and the corresponding critical field is called H_N. Measurements of polarization and permittivity in this field direction are discussed in section 4.4.1.

Above a temperature-dependent critical magnetic field H_{N2} (for $T \to 0\,\mathrm{K}$: $\mu_0 H_{N2} \approx 7.4\,\mathrm{T}$) the chiral spin order is suppressed in favor of a modulated collinear spin order where the outer product $\mathbf{S}_i \times \mathbf{S}_j$ in equation (4.1) vanishes. Therefore, this phase transition changes the electric properties from ferroelectric in the chiral phase to paraelectric in the collinear phase.

The temperature and magnetic field dependence of the polarization in $LiCuVO_4$ has previously been studied with frequencies up to 10 kHz and temperatures down to 1.5 K by Schrettle et al. [80] who could confirm the predictions for the dependence of the polarization on the magnetic field.

4.2 Theoretical description and literature

In literature the values of the coupling constants J_1 and J_2 have been heavily debated and as of now no final consensus has been reached. The nature of the

the coupling constants J_1 and J_2 has been examined from susceptibility [15] and neutron diffraction data [21]. Both demonstrated that the nearest neighbor coupling J_1 has to be ferromagnetic ($J_1 < 0$) while the next nearest neighbor coupling $J_2 > 0$ is antiferromagnetic and that the antiferromagnetic coupling is stronger, $|J_1| < J_2$. This results were also endorsed by ellipsometric measurements [51] and additional inelastic neutron data [22]. In the latter publication both the experimental as well as theoretical data from a 3D spin wave model point towards $J_1/J_2 \approx -0.7$ and $J_1 = -2.4\,\mathrm{meV}$. At the same time Sirker [83] used a density matrix algorithm to evaluate susceptibility data where they find $J_1/J_2 = -1.6$ to -2.0, proposing that the ferromagnetic coupling is dominant. Later it was argued [65] that the spin structure factor has a non universal relation to the coupling constants and in the same paper the inelastic neutron data was reevaluated. This leads to $J_1 = -6.95\,\mathrm{meV}$ and $J_1/J_2 = -1.5$. The dynamical spin structure factor was also investigated in a second paper [70] that concluded with a similar ratio $J_1/J_2 = -2$ as was proposed before.

A simple Hamiltonian with z-axis anisotropy,

$$\mathcal{H} = \sum_{n=1}^{2} \sum_{j} J_n \left[\mathbf{S}_j \mathbf{S}_{j+n} + (\Delta - 1)\, S_j^z S_{j+n}^z \right],$$

has been the most promising approach in the description of $LiCuVO_4$. The anisotropy parameter $0 \ll \Delta < 1$ indicates easy-plane anisotropy. For Cu^{2+} the easy-plane anisotropy is small and caused by single ion anisotropy driven by crystal field split d-states that interact via spin-orbit coupling [50].

Such a frustrated complex spin chain system with competing nearest and next nearest neighbor interactions has been proposed to posses a finite but very tiny energy gap in an extended region of the coupling constant space.

The strong reduction of the energy gap is caused by frustration enhanced quantum fluctuations [36]. This region of the phase diagram was evaluated in detail in a series of papers [25, 23, 24] where among others a similar argument was made for the dielectric response. Here the dielectric response from phasons and chiral solitons was proposed to be gapless.

The corresponding processes can be explained with figure 4.4. The top row of the figure shows a spin chain with purely positive (L) chirality. In this case the spins from left to right are always rotated counterclockwise by $\approx 90°$. Decomposing the spin chain into smaller blocks containing two spins reveals the existence of only two distinct patterns a (blue) and b (yellow). This dimerization of the spins is not unique, as its starting point could also be shifted by one spin resulting in the observation of two different patterns.

The simplest excitation of the dimerized system is the transformation of one dimer of type a to type b, *i.e.* the flipping of two adjacent spins j and $j + 1$. This changes the chirality at the border between the three identical dimers from positive to negative (R) forming kinks between different parts of the 1D spin chain. Here the displacement of electric charges is of opposite sign compared to the rest of the spin chain.

These chiral solitons can now traverse through the spin chain when adjacent dimers exchange their positions. Though in theory the soliton movement is gapless it was argued [25] that it can acquire a small gap in 1D multiferroic materials like $LiCuVO_4$ due to spin anisotropy or an in-plain magnetic field.

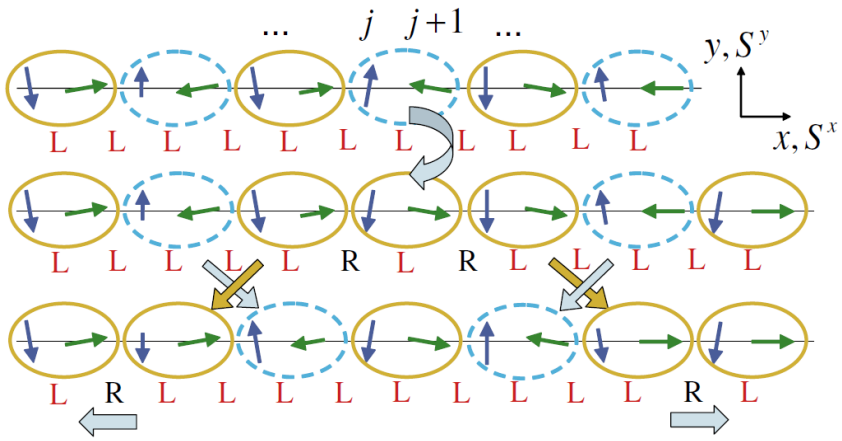

Figure 4.4: Soliton excitations.
Model for gapless soliton excitations in dimerized $LiCuVO_4$.
Reprinted figure with permission from Furukawa et al., *JPSJ* **77**, 123712 (2008). Copyright 2008 by the Physical Society of Japan.

	J_{1D}		g	p_{LiCuVO_4}	T_{cw}
H ∥ [100]	43.7 K	3.8 meV	2.25	1.836(2) μ_B	−9.6(4) K
H ∥ [001]	43.7 K	3.8 meV	2.43	2.047(1) μ_B	−18.8(2) K

Table 4.1: Results from the scaling of the 1D Heisenberg chain (J_{1D} and g) in figure 4.6 as well as the paramagnetic moment p_{LiCuVO_4} and T_{cw} from Curie-Weiss fits at temperatures between 150 and 300 K.

4.3 Magnetization

Using a SQUID (*Quantum Design MPMS*) the magnetization of $LiCuVO_4$ was measured for different magnetic field directions and temperatures down to 1.8 K.

At temperatures above 150 K (gray area in figure 4.5) the susceptibility can be described by a Curie-Weiss law (red —). The fits yield an anisotropic paramagnetic moment that is strongest for magnetic fields in [001] direction, see table 4.1. From the [Ar]d^9 electron configuration ($S = J = 1/2$) the predicted paramagnetic moment is

$$p_{J=1/2} = g \cdot \sqrt{J\,(J+1)} \cdot \mu_B \approx g \cdot 0.866\,\mu_B.$$

Due to the structural anisotropy g depends on the crystallographic axis and using values from ERS measurements [48], $g_{\perp[001]} = 2.05, g_{\parallel[001]} = 2.35$, this leads to $P_{\perp[001]} = 1.775\,\mu_B$ and $P_{\parallel[001]} = 2.035\,\mu_B$ that are both very close to the results from the Curie-Weiss fits. The Curie temperature from the fits has the same order of magnitude when compared to the results from the ESR measurements. From the negative sign of the Curie temperature the antiferromagnetic nature of the compound at lower temperatures can be inferred.

The upper inset shows both field cooled (fc) and zero field cooled (zfc) measurements where a splitting close to 50 K is observed. In the lower inset the splitting is plotted as function of temperature and fits above and below 50 K reveal the split-

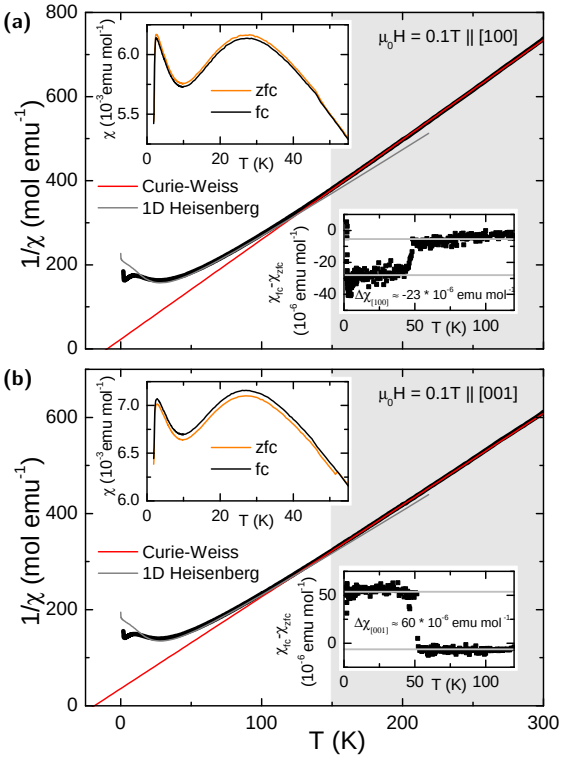

Figure 4.5: $1/\chi$ data with 1D Heisenberg chain data.
Plots of $1/\chi$ measured for 0.1 T. (a) shows the results for $\mathbf{H} \parallel [100]$. Using a Curie-Weiss fit (red ▬) the high temperature regime above 150 K can be described nicely. Model data for a 1D antiferromagnetic Heisenberg-chain (gray ▬) reasonably describes the broad feature at 28 K. The insets show the splitting between zfc and fc measurements caused by a slight oxygen contamination in the sample space as discussed in the main text. Similar measurements for $\mathbf{H} \parallel [001]$ are presented in (b). The results from the Curie-Weiss fits and the scaling factors used for the 1D model data are given in table 4.1.

ting $\Delta\chi = \chi_{\mathrm{fc}} - \chi_{\mathrm{zfc}}$ to be $\Delta\chi_{[100]} = -23 \times 10^{-6}$ emu/mol. No intrinsic features are expected in this temperature regime, instead a jump in χ at this temperature may be attributed to molecular oxygen. The amount of O_2 trapped in the sample space of the SQUID can be estimated using measurements on pure oxygen from [90]. In this paper the authors show that O_2 undergoes a phase transition from a cubic phase (γ-phase) with space group *Pm3n* into the rhombohedral β-phase (space group *R3m*) at $T_{\beta\gamma} = 43.8$ K. At this transition temperature χ_{O_2} exhibits a sharp drop of about 180×10^{-6} emu/g. Combining the height of the jump in the SQUID measurements and the results from literature the oxygen contamination can be estimated as $m_{O_2} \approx 0.1$ mg. This contamination may vary with time during one measurement and every time the sample space is vented to change the samples for different measurements. Combined with a possible paramagnetic impurity within the sample this leads to a magnetic-field-dependent splitting when comparing χ for various magnetic fields. For better visibility of the intrinsic features the curves for χ have been shifted such that their high temperature regime is field-independent.

Figure 4.6 displays the results from field cooled measurements of $\chi(T)$ for eight different magnetic fields per direction. Centered around 28 K a broad maximum is located that indicates 1D fluctuations. Consequently, it can be described reasonably well with theoretical data for a spin ½ antiferromagnetic Heisenberg chain [42, 43] that was calculated with the thermodynamic Bethe ansatz. For the comparison with measured data it has to be scaled with the coupling constant J_{1D} and the g-factor by $g^2/4$ to be adjusted for the specific material. Comparing the

	$\mathbf{E} \parallel [100], \mathbf{H} \parallel [001]$	$\mathbf{E} \parallel [001], \mathbf{H} \parallel [100]$
A	$0.725\,\mathrm{mm}^2$	$2.0\,\mathrm{mm}^2$
d	$0.3\,\mathrm{mm}$	$0.34\,\mathrm{mm}$
C_0	$2.12 \times 10^{-14}\,\mathrm{F}$	$5.21 \times 10^{-14}\,\mathrm{F}$

Table 4.2: Sample geometry for dielectric measurements.

absolute values of the peaks for the three crystallographic directions as well as the g-factors for the scaling of the theoretical data proves an anisotropic behavior between magnetic fields applied in the (001) plane and along the [001] direction.

At even lower temperatures the onset of 3D ordering is indicated by a much smaller peak. The field-dependent transition temperatures are evaluated from the maximums in the derivative of the magnetization with respect to the temperature, $\mathrm{d}M/\mathrm{d}T$, that is shown in the insets. They exhibit no significant dependence on the orientation of the crystal in the magnetic field, possibly due to the restricted temperature range of the SQUID where temperatures below 1.8 K and magnetic fields above 7 T are not accessible.

4.4 Dielectric characterization

The dielectric properties of $LiCuVO_4$ were measured for constant magnetic field as function of temperature and vice versa. For the measurements differently oriented samples where used. Their geometric dimensions and the corresponding geometric capacity are given in table 4.2.

Due to the broad range of temperatures desired and the special interest in the properties at very low temperatures two different cryostats have been used. Measurements with temperatures below 1.2 K were performed in an *Oxford Instruments "Kelvinox"* dilution refrigerator. Additional Measurements above 1.8 K were carried out in a *Quantum Design "Physical Properties Measurement System"* (PPMS).

4.4.1 $\boldsymbol{H} \parallel [001], \boldsymbol{E} \parallel [100]$

As explained in the introduction the chiral magnetic order in $LiCuVO_4$ can be suppressed with a temperature-dependent critical magnetic field H_{N2}. The critical field is expected to increase to a maximum value of $\mu_0 H_{\mathrm{N2}}(T \to 0\,\mathrm{K}) \approx 7.4\,\mathrm{T}$ with decreasing temperature as was demonstrated in [80] for temperatures above 1.5 K. Due to the instability of the magnetic structure close to the phase transition quantum fluctuations should dominate the dynamics at very low temperatures.

For the sake of simplicity this ferroelectric phase transition was first measured with magnetic field in [001] direction as to exclude any contributions from the lower lying transition at H_{N1} present for other orientations of the sample with respect to the magnetic field.

Magnetic-field-dependent polarization

To demonstrate the ferroelectric nature of $LiCuVO_4$ at low temperatures the polarization P was measured as function of the magnetic field H. The idea for this kind of measurements is similar to pyrocurrent measurements that were introduced

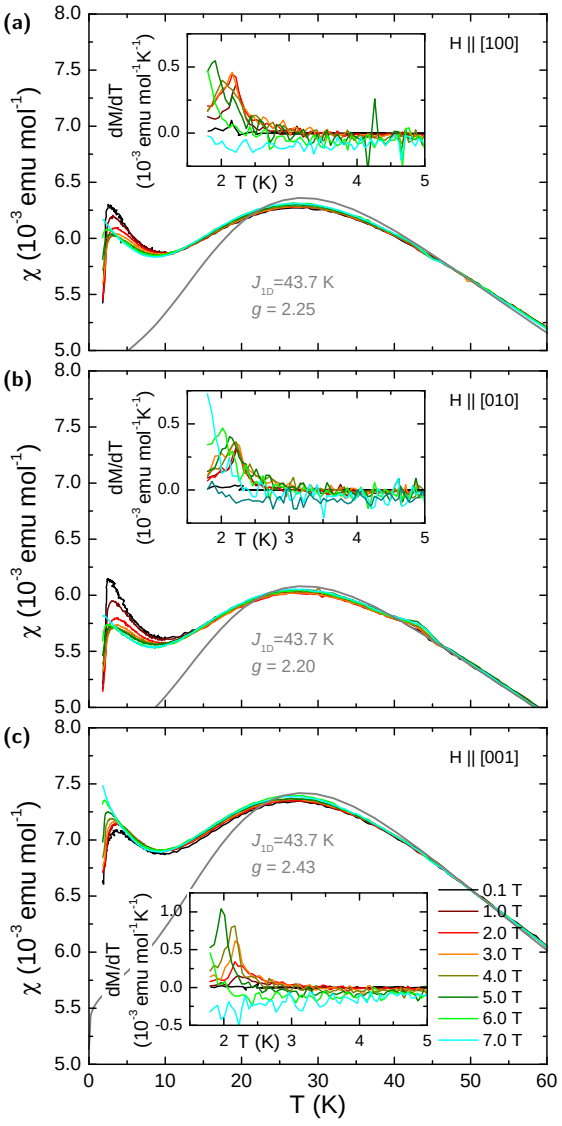

Figure 4.6: Low-temperature susceptibility data.
Temperature-dependent susceptibility χ of $LiCuVO_4$. The 1D nature of the Cu-O chains can be identified by the broad peak at 28 K. The peak positions in dM/dT (insets) indicate the transition into a 3D ordered phase at temperatures below 2.5 K. (c) shows the results for magnetic field in [001] direction, colored curves represent the measurements at magnetic field between 0.1 and 7.0 T. Theoretical results (gray ▬) for the spin $^1/_2$ antiferromagnetic Heisenberg chain from [42, 43] scaled with coupling constant J_{1D} = 43.7 K and g-factor 2.43 are a good approximation of the curves. Both J_{1D} and g are in agreement with previous results from [48]. (a) and (b) show the results for the [100] and [010] direction that are similar to the measurements in (c) but the susceptibility has a smaller absolute value. This leads to smaller values of $g_{[100]}$ = 2.25 and $g_{[010]}$ = 2.20 and demonstrates an anisotropic behavior similar but less pronounced compared to the results in [48].

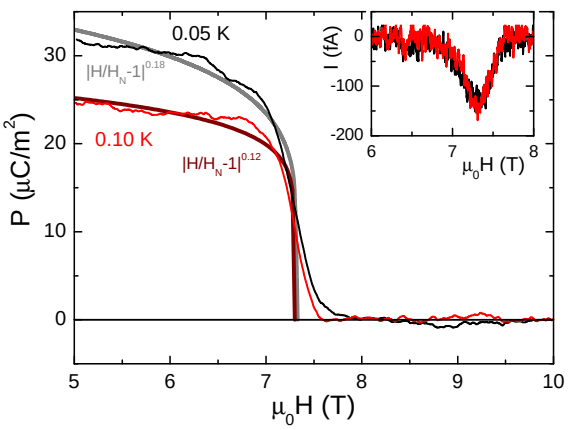

Figure 4.7:
***H* ∥ [001] - *P*(*H*) measurements at 0.05 and 0.10 K.**
At both temperatures the emergent spontaneous polarization at the critical field H_N is observed. The continuous change of the polarization close to the phase transition is an indication that the phase transition is of second order. In the inset the measured current $I \propto \mathrm{d}P/\mathrm{d}H$ is shown.

in section 2.2.2. For the $P(H)$ measurements an electric field of 667 V/mm was applied in the high-field paraelectric phase at a magnetic field of 10 T, well above the critical field. The magnetic field was then reduced with applied electric field such that the emergent spontaneous polarization at the phase transition could be fully polarized. The measurements shown in figure 4.7 were taken while raising the magnetic field towards 10 T after shutting off the electric field, $E = 0$ V/mm.

Both measurements demonstrate that $LiCuVO_4$ exhibits spontaneous polarization and that it is possible to switch it even at very low temperatures down to 0.05 K. The continuous reduction of the polarization is consistent with the second order nature of the phase transition.

Using the minimums of the measured current I shown in the inset $\mu_0 H_N$ is found as 7.30 and 7.33 T for 0.10 K and 0.05 K respectively. Also, the general form of both $P(H)$ curves can be described by $|H/H_N - 1|^\beta$ with exponents β of the order of 0.15(3) as demonstrated in the main panel of the figure. Typically, an exponent $\beta = 0.5$ is expected at a continuous phase transition when observing $P(T)$. For the example of $MnWO_4$ it has been demonstrated [64] that the exponent in the magnetic field can be reduced due to the magneto electric coupling. Consequently, it seems reasonable that the observed exponent in $LiCuVO_4$ also is smaller than 0.5.

Hysteresis curves

In figures 4.8a to 4.8c the evolution of $P(E)$ curves measured at 0.8 K can be observed. Starting at zero field in figure 4.8a the $P(E)$ curves are closing with increasing magnetic field up to 5 T. This effect is caused by an increase of the coercive field as the spin configuration of $LiCuVO_4$ is stabilized by the magnetic field and the applied electric field of $E_{max} \approx 670$ V/mm is insufficient to overcome the pinning of the polarization. When increasing the magnetic field further and approaching the phase transition the coercive field is reduced as thermal fluctuations are able to soften the pinning of the polarization. As can be seen in figure 4.8b this causes the $P(E)$ loops to open until the actual critical field $\mu_0 H_N(0.8\,\mathrm{K}) = 7.1$ T of the phase transition is reached. In the paraelectric phase above the critical field the spontaneous polarization quickly vanishes and no hysteresis remains (figure 4.8c). Both saturation polarization and coercive field have been evaluated from the hysteresis loops and are given in figure 4.8d as function of the magnetic field. In the magnetic field regime colored gray the applied field was insufficient to fully

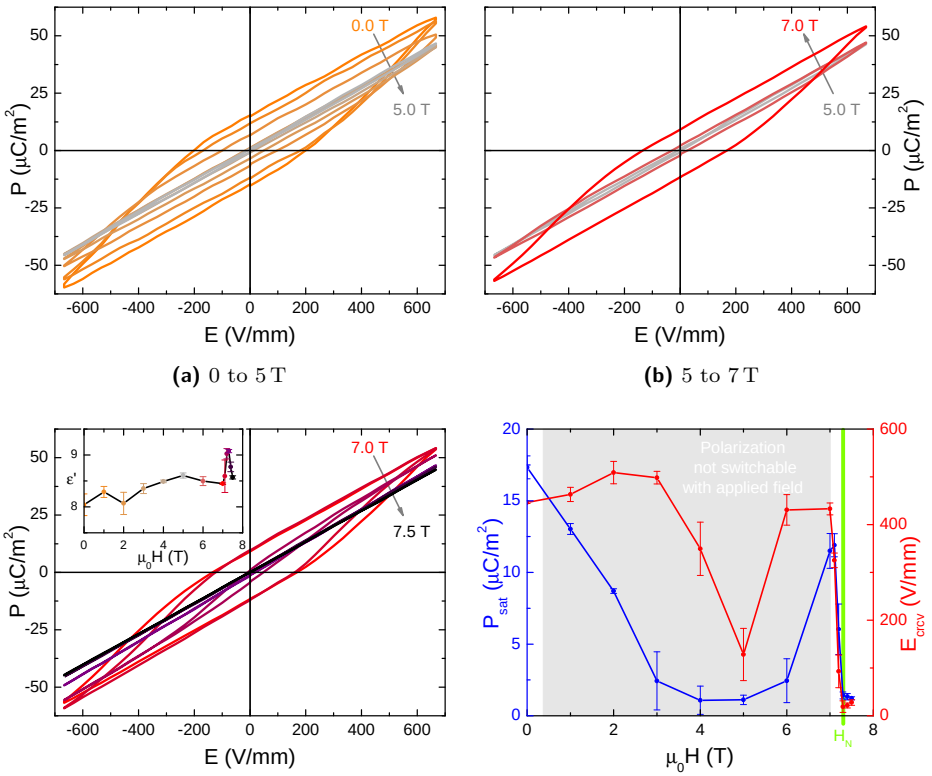

(a) 0 to 5 T **(b)** 5 to 7 T

(c) 7 to 7.5 T **(d)** H-dependent P_{sat} and E_{crcv}.

Figure 4.8: H ∥ [001] - Polarization measured at 0.8 K.
(a) - (c) demonstrate the field dependence of the polarization measured at 0.8 K. The magnetic field dependence of ε' is plotted in the inset in (c) while (d) shows P_{sat} and E_{crcv}.

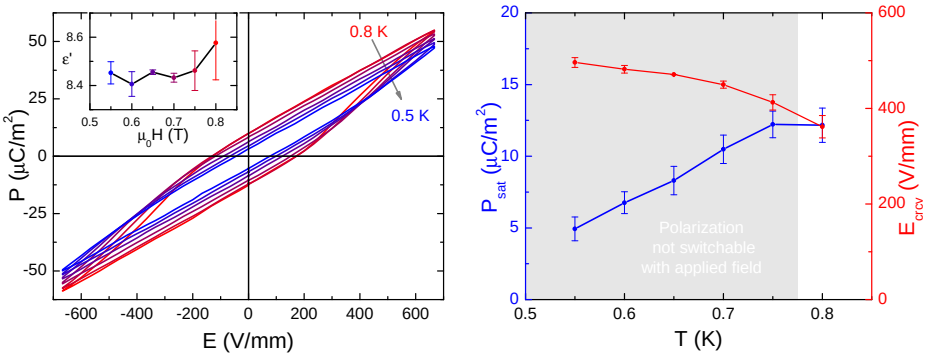

(a) $P(E)$ curves at 7.1 T

(b) T dependence of P_{sat} and E_{crcv}

Figure 4.9: H ∥ [001] - Polarization measured at 7.1 T.
Measurements at 7.1 T for temperatures between 0.5 and 0.8 K in (a) show an increase of the coercive field for lower temperatures. The inset shows the permittivity found from the slope of the linear regime of the $P(E)$ curves. In (b) both P_{sat} and E_{crcv} found from the measurements are plotted.

switch the polarization of the sample. Here the values obtained for P_{sat} and E_{crcv} are inexact but can be understood as a lower limit of the actual values and it is observed that the coercive field with magnetic field is higher than in zero magnetic field.

Additionally, the permittivity of the sample can be calculated from the slope of the linear regime in the $P(E)$ curves using

$$\varepsilon' = \frac{dP}{\varepsilon_0 dE} + 1 \tag{4.3}$$

as plotted in the inset of figure 4.8c where a maximum is observed at the phase transition.

Similar measurements were also done at a constant magnetic field of 7.1 T for different temperatures and figure 4.9a shows that the observed switchable polarization is reduced with temperature as the thermal fluctuations are reduced. This is again caused by the increasing coercive field as plotted in figure 4.9b.

Finally, a magnetic field dependent set of hysteresis curves was measured at $T = 0.1$ K. As shown in figure 4.10 the observed polarization is much smaller compared to the previous measurements.

At 0.1 K the applied electric field was not sufficient to fully switch the polarization of the sample.

Compared to the $P(H)$ measurements at the same temperature only a very small fraction (1.7 of 24 µC/m^2) of the spontaneous polarization could be switched in zero field. This indicates a much higher coercive field due to the stronger pinning of the magnetic spins at low temperatures. From the saturation polarization in figure 4.10b the increase in the coercive field with the magnetic field can still be inferred from the steep decline of P_{sat} away from magnetic zero field.

The permittivity ε' evaluated from the $P(E)$ curves in the inset of figure 4.10a shows a small feature at the critical field demonstrating that measurements of the permittivity at low temperatures are promising.

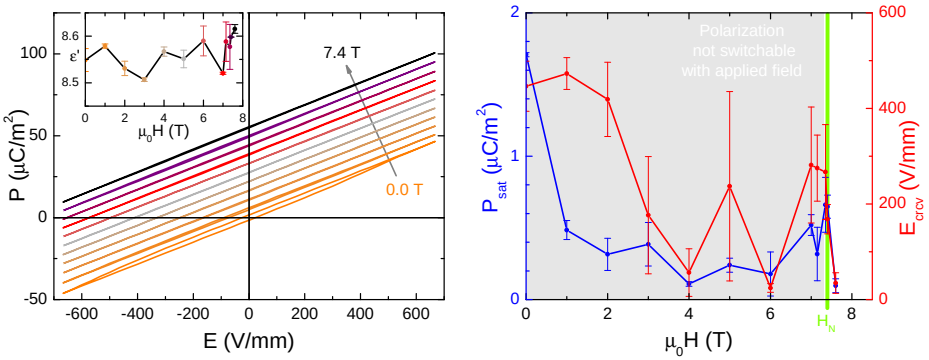

(a) $P(E)$ measurements from 0 to 7.4 T.

(b) P_{sat} and E_{crcv}

Figure 4.10: H ∥ [001] - $P(E)$ at 0.1 K.
(a) shows the results of the $P(E)$ measurements at 0.1 K with ε' in the inset. At this temperature the observed hysteresis is very small as can be seen in P_{sat} in (b). Only at the phase transition the applied electric field was sufficient to completely switch the polarization.

Low-frequency permittivity

Figure 4.11a shows the results for $\varepsilon(T)$ for nine different magnetic fields at a fixed frequency of 1 kHz.

For higher magnetic fields measurements from the dilution refrigerator are shown. The axis break covers the temperature range that can not be accessed by either instrument. Here the position of the peaks indicates the transition into the ferroelectric phase. Additionally, the temperature dependence of the height of the peaks can be observed, that is drastically reduced for lower temperatures.

The right frame, figure 4.11b displays similar results for measurements at constant temperatures. Here the measurement at 2 K was performed in the PPMS while all other measurements are from the dilution refrigerator. No significant hysteresis of the peak position between measurement with increasing or decreasing magnetic field (same color in the figure) are visible in accordance with the reported second order nature of the phase transition. Again, the reduction of the peak height with temperature is clearly visible.

4.4.2 H ∥ [100], E ∥ [001]

Using a magnetic field in [100] direction $LiCuVO_4$ undergoes an additional phase transition. Here the polarization is shifted from the [100] to the [001] direction when applying a sufficiently strong magnetic field $H > H_{\mathrm{N1}}$. To observe the switching of the polarization axis the electric field was applied perpendicular to the magnetic field along the [001] axis of the crystal. At magnetic fields above H_{N2} the polarization will be suppressed.

Polarization & sample orientation

All measured hysteresis curves in this orientation show less polarization compared to the previous direction (**H** ∥ [001], **E** ∥ [100]). As a consequence the linear contribution in $P(E)$ dominates and has to be subtracted to clearly see the switched

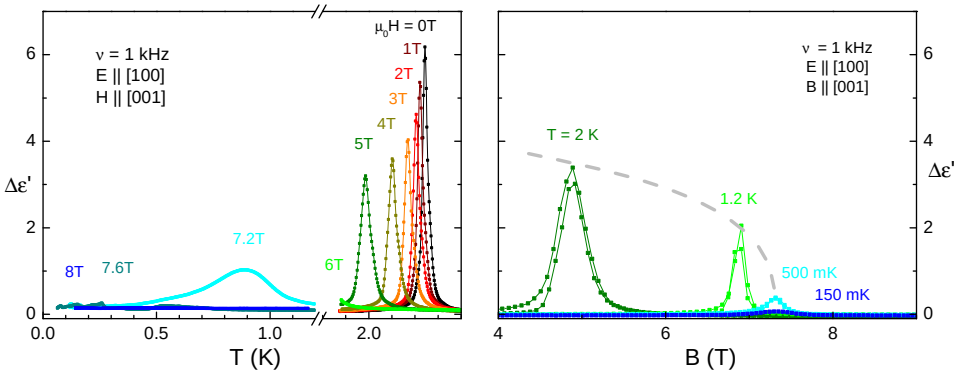

(a) Temperature-dependent measurements. **(b)** Magnetic-field-dependent measurements.

Figure 4.11: H ∥ [001] - 1 kHz permittivity.
The temperature- (a) and magnetic-field-dependent (b) measurements on $LiCuVO_4$ show the phase transition into the paraelectric phase. The height of the peaks is continuously reduced with temperature as expected at a second order phase transition resembling the $P(H)$ results in figure 4.7.

polarization and to evaluate the coercive field. For all measurements presented in the following the average permittivity $\varepsilon' = 8.388(1)$ from $P(E)$ curves measured in zero field (see the inset in figure 4.12a) was used when subtracting the linear contribution. As can be seen the zero-field permittivity is independent of temperature.

The zero field $P(E)$ curves in the main panel of the figure already demonstrate a deviation from the expectation; for a perfectly oriented sample the zero field measurements should not find any switchable polarization.

At 0.8 K the misaligned sample shows a saturation polarization of $P_{\mathrm{sat},\mathbf{E}\|[001]} = 0.75\,\mu\mathrm{C/m^2}$. Comparing this value to the results from the previous measurements, $P_{\mathrm{sat},\mathbf{E}\|[100]} = 15.0\,\mu\mathrm{C/m^2}$ (figure 4.8 on page 61), gives an estimate of 5 % for the addition from the misalignment. An additional contribution of this magnitude would be caused by a 3° misalignment. To confirm the magnitude of the sample misalignment a Laue picture of the crystal mounted on the sample holder, figure 4.12b, was taken. Here the misalignment of the sample is obvious merely from the offset of the reflex structure from the center of the picture. Closer analysis of the position of the reflexes reveals the deviation of the magnetic field from the intended [100] direction as 7.2(2)°. This tilting of the sample not only influences the orientation within the magnetic field but also the direction of the applied electric field. In this case the electric field is tilted by 3.2(2)° in [100] direction in good agreement with the estimate from the zero field polarization. Due to the small sample size and its form it was not possible to reduce the misalignment.

For this orientation of magnetic and electric fields measurements of $P(E)$ curves were done at 1.2 K and 0.8 K for various magnetic fields that will be discussed in the following.

1.2 K

To enhance the visibility of the evolution of the polarization with the magnetic field the $P(E)$ measurements presented in figure 4.13 are split into three field

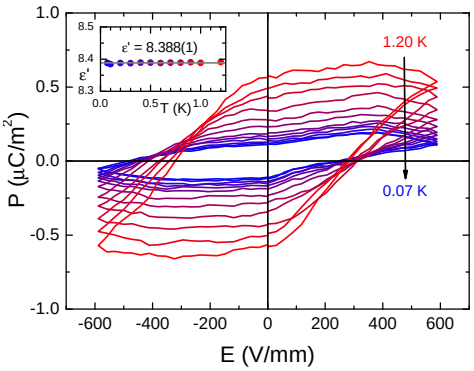

(a) $P(E)$ measurements in zero field.

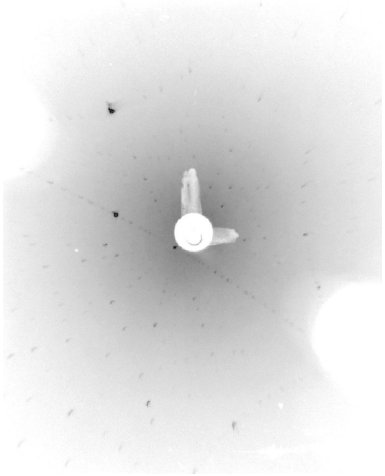

(b) Laue picture of the $LiCuVO_4$ sample.

Figure 4.12: H ∥ [100] - sample misalignment.
$P(E)$ measurements in zero field are shown in (a). The inset shows the slope of the raw data that was subtracted from the data in the main figure and all other $P(E)$ curves shown for electric field parallel [001]. The existance of measurable polarization in this sample orientation indicates the misalignment of the sample. (b) shows the Laue picture of the $LiCuVO_4$ sample mounted on the sample holder. The central reflex is assigned to the [100] direction and its deviation from the center of the picture denotes the misalignment of the sample with respect to the magnetic (and electric) field.

regimes. Figure 4.13a shows the curves for $0 < \mu_0 H \leq 3.4\,\mathrm{T}$ where the change of the hysteresis loops at H_{N1} is documented. As discussed before the measurements below H_{N1} show a finite polarization due to the misalignment of the sample. The increased canting of the curves indicates an increase of the permittivity close to the phase transition compared to the zero field value used for the background subtraction. Panel 4.13b shows the $P(E)$ measurements in the ferroelectric phase where the polarization is switchable with the applied electric field is small in the center of the phase at about 5 T. Finally, in 4.13c the measurements over H_{N2} show the vanishing polarization in the paraelectric phase.

To analyze this further the key features of the curves, permittivity ε', saturation polarization P_{sat}, and coercive field E_{crcv}, are summarized in figure 4.13d.

The maximum positions of the peaks in the permittivity indicate the critical fields. Away from the phase transitions $\varepsilon'(H)$ is found to be almost independent of the field. In this plot the color of each point of the $\varepsilon'(H)$ curve corresponds to that of the hysteresis loop from which it was evaluated.

The coercive field on the other hand is reduced from its zero field value below the first critical field before it starts to increase again in the ferroelectric phase. For approximately 3.5 T to 6.5 T the coercive field is observed to be constant. This behavior is caused by the experimental limitation of the applied voltage that was not sufficient to overcome the coercive field and switch any polarization in this regime. Therefore, all values obtained in this field region do not represent the actual intrinsic properties of the sample but can only be seen as lower limits.

Due to the misalignment of the sample the observed polarization starts at a finite value of $\approx 0.5\,\mu\mathrm{C/m^2}$. In the ferroelectric phase this value increases up $3.4\,\mu\mathrm{C/m^2}$ at 3.3 T. The high coercive fields further away from the critical field prohibit finding additional reliable values of the saturation polarization in this phase. Above H_{N2} the polarization vanishes as expected.

0.8 K

Similar measurement were also done at 0.8 K. As the $P(E)$ curves are almost identical to those measured at 1.2 K in both their form and evolution close to the critical fields a plot of them was omitted in the main text. Instead they are shown in figure C.1 in the appendix on page 123. There the curves are again plotted after subtracting the same linear contribution as discussed for the measurements at 1.2 K.

Figure 4.14 displays the results from the evaluation of the hysteresis curves. The results are similar to the measurements at higher temperature but the observed saturation polarization close to the phase transitions is smaller by almost a factor of two. Also the field regime of insufficient applied electric field is broader and the increase of the coercive field at the edges of the ferroelectric phase is steeper.

Comparing the saturation polarization with the measurements at the same temperature but different orientation of magnetic and electric field shows that the saturation polarization for $\mathbf{E} \parallel [001]$ is smaller than the observed saturation polarization for $\mathbf{E} \parallel [100]$ at the same magnetic field strength.

Due to the reduced amount of switchable polarization in this electric field direction direct measurements of the polarization at lower temperatures did not yield useful results.

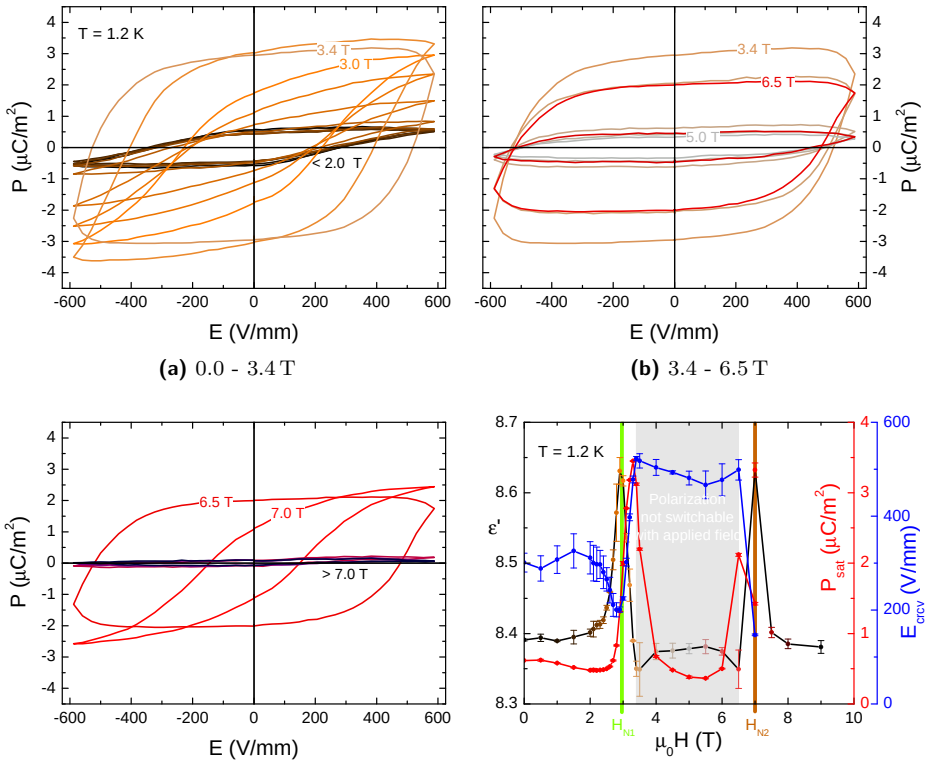

(a) 0.0 - 3.4 T **(b)** 3.4 - 6.5 T

(c) $\mu_0 H \geq 6.5\,\mathrm{T}$ **(d)** ε' , P_{sat}, and E_{crcv}

Figure 4.13: $\boldsymbol{H}$ ∥ [100] - $\boldsymbol{P(E)}$ at 1.2 K.
(a) - (c) show measurements of the $P(E)$ curves of $LiCuVO_4$ at 1.2 K. Both phase transitions can be seen in the opening of the hysteresis loops as the coercive field is reduced in the proximity of the phase transition and more polarization can be switched with the applied electric field. (d) shows the results from the evaluation of the hysteresis loops. The peak positions in the permittivity ε' indicate the critical fields and the color of each point corresponds to the hysteresis loop that was evaluated. Only close to the phase transitions the applied electric field was high enough to overcome E_{crcv} and completely switch the polarization. The field range where this is not true is shaded gray and there the values found for of P_{sat} and E_{crcv} are only lower limits of the actual values.

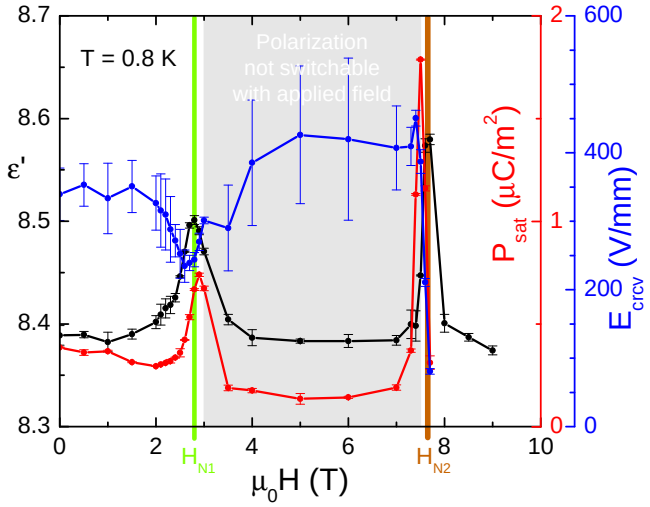

Figure 4.14: $H \parallel [100]$: P_{sat}, ε' , and E_{crcv} at 0.8 K.
Evaluation results of the $P(E)$ curves measured at 0.8 K as function of the magnetic field. The peak positions in the permittivity ε' (black •) indicate both phase transitions. Looking at the coercive field (blue •) shows that the results are only valid close to the phase transitions as the applied electric field is not strong enough to switch the polarization away from the phase transitions. The area affected by this is shaded gray in the plot. In red (•) the saturation polarization is observed to increase at H_{N1} and decease at H_{N2}.

4.5 Phase diagrams

From the measurements of magnetization, polarization, and permittivity the phase diagrams for both magnetic field directions observed have been compiled.

$H \parallel [001], E \parallel [100]$

The result of combining all previously shown measurements into a phase diagram of $LiCuVO_4$ for magnetic field in [001] direction has been plotted in figure 4.15a. The transition temperatures of magnetic and dielectric measurements are in very good agreement both with each other as well as the known transition temperatures, $T_N = 2.3\,K$ without external magnetic field, and critical fields, $\mu_0 H_N = 7.4\,T$ at $T \to 0\,K$, from literature.

$H \parallel [100], E \parallel [001]$

The phase diagram for $LiCuVO_4$ in [100] magnetic field is shown in figure 4.15b. For comparison the phase boundary for $\mathbf{H} \parallel [001]$ is shown again as a gray (▬) line. The transition temperatures from the magnetization measurements are almost identical to those obtained previously, deviations in the phase diagrams are only observed at lower temperatures.

Here increasing the magnetic field tilts the polarization from the [100] to the [001] direction at $\mu_0 H_{N1} \approx 2.8\,T$. Even higher magnetic fields suppress the ferroelectric order at $\mu_0 H_{N2} \approx 8\,T$. Comparing the critical field to the results for $\mathbf{H} \parallel [001]$ shows that here H_{N2} is higher by 8 %. The deviation due to the misalignment of the

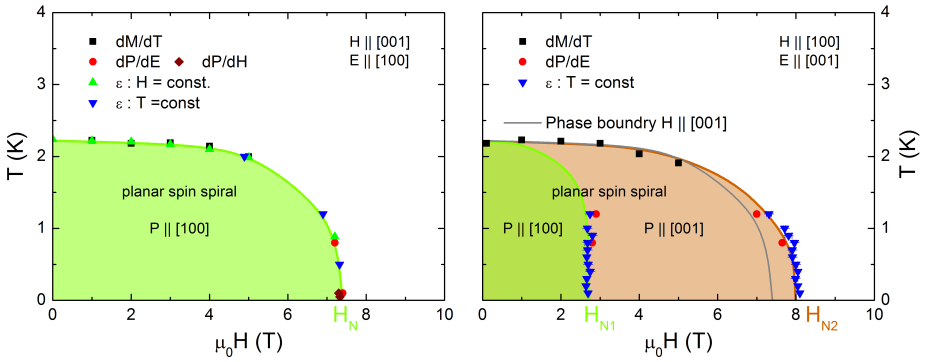

(a) $\mathbf{H} \parallel [001]$ **(b)** $\mathbf{H} \parallel [100]$

Figure 4.15: Phase diagrams of $LiCuVO_4$.
Combining the results of the magnetic (χ) and dielectric measurements ($P(E)$ and $\underline{\varepsilon}$) the phase diagrams for $LiCuVO_4$ in (a) [001] and (b) [100] magnetic field have been created.

sample is expected to be smaller by one order of magnitude, as $\cos(0°)/\cos(7.2°) \approx 1/0.992 = 0.8\,\%$.

4.6 Fluctuation dynamics

After the discussion of the phase diagrams the following section focuses on the evaluation of the fluctuation dynamics in the paraelectric phase. Again the discussion will start with the results for $\mathbf{H} \parallel [001]$, for the second orientation the results are presented from page 75.

4.6.1 $\boldsymbol{H} \parallel [001], \boldsymbol{E} \parallel [100]$

Temperature-dependent measurements

Frequency-dependent data at the phase transition are shown in figure 4.16. Both frames clearly show the asymmetry of the peaks that complicates the evaluation of the dynamical exponents.

Using the intersections of $\varepsilon''(T)$ curves of different frequencies we find $T_\mathrm{p}(\nu)$ that can be evaluated with two different models. Typically, the relaxation time is connected with the correlation length ξ via the dynamical exponent z, $\tau \propto \xi^z$. At the phase transition the correlation length is assumed to diverge as a function of temperature, $\xi \propto [T - T_\mathrm{N}]^{-\nu_\xi}$ with the correlation length exponent $\nu_\xi > 0$. This leads to

$$\frac{1}{\tau} = 2\pi\nu \propto \left[\frac{T - T_\mathrm{N}}{T_\mathrm{N}}\right]^{z\nu_\xi}$$

where the dynamical exponent z is usually positive indicating critical slowing down of the dynamics. From the data the critical exponent $\gamma = z\nu_\xi$ is found as 4.8(17) with fixed $T_\mathrm{N} = 0.82\,\mathrm{K}$.

For gapped chiral phases it has been discussed [24] that the phase transition is of Berenitzkii-Kosterlitz-Thouless type. This type of phase transition is characterized by a different scaling behavior of the correlation length at the phase transition,

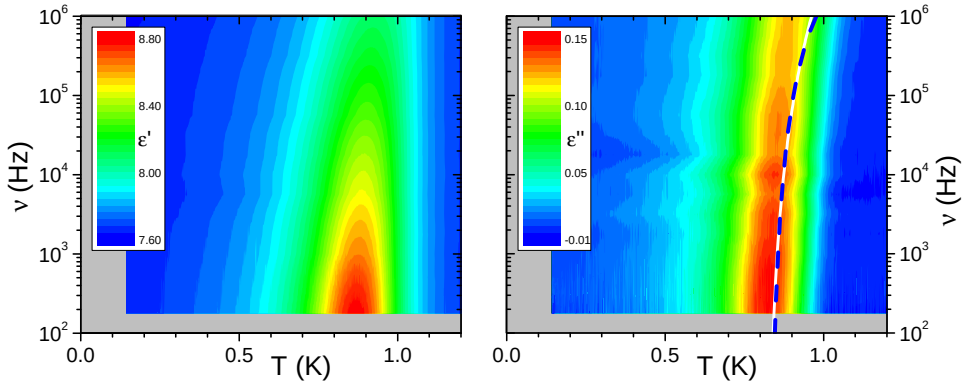

(a) permittivity **(b)** dielectric loss

Figure 4.16: $H \parallel [001]$ - complex permittivity at 7.2 T.
Permittivity (a) and dielectric loss (b) as function of T and ν at a fixed magnetic field of $\mu_0 H = 7.2\,\mathrm{T}$. Close to the phase transition at 0.85 K the divergence of ξ can be seen in the slope of the peak position in ε'' . The lines in (b) are fits of the frequency-dependent peak position to evaluate the dynamical exponents with critical exponents (white) and BKT scaling (blue ▬).

namely $\xi \propto \exp(1/\sqrt{(T-T_\mathrm{N})/T_0})$. With the same connection between ξ and τ as before the scaling results in

$$\frac{1}{\tau} = 2\pi\nu \propto \frac{1}{\left(\exp(\sqrt{\frac{T_0}{T-T_\mathrm{N}}})\right)^z} = \exp\left(-z\sqrt{\frac{T_0}{T-T_\mathrm{N}}}\right) \tag{4.4}$$
$$= 1 - z\left(\frac{T_0}{T-T_\mathrm{N}}\right)^{1/2} + \frac{z^2}{2}\frac{T_0}{T-T_\mathrm{N}} - \frac{z^3}{6}\left(\frac{T_0}{T-T_\mathrm{N}}\right)^{3/2} + \ldots$$

Here the fit yields a result of $z\sqrt{T_0} = 2.6(10)$.

In figure 4.16b the results from the fits are shown. Both show a clear deviation from the measured peak position but no significant difference in their quality is observed. Thus from the dielectric measurements the possible Berenitzkii-Kosterlitz-Thouless nature of the transition could neither be confirmed nor denied.

Magnetic-field-dependent measurement

For the main analysis of the dynamics at the phase transition in $LiCuVO_4$ magnetic-field-dependent measurements in a frequency range from 30 MHz to 5.6 GHz were performed at constant low temperatures down to 0.025 K. The frequencies were chosen as four frequencies per decade with logarithmic spacing. To achieve complete coverage of this frequency range two network analyzers have been used, a *Rhode & Schwarz "ZVB4"* and an *Agilent "PNA-X"*.

The transition from the ferroelectric to the paraelectric phase can be seen in both the real part ε' (figure 4.17) and the imaginary part ε'' (figure 4.18) of the permittivity. To demonstrate the quality and reproducibility of the results the measurements at 1 GHz, green (▬) in both figures, are plotted from findings of both instruments for all temperatures. For improved visibility of the dynamics at

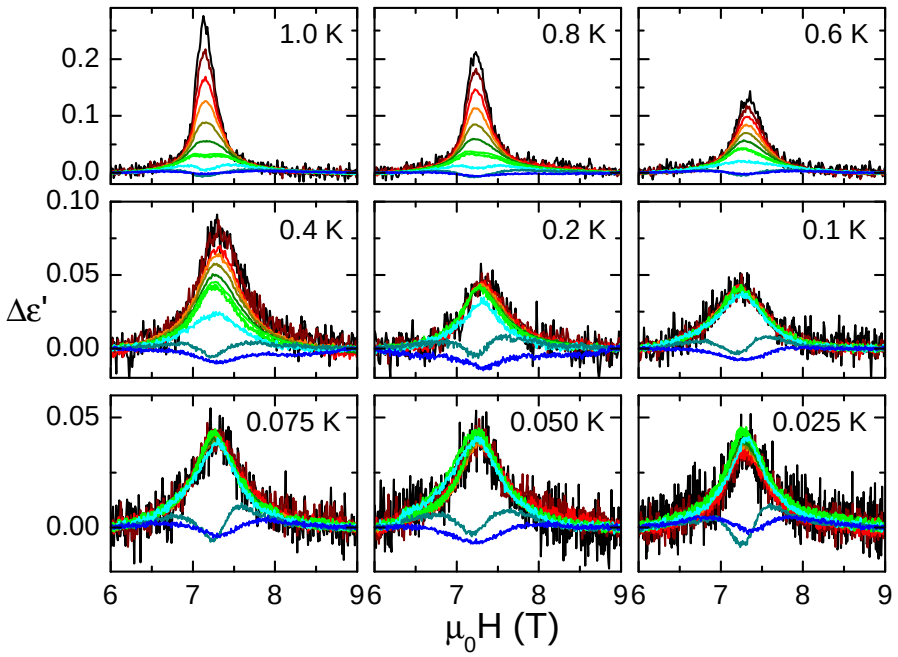

Figure 4.17: $H \parallel [001]$ - high-frequency permittivity data.
$\Delta\varepsilon'$ of $LiCuVO_4$ as function of the magnetic field in [001] direction at constant temperatures. The measured frequencies span a range from 31.6 MHz (black ▬) to 5.62 GHz (blue ▬) with four frequencies per decade in logarithmic spacing. In the top left panel the succession from low to high frequencies can be seen in the dispersive peak at the critical field. For comparison of the results of both instruments used the green (▬) curve at 1 GHz is shown twice at all temperatures.

the phase transition a frequency dependent linear offset was subtracted such that all curves coincide in the paraelectric phase.

Starting with the real part of the permittivity in figure 4.17 at 1 K in the top left panel the phase transition is located at 7.15 T and shows a dispersion throughout the whole frequency spectrum. At 1.87 GHz the 'dispersion' minimum expected for critical slowing down in classical ferroelectric materials [61, 30, 60] is observed. Reducing the temperature also reduces the absolute height of the feature as it moves with the temperature-dependent critical field towards 7.38 T while shifting the minimum in ε' towards higher frequencies, at 0.4 K it has moved up to 3.16 GHz.

Below 0.4 K the dispersion observed at higher temperatures is lifted for frequencies below 1 GHz resulting in a frequency-independent peak at the phase transition with a sharp drop above 1 GHz.

The measurements of the dielectric loss in figure 4.18 show similar results. Starting again at 1 K in the upper left frame ε'' also shows a dispersive peak at the critical field H_N. When reducing the temperature the height of the peaks is reduced and starting at 0.4 K frequencies below 500 MHz show no contribution at the phase transition, $\Delta\varepsilon''(\nu \lesssim 500\,\text{MHz}) \approx 0$. This is in agreement with the vanishing dispersion in $\Delta\varepsilon'$.

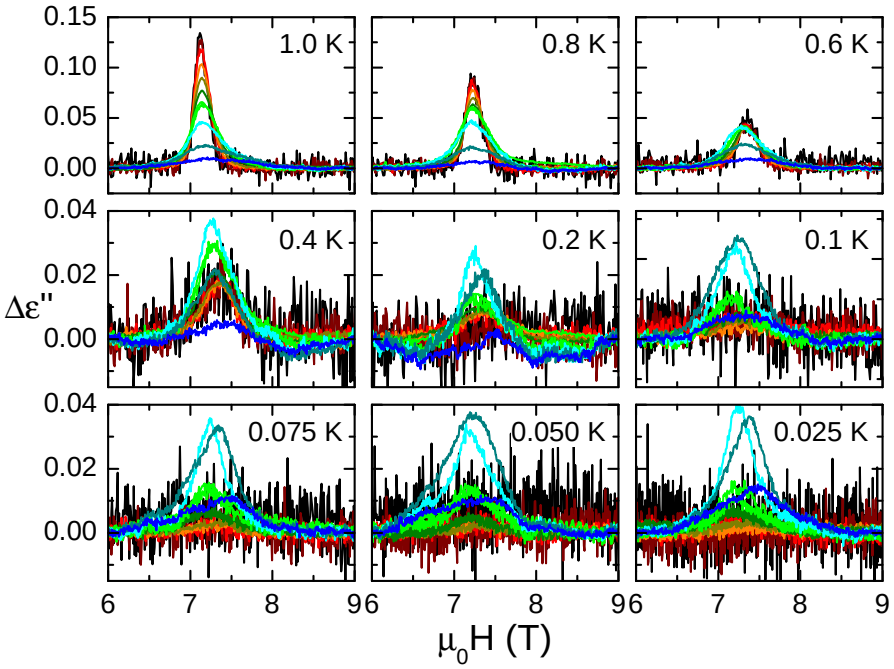

Figure 4.18: $\boldsymbol{H}$ ∥ [001] - high-frequency dielectric loss.
The imaginary part of the complex permittivity of $LiCuVO_4$ as a function of magnetic field in [001] direction at constant temperatures with the same color coding as explained in figure 4.17. Again the 1 GHz curves (green —) are always plotted twice from different instruments, the barely visible deviations confirming the good agreement and reproducibility of the results. The peak positions and the intersections of neighboring frequencies above the critical field are used for the evaluation of the fluctuation dynamics.

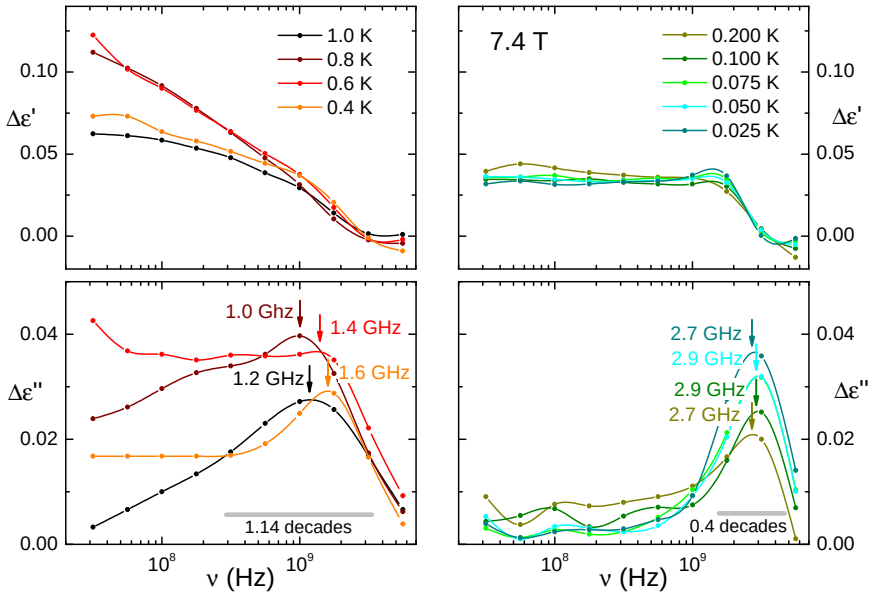

(a) 1.000 - 0.400 K **(b)** 0.200 - 0.025 K

Figure 4.19: $H \parallel [001]$ - permittivity spectra at 7.4 T.
The measured spectra for $LiCuVO_4$ at 7.4 T show relaxational character above 0.4 K in (a) that changes to an excitational character for lower temperatures in (b).

At higher frequencies the phase transition is visible as peak whose height increases up to 2 GHz before it starts to vanish. Similar to the results of the permittivity, lowering the temperature below 0.2 K does not change the behavior significantly.

Fluctuation dynamics in the paraelectric phase

Finding the relaxation time τ from measurements of the dielectric loss can be done with different approaches. The simplest method is to evaluate the peak position in $\varepsilon''(\log_{10}(\nu))$ spectra measured at constant magnetic field of 7.4 T and temperature as shown in figure 4.19. The spectrum measured at 1 K differs from the measurements at slightly lower temperatures. This can be understood by looking at the phase diagram in figure 4.15a on page 69 where the magnetic field of 7.4 T is further away from $\mu_0 H_N(T)$ at 1 K than for the measurements at lower temperatures.

If the number of frequencies measured is limited another approach is to calculate the relaxation time from the intersections of $\varepsilon''(\mu_0 H_i)$ curves measured at different frequencies. Assuming the peak in the frequency domain to be symmetric and knowing two frequencies ν_1 and ν_2 with equal dielectric loss the peak in between can be found as their average:

$$\log_{10}(\nu_p(\mu_0 H_i)) = \frac{\log_{10}(\nu_1) + \log_{10}(\nu_2)}{2} \tag{4.5}$$

In both cases the frequency ν_p is associated with the relaxation time τ by $\tau =$

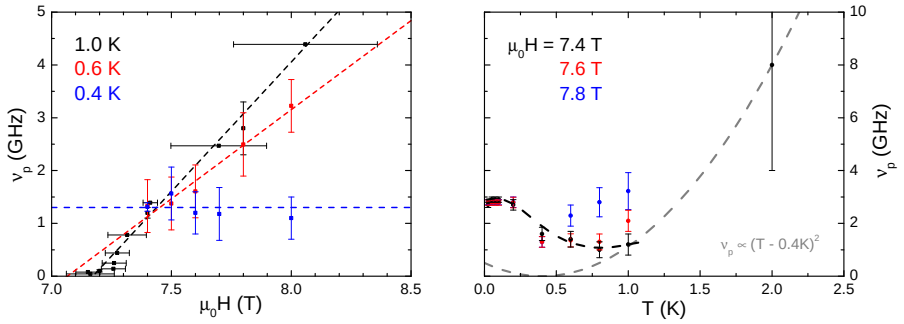

(a) Magnetic field dependence of ν_p for different temperatures.

(b) Temperature dependence of $\nu_\mathrm{p}(7.4\,\mathrm{T})$.

Figure 4.20: $\boldsymbol{H}$ ∥ [001] - GHz dynamics.
(a) For temperatures above 0.4 K the field dependence of ν_p is roughly in agreement with the Curie-Weiss law from equation (4.6). Due to the data quality the dashed lines are only a guide to the eye where $z\nu_\xi = 1$ was assumed. At lower temperatures $\nu_\mathrm{p}(\mu_0 H) \approx 1.3\,\mathrm{GHz}$ is independent of the magnetic field. (b) shows the temperature dependence of ν_p at magnetic field of 7.4 to 7.6 T. Here the dashed gray (▬) line gives an approximation of the expected temperature dependence using $z\nu_\xi = 2$. The black line marks the observed deviation from this behavior.

$1/2\pi\nu_\mathrm{p}$.

For the dielectric measurements shown in figure 4.18 both methods were used to find the peak frequency and the results are plotted in figure 4.20a for selected temperatures.

Analogue to classical ferroelectric phase transitions where the temperature T is the control parameter a multiferroic ferroelectric phase transition with the magnetic field as control parameter also shows similar dynamics above the transition and the field dependency of τ can also be described with a Curie-Weiss law, that has to be expressed as

$$\frac{1}{2\pi\tau} = \nu_\mathrm{p} = a \cdot \left[\frac{H - H_\mathrm{N}}{H_\mathrm{N}}\right]^{z\nu_\xi} \tag{4.6}$$

because of the different control parameter used to drive the phase transition. Looking at the results for different temperatures shown in figure 4.20a reveals that the description with equation (4.6) is valid only for temperatures above 0.4 K. Here the positive critical exponent is consistent with critical slowing down as expected at a ferroelectric phase transition.

At 0.4 K and below $\nu_\mathrm{p}(\mu_0 H)$ becomes independent of the magnetic field but shifts from $\nu_\mathrm{p} \approx 1.3\,\mathrm{GHz}$ at 0.4 K towards higher frequencies until it stays at 3 GHz below 0.2 K.

Figure 4.20b shows the temperature dependence of the peak position exemplary for magnetic fields of 7.4 to 7.8 T where the distinct deviation from the expected critical dynamics (gray dotted line) at low temperatures is evident.

A better understanding of the change in the dynamics below 0.4 K can be gained when returning to the spectra shown in figure 4.19 and observing not only the peak positions but also the shape of the curves for different temperatures.

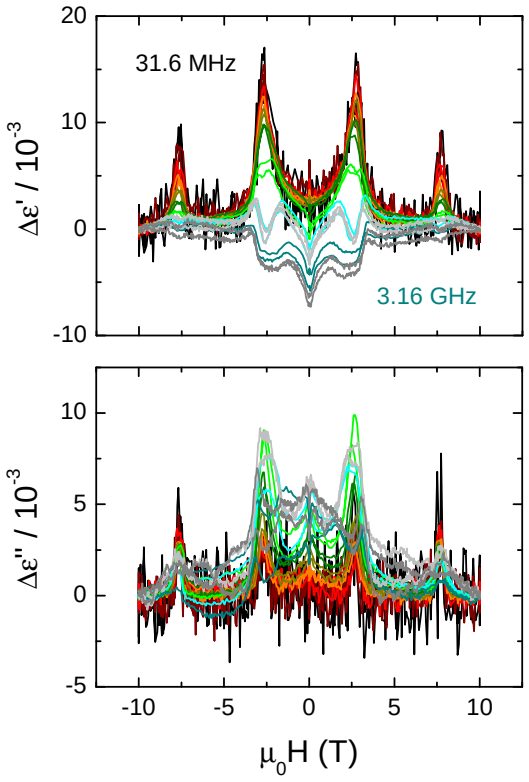

Figure 4.21:
H **‖ [100] - high frequency dynamics at 1.0 K.**
The complex permittivity of $LiCuVO_4$ as a function of the magnetic field at $T = 1\,\mathrm{K}$. In this field direction two phase transitions can be observed, at $\mu_0 H_{\mathrm{N1}} = 2.7\,\mathrm{T}$ the cycloidal spin order is flipped and the polarization is turned into the [001] direction. At $\mu_0 H_{\mathrm{N2}} \approx 7.4\,\mathrm{T}$ the magnetic field forces the spins into a collinear alignment and destroys the polarization.

Above 0.4 K the width of the peak in the dielectric loss, the lower frame of figure 4.19, is broader than 1.14 decades what is indicative of relaxational, Debye like, processes. At lower temperatures the width of the peak is strongly reduced and the reduction of temperature transfers spectral weight from the frequencies below 1 GHz to the peak that has its maximum at 3 GHz at 0.2 K and below. This change in form means that at low temperatures $LiCuVO_4$ has a very low lying excitation with an energy gap of roughly 12.4 µeV.

4.6.2 $\boldsymbol{H} \parallel [100], \boldsymbol{E} \parallel [001]$

With **H** ‖ [100] both phase transitions are visible as frequency-dependent peaks in the dielectric measurements exemplary shown for a temperature of 1 K in figure 4.21 for frequencies from 31.6 MHz to 3.16 GHz. Here a time-dependent linear drift has been corrected that is slightly different for each frequency.

The critical fields at this temperature can be found from the peak positions in ε'' of the lower frequencies as $\mu_0 H_{\mathrm{N1}} = 2.7\,\mathrm{T}$ and $\mu_0 H_{\mathrm{N2}} \approx 7.4\,\mathrm{T}$. Compared to the measurements with magnetic field in [001] direction the absolute value of the measured peaks is one order of magnitude smaller. Both phase transitions show dispersive behavior with a 'dispersion' minimum at 1.78 GHz consistent with critical slowing down.

At higher frequencies the peak at $\mu_0 H_{\mathrm{N1}}$ first turns into a much smaller double peak structure at 1.78 GHz before the field region below this critical field completely changes its shape at 3.16 GHz. In gray measurements at the same frequencies using a different measurement device are plotted that demonstrate the reproducibility of the experiment. The hysteresis like offset observed between the

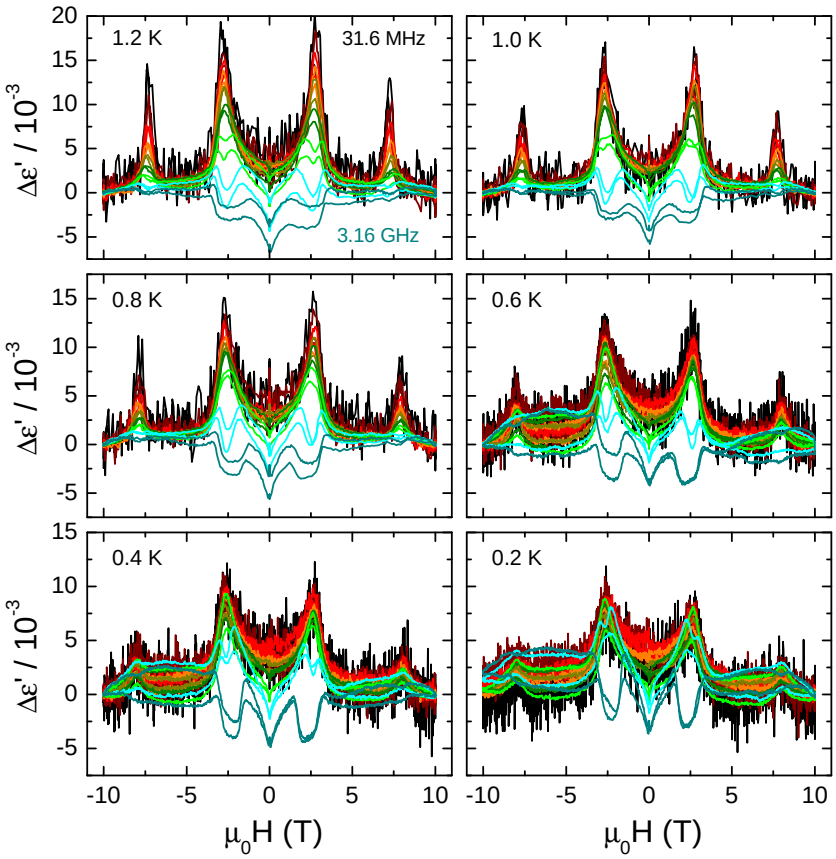

Figure 4.22: $\boldsymbol{H}$ ∥ [100] - Field dependent permittivity.
In the magnetic field dependent permittivity the phase transitions at H_{N1} and H_{N2} are observed. With decreasing temperature the height of the features is reduced but the phase transitions can be distinguished down to 0.2 K. Above 0.4 K the dynamics always show critical slowing down and the ferroelectric 'dispersion' minimum is observed.

up and down sweeps cannot be attributed to intrinsic effects of the sample as the applied linear correction of the time-dependent background is only an approximation of the real drift behavior. As the drift can be understood as a time-dependent change of the resistivity of the cables used in the measurement it causes a change in the electrical length of the probe and has a strong frequency dependence. Especially the dielectric loss is influenced strongly due to the relatively small loss angle. Therefore, $\Delta\varepsilon''$ can only be considered reliable when looking at limited parts of the measurements.

Figure 4.22 shows the temperature dependence of the permittivity from 1.2 to 0.2 K. The phase transition at the critical field H_{N1} is dispersive and the 'dispersion' minimum is observed between 1.0 (green —) and 1.78 GHz (cyan —) at 1.2 K. A reduction of the temperature shifts the minimum towards higher frequencies, at 0.8 K and below it is only visible in the 1.78 GHz curve.

Within the ferroelectric phase the dispersion is, at higher temperatures, almost lifted. Below 0.8 K some anisotropy with respect to the direction of the applied

magnetic field can be observed that is strongest in high frequencies that could be caused by the misalignment of the sample.

A detailed plot of the dynamics at H_{N2} is shown in figures 4.23a and 4.23b for ε' and ε'' respectively, where the the linear background has been determined only within the plotted magnetic field range. Here the dynamics are similar to the observation with $\mathbf{E} \parallel [100]$, however, the signal strength is smaller by a factor of approximately 25 when comparing the peak height at 1 K. The dispersive behavior at the phase transition is reduced with temperature and vanishes below 0.4 K. This can be seen best in the dielectric loss where the transition is invisible for frequencies below 100 MHz and the observed peak in the frequency domain has its maximum at about 2 to 3 GHz.

Due to the very small signal at low temperatures measurements at temperatures below 0.2 K did not yield meaningful results.

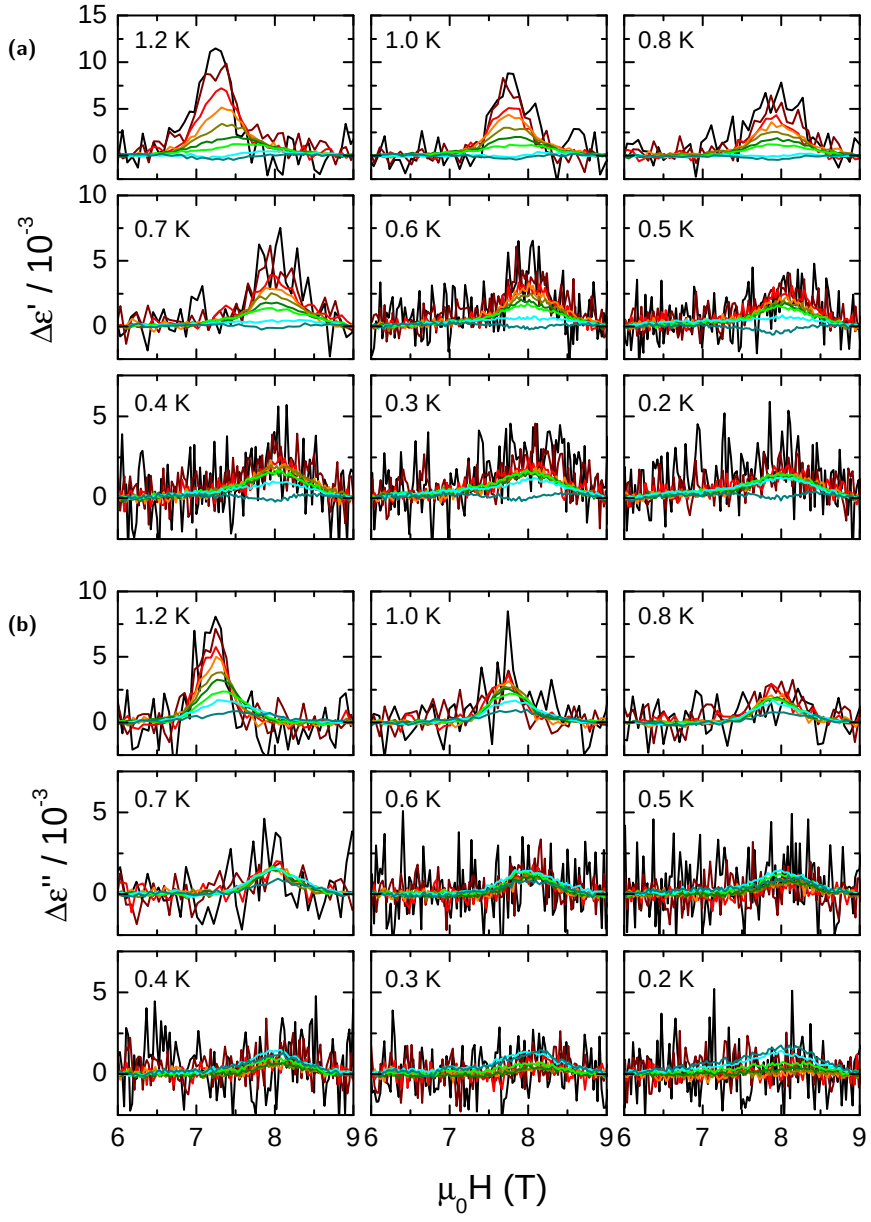

Figure 4.23: H ∥ [100] - ε' at H_{N2}.
In (a) the measurements of ε' show the critical slowing down at H_{N2} for frequencies from 31.6 MHz in black (—) to 3.16 GHz in blue (—). Despite the smallness of the feature the phase transition can be resolved down to 0.2 K and the change in the dynamics described for **H** ∥ [001] can also be seen, especially in ε'' in (b). Here the peak at the phase transition vanishes for frequencies below 100 MHz and temperatures below 0.4 K.

4.7 Conclusion

In this work the anisotropic magnetization of $LiCuVO_4$ was demonstrated with measurements of the magnetic susceptibility that also showed that strong 1D fluctuations are present in this system. From measurements of the polarization as function of both the magnetic, $P(H)$, and the electric field, $P(E)$, the magnetoelectric nature of the compound was demonstrated. Combining these results with low frequency permittivity measurements the phase diagram for two orientations of the sample with respect to magnetic and electric field could be reproduced down to temperatures of $\approx 0.025\,\mathrm{K}$.

Using permittivity measurements up to 5 GHz the fluctuation dynamics at the transition from the ferroelectric to the paraelectric phase was observed. At temperatures above 0.4 K Debye-like relaxation processes were observed that are characterized by critical slowing down typical for ferroelectric phase transitions. In the case of $LiCuVO_4$ the softening mode belongs to an electromagnon as is evident from the observation of the evolution of fluctuation dynamics with both temperature and magnetic field. This observation is similar to the results presented for $TbMnO_3$ and other magnetoelectric materials that were discussed in literature, *e.g.* $MnWO_4$.

Below 0.4 K the nature of the observed processes changes. Here the width of the observed relaxation is smaller than 1.14 decades of frequency, indicating that the damping is greatly reduced. This signifies that that the nature of the observed process changes into an excitation with a very small energy gap of only 12.4 µeV.

The observation of a low energy excitation in $LiCuVO_4$ is in good agreement with the predictions of Furukawa et al. [25] who propose the existence of a nearly gapless dielectric response from chiral solitons and in this work first experimental evidence for its existence was presented.

5 $Dy_2Ti_2O_7$

In the following chapter it will be demonstrated that the magnetic monopole-like excitations of the spin-ice compound $Dy_2Ti_2O_7$ also possess an electric dipole moment. This allows to investigate the dynamical properties of the magnetic monopoles via dielectric spectroscopy for low temperatures and high magnetic fields. The latter was applied in [111] direction where the compounds phase diagram is analogue to that of water. Of special interest is the critical endpoint at approximately 0.36 K and 1 T where the dielectric measurements show critical speeding up. Additionally, the quantum paraelectric properties caused by Ti^{4+} confined within O^{2-} octahedrons are demonstrated with measurements up to 300 K.

Contents

5.1 Introduction

$Dy_2Ti_2O_7$ has a pyrochlore lattice that consists of corner-sharing tetrahedrons with four Dy^{3+} ions at the corners. Due to the strong crystal field the spins of the Dy^{3+} ions are forced to point along the local {111} directions of the crystal that are pointing from the center of the tetrahedrons to their corners. Therefore, the spins can be seen as Ising spins with two states corresponding to pointing into or out of a tetrahedron.

At low temperatures the spins order in a spin-ice state, meaning that on every tetrahedron two spins point in and to spins point out. The name spin-ice was coined by Harris et al. [29] due to the similarity of this configuration with the hydrogen bonds in water ice where every oxygen has two hydrogen atoms that are close to the oxygen while the other two are further away. The phase diagram in a [111] magnetic field has been studied by Aoki et al. [2] and is shown in figure 5.1.

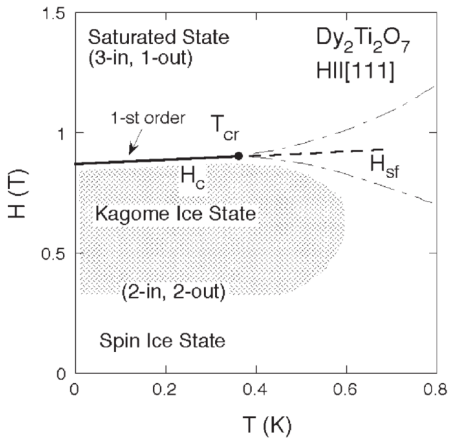

Figure 5.1: Phase diagram of $Dy_2Ti_2O_7$ in a [111] magnetic field, determined by magnetization and specific heat measurements.[1]

Recently $Dy_2Ti_2O_7$ has been in the focus of many researchers due to the emergence of magnetic Dirac monopoles at very low temperatures that were theoretically predicted by Castelnovo et al. in 2008 [10] and experimentally observed in 2009 by Morris et al. [56]. This excitations in the spin-ice state can be imagined as flipping one of the four spins of a tetrahedron and thus creating a 3-in-1-out configuration (three spins pointing to the center of the tetrahedrons, one spin pointing out) as shown in figure 5.2c. At the same time a 3-out-1-in configuration has to be created in the adjacent tetrahedron. The two configurations 3-out-1-in/3-in-1-out are called magnetic (Dirac) anti-/monopoles due to the fact that only a magnetic coulomb interaction between monopoles and anti-monopoles affects their movement in zero magnetic field. The density of magnetic monopoles depends on temperature and magnetic field and the calculations for zero magnetic field can be found in [44]. These calculations show that the number of magnetic monopoles is reduced with temperature below $\approx 6\,\mathrm{K}$. Here the second excited state, 4-in-0-out and 0-in-4-out, is no longer thermally activated as its activation energy of $6.6\,\mathrm{K}$[2] is higher than T.

Magnetic field in [111] direction

Using a magnetic field in [111] direction the ground state of $Dy_2Ti_2O_7$ can be tuned. First the spin parallel to the magnetic field in each tetrahedron will be aligned with the magnetic field while the other three spins are free. The formerly sixfold degenerate 2-in-2-out ground state in zero field is split into two threefold degenerate energy levels. This phase is called the kagome[3] ice state since the free spins are aligned in a kagome lattice and the 2-in-2-out ground state has to be realized by spin flips within the kagome planes. By further increasing the magnetic field the spins on the kagome planes will also be forced to point as far as possible into the magnetic field and the new ground state is a non degenerate 3-in-1-out state. In this phase a dense packing of alternating monopole/anti-monopole layers perpendicular to the [111] direction of the magnetic field is realized. The transition from the low field 2-in-2-out to the high field 3-in-1-out state is sometimes called a liquid to gas transition in continuation of the comparison to water. In this analogy the high field phase corresponds to the liquid phase due to its high density of magnetic monopoles/anti-monopoles and the low field phase corresponds to the gas phase. Indeed, the phase diagram of $Dy_2Ti_2O_7$ shown in figure 5.1 has a distinct similarity to the well known case of water, only at much lower temperatures and

[1] Reprinted figure with permission from Aoki et al., *JPSJ* **73**, 2851 (2004). Copyright 2004 by the Physical Society of Japan.
[2] This value was derived for a single tetrahedron model in [44].
[3] The name kagome is derived from a traditional Japanese braiding patten mostly used for bamboo baskets.

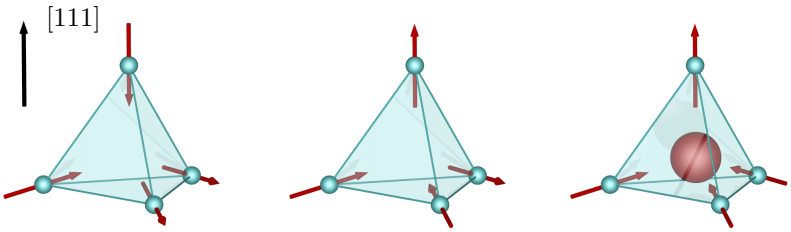

(a) Sixfold degenerate 2-in-2-out ground state in zero field.

(b) Threefold degenerate kagome ice state. Here the direction of the upper spin is fixed.

(c) Nondegenerate magnetic monopole ground state at high magnetic fields.

Figure 5.2: Tetrahedron configurations.
Ground state tetrahedron configurations in the phases observed with a [111] magnetic field. The magnetic field is increased from left to right.

magnetic field instead of pressure as the second parameter. The critical endpoint of this phase transition is located at $\mu_0 H_c = 1\,\mathrm{T}$ and $T_c = 0.36\,\mathrm{K}$.

Monopole dynamics

The dynamics of magnetic monopoles in zero field have been studied with magnetic ac susceptibility down to 0.3 K in a number of publications, *e.g.* [84, 93], that are qualitatively in agreement and the latter concludes that there is Arrhenius behavior, $\nu_p = \nu_0 \exp(-E_a/T)$, at temperatures below 1 K. Even though this was not discussed explicitly Vogel-Fulcher-Tammann behavior, $\nu_p = \nu_0 \exp(-E_a/T - T_{vft})$, with a small T_{vft} would also describe the susceptibility data.

In a [111] magnetic field the monopole dynamics were also studied at temperatures down to roughly 2 K [8] as a function of the magnetic field and the existence of two processes with different timescales was proposed. Despite the limited frequency range accessible with magnetic ac susceptibility measurements their careful examination in combination with Monte Carlo simulations for $Dy_2Ti_2O_7$ could be used to show critical speeding up near the critical field [87].

The nature of this processes has not been fully understood and it is not clear which processes have to be associated with magnetic monopoles as muon spin rotation (μSR) measurements [19] show the existence of magnetic excitations without monopole signatures in the low-temperature regime.

Dielectric properties of monopoles

First dielectric measurements on $Dy_2Ti_2O_7$ were done by Saito et al. in 2005 [75]. They examined the dielectric function at low temperatures for a fixed frequency of 1 kHz and explain their findings with local spin correlations among the moments of the tetrahedrons and not the individual Dy^{3+} ions.

In 2012 the formation of electric dipoles on top of the magnetic monopoles was proposed [39]. From symmetry considerations the electric dipole moment in all magnetic monopoles or antimonopoles always points from the center of the tetrahedron to the spin with the unique orientation with respect to the center of the tetrahedron as shown in figure 5.3. Here it can also be seen that the movement of a monopole will result in a change of net polarization in [111] direction. High

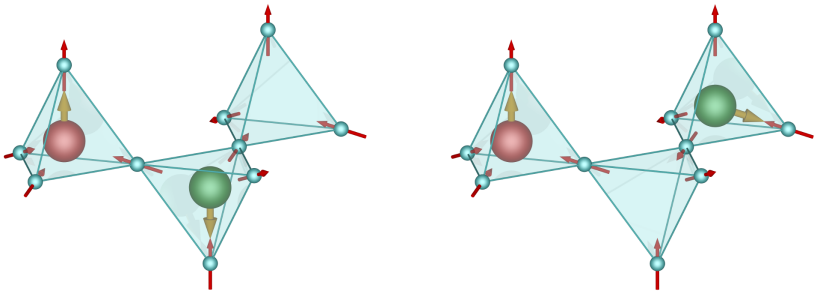

Figure 5.3: Dipoles on magnetic monopoles.
Dipoles (**yellow** arrows) on magnetic monopoles. The movement of a magnetic monopole also changes the net dipole moment in [111] direction.

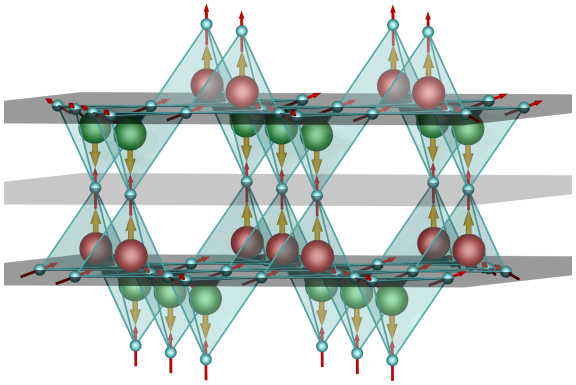

Figure 5.4: Antiferroelectric order in the high field phase.
The kagome layers are colored in dark gray, the trigonal layer in light gray. In the ground state of the high field phase the electric dipoles always point toward the trigonal layers.

magnetic [111] fields result in an antiferroelectric order at low temperatures, see figure 5.4, as the electric dipole moments in this phase will always point away from the kagome plane.

Thus the use of dielectric spectroscopy on $Dy_2Ti_2O_7$ is promising not only for studying its quantum paraelectric behavior but also to prove the existence of dipoles on magnetic monopoles. In addition it might help to understand the dynamics of the magnetic monopoles in the spin-ice phase as higher frequencies are accessible compared to magnetic ac susceptibility.

5.2 The pyrochlore structure

Materials with the pyrochlore[4] structure $A_2B_2O_6O'$ have been studied for many years. In fact the first description of a pyrochlore was published in 1826 after the mineral was found close to Frederiksværn (today: Stavern) in Norway [92]. The first compound to be found with this structure was $(Na,Cl)_2Nb_2O_6(OH,F)$, a naturally occurring mineral that was subsequently found in many regions around the globe.

Successively, many more materials with this structure were found or engineered

[4] The name is based on the greek language: $\pi\upsilon\rho$ (pyr): fire, $\chi\lambda\omega\rho\acute{o}\varsigma$ (chlorós): green/yellow and has been inspired by the yellow color that was observed during blowpipe analysis.

Ion	Loc.	Site Symm.	Coordinates			
			(0 , 0 , 0	0 ,½,½	½, 0 ,½	½,½, 0) +
16 *A*	16d	$\bar{3}m(D_{3d})$	½,½,½	½,¼,¼	¼,½,¼	¼,¼,½
16 *B*	16c	$\bar{3}m(D_{3d})$	0 , 0 , 0	0 ,¼,¼	¼, 0 ,¼	¼,¼, 0
48 O	48f	$mm(C_{2v})$	x ,⅛,⅛	$\bar{x}$,⅞,⅞	¼-x,⅛,⅛	¾+x,⅞,⅞
			⅛, x ,⅛	⅞, $\bar{x}$,⅞	⅛,¼-x,⅛	⅞,¾+x,⅞
			⅛,⅛, x	⅞,⅞, $\bar{x}$	⅛,⅛,¼-x	⅞,⅞,¾+x
8 O'	8b	$\bar{4}\bar{3}m(T_d)$	⅜,⅜,⅜	⅝,⅝,⅝		

Table 5.1: Position of the ion in the pyrochlore structure of space group $Fd\bar{3}m$. The oxygen parameter x measures the distortion of the structure and depends on the components A and B. A value of $x = 0.3125$ gives a regular octahedron while $x = 0.375$ represents a regular cube. For $Dy_2Ti_2O_7$ a value $x = 0.323$ has been reported [85].

for many different applications. A good review of the earlier research efforts on pyrochlore crystals can be found in [85].

Here only the (3+/4+) class of pyrochlore materials is briefly introduced where the A atom (Dy or Y in this work) has an oxidation state 3+ and the B atom (Ti) 4+. Table 5.1 gives the positions of the ions in the structure as a function of the oxygen x parameter that was reported as $x = 0.323$ for $Dy_2Ti_2O_7$ and $x = 0.328$ for $Y_2Ti_2O_7$ meaning that the latter compound consists of slightly stronger distorted octahedrons compared to $Dy_2Ti_2O_7$.

The crystallographic space group of the pyrochlore structure is $Fd\bar{3}m$ and stable growth conditions require the ratio of the inoic radii ${}^{r_{A^{3+}}}/_{r_{B^{4+}}}$ to reside in the range from 1.46 to 1.80 when growing the crystal at normal pressure. For the three ions used in this thesis the ionic radii from r^3 *vs* V plots are $r_{Dy^{3+}} = 1.027$, $r_{Y^{3+}} = 1.019$, and $r_{Ti^{4+}} = 0.605$ [81]. Their ratios ${}^{r_{Dy^{3+}}}/_{r_{Ti^{4+}}} = 1.698$ and ${}^{r_{Y^{3+}}}/_{r_{Ti^{4+}}} = 1.684$ are slightly in the upper half of the given range. Deviations from the optimal ratio may result in oxygen deprived samples, *i.e.* the chemical formula of the result is $A_2B_2O_{7-\delta}$ with $\delta > 0$, that are generally non-transparent and weaker insulators. This oxygen deficiency δ should be cured by annealing the sample in oxygen atmosphere before measurements as it has a strong influence on the physical properties of the materials.

5.3 Sample preparation

The high quality single-crystalline $Dy_2Ti_2O_7$ sample used in this work was supplied by Martin Valldor and already cut and oriented with the planes perpendicular to the crystalline [111] direction. Gold was chosen as contact material and was applied to the sample by sputtering using masks build from adhesive tape to define a rectangular shape for the electrodes. The final area of the contacts was measured using a calibrated microscope as $A = 7.0(1)\,\mathrm{mm}^2$ with a sample thickness of $d = 0.34(1)\,\mathrm{mm}$ resulting in a geometric capacity of

$$C_{\mathrm{geometric}} = 182(6)\,\mathrm{fF}. \tag{5.1}$$

For the dielectric measurements the sample was mounted on a microstrip sam-

ple holder designed for measurements in both a *Quantum Design "PPMS"* for measurements from 400 to 2 K and an *Oxford Instruments "Kelvinox"* dilution refrigerator for temperatures down to 0.02 K. Both cryostats are equipped with superconducting magnets with a maximum magnetic field of 14 (PPMS) or 13 T (Kelvinox). The sample was oriented on the sample holder for measurements with magnetic and electric field parallel to the crystalline [111] direction. With the sample thickness the applied ac voltage of $1\,V_{rms}$ translates to an alternating electric field $E_{ac} = 4.16\,V/mm$.

5.4 Demagnetization correction

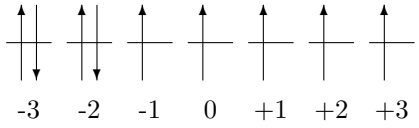

Figure 5.5: Spin configuration of Dy^{3+} according to Hund's rules.

The Dy^{3+}-ions in $Dy_2Ti_2O_7$ have a $[Xe]4f^9$ electron configuration that causes a very high magnetic moment. Using Hund's rules the $4f^9$ electrons have a total spin $S = 5/2$ and an orbital angular momentum $L = 5$. The total angular momentum in this case calculates as $J = L + S = 15/2$. Taking into account the gyromagnetic ratio $g = 4/3$ as calculated with the Landé equation this leads to the total magnetic moment per Dy^{3+}-ion of $m_{Dy} = g \cdot \sqrt{J(J+1)} = 10.65\,\mu_B$. As the crystal field forces the spins to orient with the local $\{111\}$ directions the average magnetic moment per Dy^{3+} has to take the reduced contributions of the ions located on the kagome planes into account. The directions of the magnetic moments for this ions are $[11\bar{1}]$, $[1\bar{1}1]$, and $[\bar{1}11]$ that are at an angle of 70.53° with respect to the [111] direction. Therefore, their contribution to the magnetization in field direction has to be reduced to $\cos(70.53°) = 1/3$ of m_{Dy} and the average magnetization per Dy^{3+} calculates to $m_{avrg} = (1 + 3 \cdot 1/3)/4 \cdot m_{Dy} = 5.32\,\mu_B$.

Due to this high magnetic moment and the geometry of the sample the demagnetization (see chapter 2.6) has to be taken into account. Therefore, the sample was simulated with Mathematica and the Radia software package provided by the ESRF[5] using the script shown in appendix B.3 on page 120. The magnetization data required for this calculations was taken from [44].

Figure 5.6 shows the exemplary $\mu_0 H_i(\mu_0 H)$ curves for different temperatures that were used to correct the known external magnetic field strength $\mu_0 H$ for the demagnetization of the sample. While the corrections for external magnetic field strength H above and below the critical field show a temperature dependence the applied critical field is temperature-independent at a value of $\mu_0 H_c \approx 1.63\,T$. The internal critical magnetic field strength $\mu_0 H_{i,c} = 1\,T$ is in agreement with the value found in other publications, *e.g.* [76, 2], and is an indication of the validity of the demagnetization correction. This result emphasizes the necessity to take the demagnetization into account as the applied magnetic field strength is reduced by more than 0.6 T due to the unfavorable geometry required for the dielectric measurements with parallel magnetic and electric fields. With this result also the demagnetization factor D of this sample in [111] direction can be calculated as $D = 0.98$.

All magnetic field values given in the remainder of this chapter have been corrected using this method unless explicitly stated otherwise.

[5] http://www.esrf.eu/Accelerators/Groups/InsertionDevices/Software/Radia

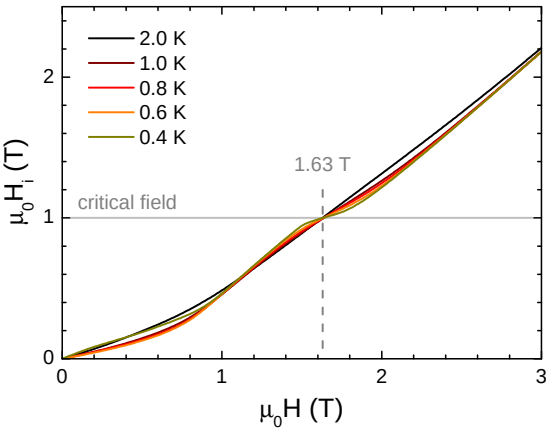

Figure 5.6: Demagnetization correction for the $Dy_2Ti_2O_7$ sample.
Calculated demagnetization of the $Dy_2Ti_2O_7$ sample used for measurements with E parallel to H in [111] direction. The magnetization data was taken from [44].

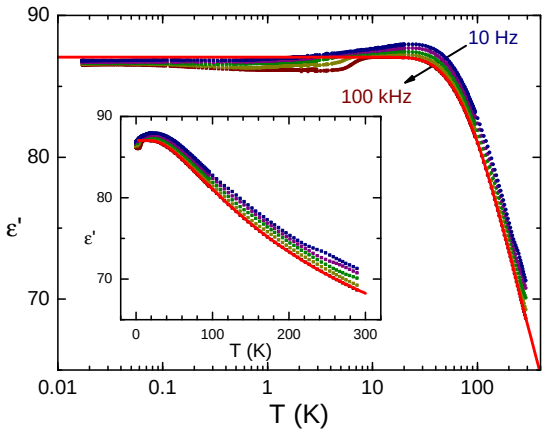

Figure 5.7: Quantum paraelectric properties.
The dielectric function of $Dy_2Ti_2O_7$ for temperatures up to 300 K with a fit of the Barrett formula. The negative coupling parameter from the fit indicates that $Dy_2Ti_2O_7$ is an incipient antiferroelectric.

5.5 Quantum paraelectric properties

Similar to the famous example of $SrTiO_3$ [34], $Dy_2Ti_2O_7$ also shows a non vanishing dielectric function at low temperatures. While its magnitude is much smaller—$SrTiO_3$ reaches a value of over 10000 in ε' compared to approximately 80 in $Dy_2Ti_2O_7$—the temperature dependence of the dielectric function can be nicely described by the Barrett formula that was introduced in equation (1.21) on page 13.

In figure 5.7 the resulting fit is plotted. Contrary to the results in $SrTiO_3$ the coupling parameter $J_0/k_B = -850(45)\,K$ is negative. Therefore, $Dy_2Ti_2O_7$ should be called an incipient antiferroelectric material in contrast to the incipient ferroelectric $SrTiO_3$ that has a positive coupling constant J_0/k_B.

The remaining parameters obtained from the fit of the Barrett formula are: $nk_B\mu^2 = 11\,350(630)\,K$, $\Omega/k_B = 132(3)\,K$, and $\varepsilon_\infty = 45.3(80)$.

The agreement with the measurement is almost perfect at temperatures above 10 K, at lower temperatures a deviation from the fit is observed. There the onset of the spin-ice regime causes a step-like reduction of the permittivity. At very low temperatures the permittivity rises until the original value is almost recovered at 0.02 K.

5.5.1 Nearly constant loss

Many quantum paraelectric materials also exhibit a so called nearly constant loss behavior where the dielectric loss is nearly constant over a broad frequency range. This is attributed to the quantum tunneling of the titanium ions between different off-center positions in the distorted TiO_6-octahedrons. In $Dy_2Ti_2O_7$ this effect is very pronounced and a distinct constant loss behavior can be seen even at room temperature.

The constant loss contribution can be seen in the spectra in figure 5.8 as a linear slope in ε' at frequencies below 1 kHz in the upper frame and even more clearly in the offset present in ε'' shown in the lower frame of the same figure. This additional feature complicates the evaluation of the measured spectra, as the sum of the Havriliak-Negami function (equation (1.16)) and the constant loss contribution given in equation (1.29) have to be fitted simultaneously. Therefore, the real and imaginary part of the measured dielectric spectra were fitted using the equation

$$\underline{\varepsilon}(\nu) = \frac{\Delta\varepsilon}{\left(1 + (\mathrm{i}2\pi\nu\tau_{\mathrm{HN}})^{\beta}\right)^{\gamma}} - \frac{2\varepsilon_{\mathrm{c.l.}}}{\pi}\log_{10}(\nu/\nu_0) + \mathrm{i}\varepsilon_{\mathrm{c.l.}} + \varepsilon_{\infty} \tag{5.2}$$

that is basically the combination of the previously mentioned equations. The reference frequency ν_0 used in the fit was chosen arbitrarily as the lowest measured frequency of 10 Hz. For the fit the real and imaginary part of the permittivity were weighted differently for two reasons:

- Due to the chosen fitting method the higher absolute value in the real part $\varepsilon' \approx 80$ compared to the imaginary part $\varepsilon'' \approx 0.15$ of the complex permittivity causes an higher effective weight on the real part when calculating the quality of the resulting fit.
- Secondly the separation of the relaxation and the constant loss contribution is easier in ε'' where the latter part has no frequency dependence.

Therefore, the imaginary part of the permittivity was deemed more accurate in the description of the relaxation process and was weighted with 1 while the real part was weighted with only a small weight of 0.02.

The good agreement between the measurements at 0.6 K and the plotted fit of equation (1.29) in figure 5.8 shows that the assumption of only this two contributions to the dielectric response is reasonable. Here also a first indication of the monopole dynamics is apparent: the position of the peak in ε'' shifts to higher frequencies close to the critical field. This aspect will be covered in detail in chapter 5.6.2. At this field a deviation between the measurement and the fit occurs when the peak is very close to the upper frequency limit of the measurement and its down slope could not be measured.

In the same figure measurements of the dielectric loss of $Y_2Ti_2O_7$ are shown in gray. As $Y_2Ti_2O_7$ is a non-magnetic isostructural compound to $Dy_2Ti_2O_7$ and is missing the prominent peak seen in $Dy_2Ti_2O_7$ this contribution can be said to originate in the magnetic structure. A nearly constant loss contribution on the other hand is also present in $Y_2Ti_2O_7$ and shows no magnetic field dependence. The results on $Y_2Ti_2O_7$ are discussed in detail in chapter 6 from page 103 onwards.

Figure 5.9 shows the temperature and magnetic field dependence of the constant loss below 2 K. $\varepsilon_{\mathrm{c.l.}}$ has a maximum at 0.5 K that is indicated by the color gradient.

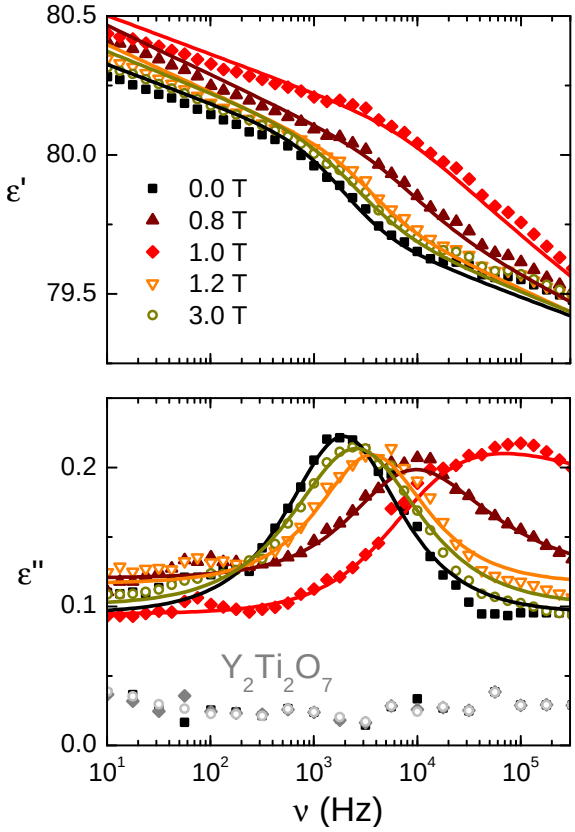

Figure 5.8:
Fits of Havriliak-Negami and constant loss.
Fits (lines) of the sum of the Havriliak-Negami and constant loss contributions from equation (5.2) to the measurements (points) of $Dy_2Ti_2O_7$ at 0.6 K and different magnetic fields. The fits were done using both the real and imaginary part of the permittivity.
In gray (•), measurements of the non-magnetic isostructural compound $Y_2Ti_2O_7$ are included in the dielectric loss. As expected these spectra show no peak and are independent of the magnetic field.

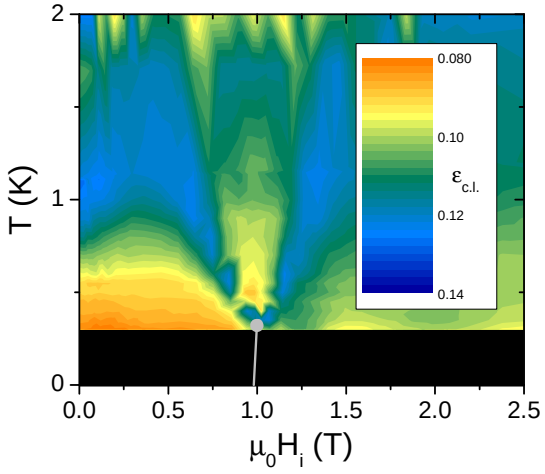

Figure 5.9:
Constant loss contribution.
Temperature and magnetic field dependence of the nearly constant loss contribution $\varepsilon_{c.l.}$ in $Dy_2Ti_2O_7$.

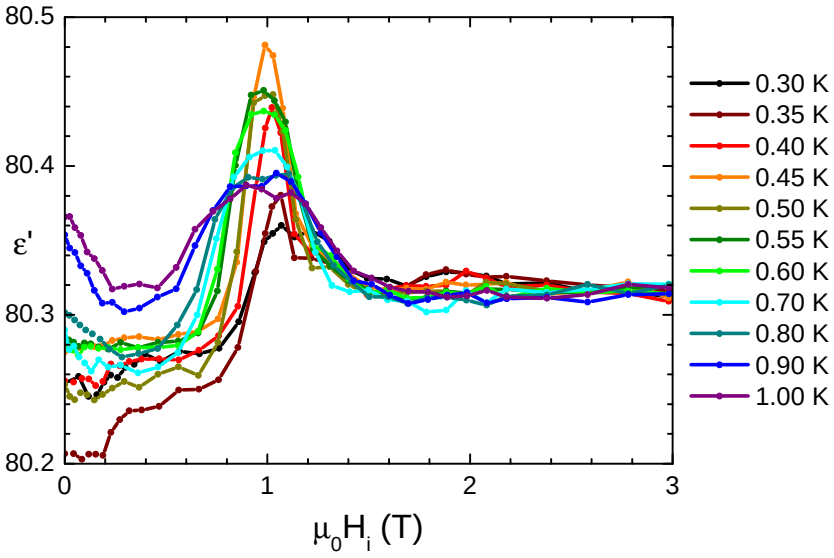

Figure 5.10: $\varepsilon(10\,\mathrm{Hz})$.
The permittivity of $Dy_2Ti_2O_7$ for the lowest measured frequency of 10 Hz. Some of the curves have been slightly shifted so that they coincide at high magnetic field.

At lower temperatures the constant loss is reduced with temperature but this reduction has different slopes on either side of the critical field.

This results also show that it is not possible to assume the constant loss to be independent of the magnetic system and implies a coupling between the magnetic system and the Ti-ions via the crystal lattice.

5.6 Dynamics of Magnetic Monopoles

After the previous discussion of the dielectric background caused by the quantum paraelectric nature of $Dy_2Ti_2O_7$ in the following the focus will be shifted to the dynamical properties of its magnetic spin structure observed with dielectric spectroscopy. To that end the remaining fit parameters from equation (5.2) will be discussed in detail after an excursion to quasi static magnetic field dependent measurements that are used to characterize the phase diagram by fitting the critical exponents of the crossover lines.

5.6.1 The thermodynamic limit: $\nu \to 0\,\mathrm{Hz}$

Assuming there are no additional features below the slowest measured frequency this measurement can be treated as identical to a dc measurement. But due to the constant loss contribution present in $Dy_2Ti_2O_7$ it has to be kept in mind that the actual $\nu = 0\,\mathrm{Hz}$ measurement would at least be shifted to a higher absolute value that can not be easily inferred from the measurement because equations (5.2) and (1.29) diverge in the limit of $\nu_0 \to 0\,\mathrm{Hz}$.

Still, the best possible approximation of a dc measurement is made by using the results from the lowest measured frequency—in this case 10 Hz—as shown in

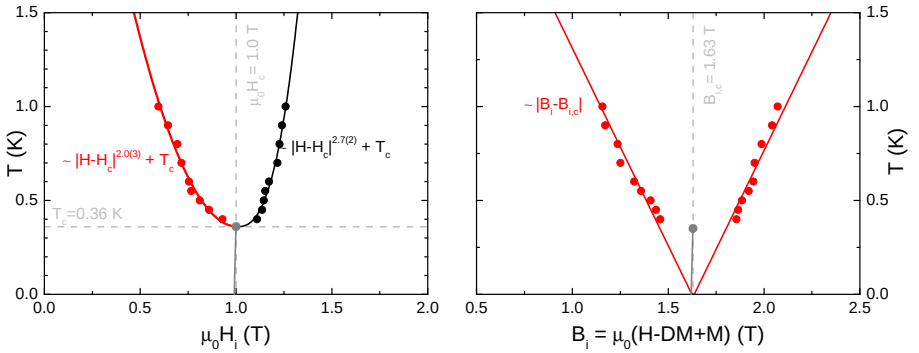

(a) internal magnetic field strength **(b)** magnetic flux density

Figure 5.11: Inflection points from the 10 Hz data.
The inflection points of the 10 Hz data shown in figure 5.10 as a function of (a) the internal magnetic field strength H_i and (b) the magnetic flux density B_i. The difference in the critical exponents of both plots shows that non-mean-field behavior is observed.

figure 5.10 as a function of magnetic field for different temperatures. Beginning at the 1 K curve with increasing magnetic field the permittivity decreases until it reaches a plateau at 0.4 T. At higher fields a broad peak centered around 1 T follows before a second plateau begins at 1.8 T that is independent of the magnetic field. Reducing the temperature also reduces both the decrease at low magnetic fields as well as the value of the first plateau while the peak centered on 1 T becomes narrower and higher. The second plateau shows no systematic change with temperature.

From the peaks in this quasi-static measurements the inflection points as a function of temperature can be used to define thermodynamic crossover lines at temperatures above 0.36 K. This is done by finding the magnetic fields of the inflection points of the peak for different temperatures. After scaling $t = T - T_\mathrm{c}$ and $b = \mu_0(H_\mathrm{i} - H_\mathrm{i,c})$ these positions can be fitted with $t \sim b^\alpha$ to obtain a critical exponent on either side of the critical magnetic field, and the results are shown in figure 5.11a. With $T_\mathrm{c} = 0.36\,\mathrm{K}$ and $\mu_0 H_\mathrm{i,c} = 1\,\mathrm{T}$ this yields a critical exponent of $\alpha_\mathrm{low} = 2$ for the low field and $\alpha_\mathrm{high} = 2.6$ for the high field branch.

The same consideration can also be done for the magnetic flux density B_i. As discussed in chapter 2.6.1 for a planar sample this can be approximated with the applied magnetic field: $B_\mathrm{i} \approx \mu_0 H$. Figure 5.11b shows that in this case the inflection points can be fitted with a single critical exponent $\alpha = 1$ and $T_\mathrm{c} = 0\,\mathrm{K}$.

For mean field crossover lines both the asymmetry and the difference in the exponents for the internal magnetic field strength and the magnetic flux density are not expected, as $B_\mathrm{i} = \mu_0(H_\mathrm{i} + M)$ and adding multiples of the magnetization should not change the critical behavior.

5.6.2 Peak position and relaxation time: critical speeding up

As already mentioned in chapter 5.5.1 the position of the peak in the dielectric loss of $Dy_2Ti_2O_7$ depends at least on the magnetic field. The peak position ν_p is calculated from the parameters of the Havriliak-Negami fits with equation (1.17)

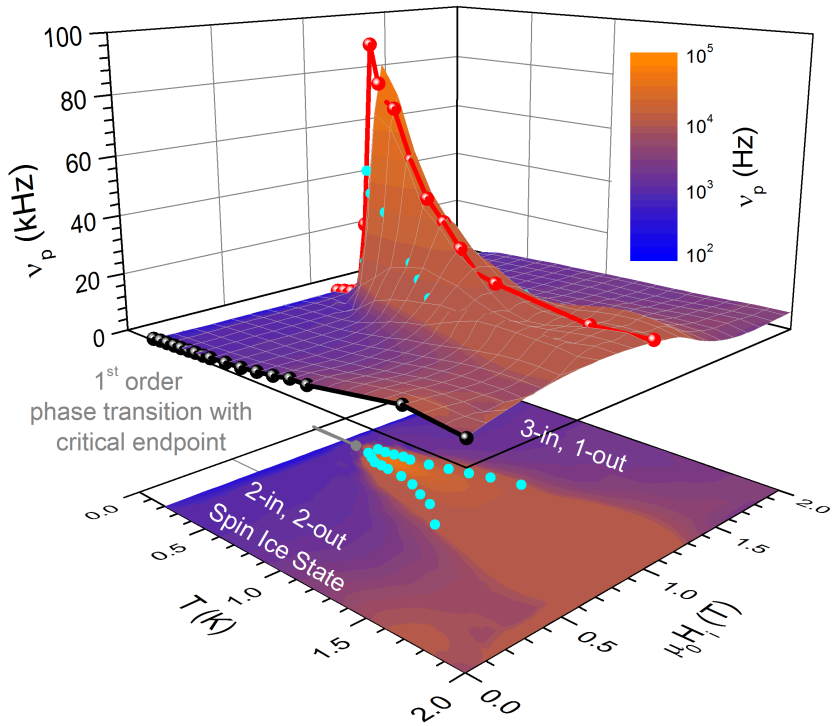

Figure 5.12: 3D plot of ν_p.
The position of the peak in ε'' as calculated from the fit parameters from equation (5.2) at low temperatures as 3D surface and logarithmic color plot that is a very good reproduction to the known phase diagram. At low and high magnetic fields critical slowing down is observed: $\nu_p \propto (T - T_c)^\alpha$ with $\alpha > 0$. Above the critical field the exponent α changes its sign and becomes negative. This behavior is called critical speeding up.
The blue dots mark the FWHM at constant temperature and are discussed in the main text in more detail.

for further investigation of its temperature and magnetic field dependence. In the case of a symmetric function ν_p leads to the relaxation time τ of the magnetic excitation via equation (1.14).

The results for $\nu_p(H_i, T)$ as found from the measurements is shown in figure 5.12 as logarithmic color plot that is the projection of the 3D surface. Without going into detail it is obvious that this representation of the dynamical results directly reproduces the known phase diagram of $Dy_2Ti_2O_7$ as seen in literature, for example in [2] (also shown on page 82). This observation alone gives a very strong argument for the assumption that the measured dynamics are indeed caused by the critical endpoint of the monopole condensation in $Dy_2Ti_2O_7$.

For a detailed discussion of the temperature dependence, cuts through this diagram at different constant magnetic fields are shown in figure 5.13. At low and high magnetic fields a slowing down of the dynamics with temperature occurs that is roughly linear in $T - T_c$ that can be seen in the color gradient and even more clearly in the black dots that mark the measured zero field values of ν_p. Such a

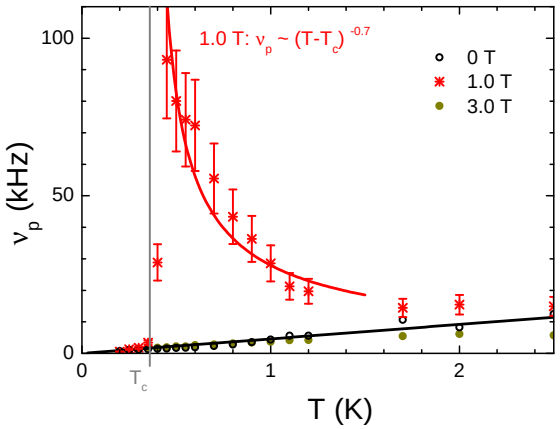

Figure 5.13:
Relaxation time at constant magnetic fields.
The relaxation time at three different constant magnetic fields. At the critical field of 1 T the fit yields a critical exponent α of roughly -0.7.

behavior is called critical slowing down and can be observed close to ferroelectric phase transitions [5] as well as in the vicinity of a (quantum) critical endpoint [74].

At the critical field, however, a completely different behavior emerges. Instead of slowing down the dynamics of the magnetic monopoles actually speeds up by more than two orders of magnitude. This critical speeding up can be described as

$$2\pi\nu_\mathrm{p}\,(T) \propto (T - T_\mathrm{c})^{\alpha} \tag{5.3}$$

with a negative dynamical critical exponent α that can be found from the experimental results to be between -0.7 and -1.

The concept of critical speeding up is not a novel one and has previously observed for example in the piston effect of gases in zero gravity [94]. While the previous example is relatively far away from the topic of this work critical speeding up has been theoretically proposed for a Kasteleyn transition of the magnetization plateau in [111] magnetic field in spin-ice [54, 16]. Though this example of critical speeding up is proposed for the correct type of material the control parameter for the Kasteleyn transition would be the misalignment angle between the magnetic field and the crystallographic [111] direction. Since the sample has not been rotated during the measurements this mechanism also seems to be unsuited to explain this experimental results. But as already mentioned in the introduction critical speeding up at the critical field has also been observed in magnetic ac susceptibility measurements and Monte Carlo simulations [87].

Finally, below the critical temperature of 0.36 K the relaxation process vanishes.

Critical exponents

The peak frequency ν_p can also be used to define dynamical crossover lines using a similar approach as with the quasi-static measurements. Here the FWHM is used, calculated for $\nu_\mathrm{p}(\mu_0 H_\mathrm{i})$ at different temperatures, the results are shown in blue (•) in figure 5.14. Compared to the inflection points from the quasi-static measurements also shown in the same figure in yellow (•), the shape of the crossover lines is markedly different. After rescaling they can be described via $T - T_\mathrm{c} \propto |H_\mathrm{i} - H_\mathrm{i,c}|^{\alpha}$ with a critical exponent $\alpha = 2/3$ as predicted by mean field calculations [82]. Additionally, the critical exponent α does not change when using the magnetic flux density instead of the magnetic field strength.

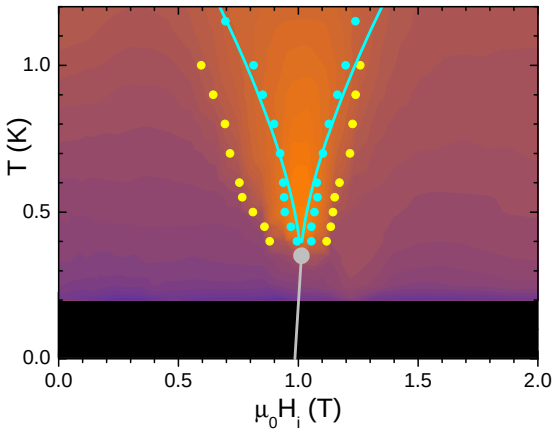

Figure 5.14:
Crossover lines.
Crossover lines obtained from the quasi static measurements (yellow •) and the relaxation time (blue •). The critical exponent $\alpha = 2/3$ found from the relaxation time is in good agreement with predictions from mean field theory. The color plot of ν_p in the background uses the same colors as in figure 5.12.

5.6.3 Broadening of the peak

A broadening of the peak in $\varepsilon''(\nu)$ is typically caused by a distribution of relaxation times that is present in all solids due to small deviations of local domains from the perfectly uniform crystal.

The Havriliak-Negami function allows for symmetric and asymmetric broadening via the parameters β_{HN} and γ_{HN} where a value of 1 in either parameter denotes no asymmetric/symmetric broadening. In the color plot shown in figure 5.15a it can be seen that the symmetric broadening of the peaks is almost independent of the magnetic field but is reduced with temperature. Even in the proximity of the critical point β_{HN} deviates only in few measured spectra from this independence of the magnetic field.

The asymmetric broadening parameter γ_{HN} of the peaks on the other hand only deviates from unity close to the critical field at temperatures above 0.36 K as shown in figure 5.15b. For lower and higher magnetic fields or temperatures above 2 K the spectra show no asymmetric broadening. Therefore, the asymmetry of the peak can be said to have its origin in the critical behavior close to the phase transition. Similar observations have also been made in [8] for measurements of the magnetic ac susceptibility in the vicinity of the critical field at 2 K.

Directly above the critical point the asymmetric broadening of the peak might be overestimated due to missing data for the down slope as the peak almost reaches the upper frequency limit for the measurements, as can be seen exemplary in the 1 T curve in figure 5.8 on page 89.

5.6.4 Relaxation strength $\Delta\varepsilon$ & the dielectric background ε_∞

Evaluating the strength of the relaxation that is described by the fit parameter $\Delta\varepsilon$ in equation (5.2) offers information about the amount of polarization that can be moved with the applied electric field at given temperature and magnetic field. This information can be found in both parts of the complex permittivity, either the height of the step in ε' or the area of the peak in ε'' on a logarithmic frequency scale, as can be seen from the Kramers-Kronig relations given in equations (1.25a) in the limit of $\omega \to 0$ and (1.25b). Both sources of information are entering into $\Delta\varepsilon$ obtained from the fits.

In figure 5.16a the relaxation strength $\Delta\varepsilon$ as a function of temperature is shown for different magnetic fields. A reduction of the temperature at any magnetic field

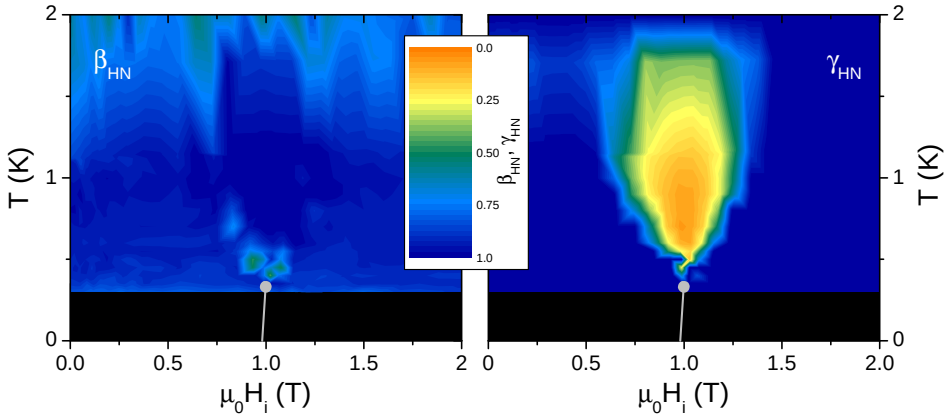

(a) The symmetric broadening parameter β_{HN}.

(b) Asymmetric broadening γ_{HN} shows a significant contribution only close to the critical field. This

Figure 5.15: Broadening parameters β_{HN} and γ_{HN}.
The symmetric broadening parameter β_{HN} is plotted in (a). Below 1 K the peaks are not symmetrically broadened as indicated by the value of 1 (blue) for β_{HN} and no systematic dependence on the magnetic field is observed. The asymmetric broadening parameter γ_{HN} in (b) only contributes close to the critical field at low temperatures.

shown except the critical field reduces the relaxation strength roughly linearly with temperature. This tendency is in agreement with the predicted temperature dependence of the density of magnetic monopoles published for zero magnetic field *e.g.* in [44]. At the critical field of 1 T an increase in $\Delta\varepsilon$ can be observed with its maximum at 0.70 K, much higher than the critical temperature of $T_{\mathrm{c}} = 0.36$ K. In gray a Curie-Weiss law $1/(T - T_{\mathrm{c}})$ is fitted to the increase in the relaxation strength at the critical field.

Figure 5.16b shows $\Delta\varepsilon$ as a color plot in more detail for temperatures below 2 K that again reproduces the phase diagram of $Dy_2Ti_2O_7$. The reduction of $\Delta\varepsilon$ with temperature can be seen in the color gradient visible outside the cone above the critical endpoint marked by the crossover lines. Within the critical regime there is a very steep and narrow peak with nearly four times the relaxation strength compared to the zero field measurement at the same temperature.

Finally, the temperature and magnetic field dependence of ε_∞ can also be evaluated from the measurements and the corresponding color plot is shown in figure 5.17.

ε_∞ displays a strong dependence on the magnetic field that is similar to $\Delta\varepsilon$ but with a decrease close to the critical field where $\Delta\varepsilon$ shows an increase. As in this field range the peak shifts to high frequencies and the down slope of the peak is not completely observed. The question arises whether only an error in the fit shifts weight between both parameters. To answer this the sum of $\Delta\varepsilon + \varepsilon_\infty$ is considered in figure 5.18 for two exemplary temperatures.

There the prominence of the change close to the critical field can be seen for both temperatures shown. Although an error in the fit due to the position of the peaks at the edge of the measured spectra can not be excluded and the exact value of $\Delta\varepsilon$ might not be identified correctly the overall dependence on magnetic field and

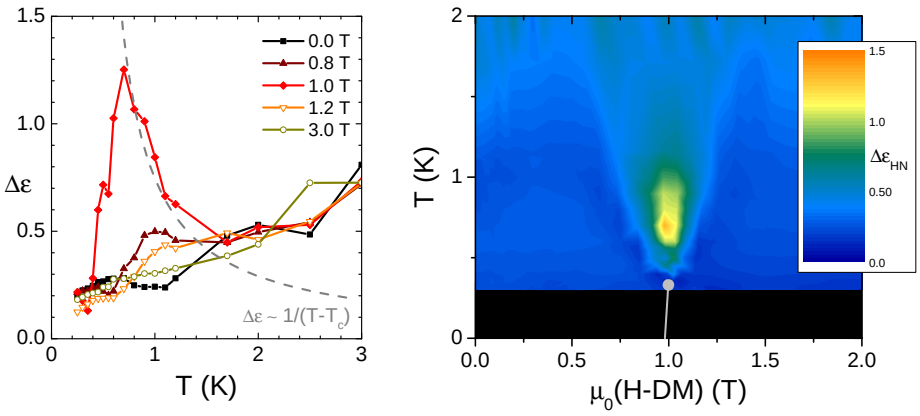

(a) $\Delta\varepsilon$ as a function of temperature.

(b) $\Delta\varepsilon$ in detail for temperatures below 2 K.

Figure 5.16: Relaxation strength $\Delta\varepsilon$.
(a) shows the relaxation strength $\Delta\varepsilon$ as a function of temperature. For all magnetic fields except the critical field of 1 T $\Delta\varepsilon$ is reduced roughly linear with temperature. At the critical field $\Delta\varepsilon$ has a maximum located at 0.7 K, the increase above 0.7 K can be described with a Curie-Weiss law (gray ▬). The color plot of $\Delta\varepsilon$ in (b) reproduces the known phase diagram of $Dy_2Ti_2O_7$ and illustrates that the peak is only seen in a very narrow magnetic field range.

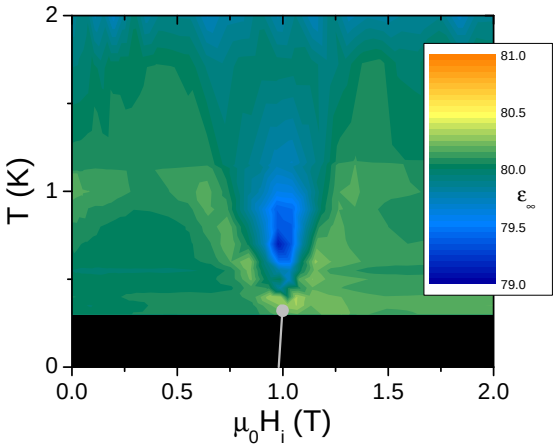

Figure 5.17: Offset ε_∞.
Temperature and magnetic field dependence of ε_∞ for temperatures below 2 K.

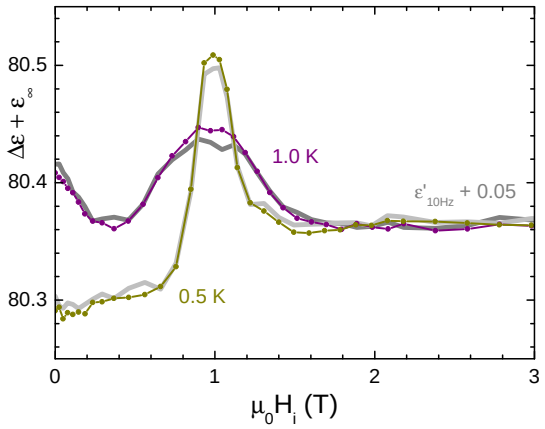

Figure 5.18: $\Delta\varepsilon + \varepsilon_\infty$. Sum of $\Delta\varepsilon + \varepsilon_\infty$ at two different temperatures as function of the magnetic field. In gray the 10 Hz data from figure 5.10 shows good agreement with the fit results. Due to the chosen reference frequency in the fit of the constant loss background the measured spectra were shifted by +0.05.

temperature has been represented correctly.

5.7 Comparison to the magnetic ac susceptibility

As the dynamics of $Dy_2Ti_2O_7$ can also be studied with magnetic ac susceptibility, it is interesting to compare those results to the dielectric measurements. To that end magnetic ac susceptibility measurements at 2 K were done in a SQUID and shown together with the results obtained by dielectric spectroscopy in figure 5.19a. The frequency ν_p where the imaginary part χ'' shows a peak and the step in the real part χ' has its inflection point defines the effective relaxation time of the underlying process with $\tau = 1/2\pi\nu_p$. At 2 K ν_p is found as $\nu_p \approx 350$ Hz in good agreement with values found in literature [53, 52, 93]. Even though the experimental limit for this measurements was $\nu \leq 1.2$ kHz it can be noted that $\chi'(\nu)$ is leveling off at a finite value at high frequency, hinting at a second process with a faster relaxation time and higher peak frequency. This again is in agreement with the proposal of an isothermal (slow) and an adiabatic (fast) contribution from [8].

In the lower frame of figure 5.19a the constant loss contribution and ε_∞ have been subtracted from the permittivity. Here the slower process is not visible while a faster process with $\nu_p \approx 10$ kHz can be observed.

Figure 5.19b shows the effect of a magnetic field in [111] direction on χ' in the upper frame. Increasing the magnetic field suppresses the slower process until only the faster process survives at the critical field. Even higher fields also suppress the second process and at approximately 2 T the ac susceptibility completely vanishes.

In the lower frame of the same figure the corresponding measurement with dielectric spectroscopy is shown, again the constant loss contribution has been removed. The vanishing of the slow process at low magnetic fields has no influence on the permittivity while the influence of the second process can be seen *e.g.* in the 10 kHz curves close to the critical field. This is a first indication that the slower process might not be associated with the movement of single magnetic monopoles.

$DyYTi_2O_7$

To better understand the nature of the different processes seen in $Dy_2Ti_2O_7$, measurements of the magnetic ac susceptibility on the doped spin-ice $DyYTi_2O_7$ were performed. In this compound two magnetic Dy ions per tetrahedron are

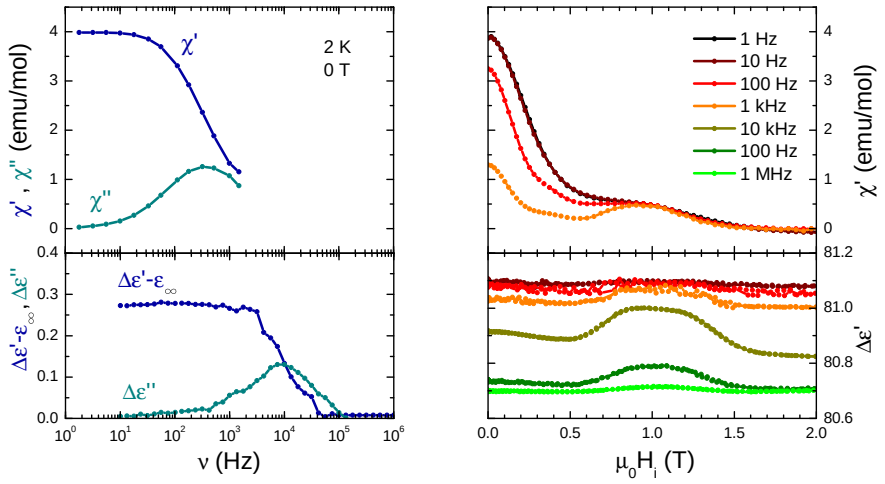

(a) Frequency sweep at 0 T

(b) Field-dependent measurement

Figure 5.19: ac-susceptibility and permittivity at 2 K.
Spectra of the complex magnetic ac susceptibility and the complex permittivity at 2 K.

replaced by non-magnetic Y ions and no spin-ice physics can occur. Figure 5.20b shows the dependence of the magnetic ac susceptibility of $DyYTi_2O_7$ on a static magnetic field at 2 K. The only visible feature is a slow relaxation process at zero field that is suppressed by the static magnetic field. Comparing this results to the previously discussed magnetic field dependent measurements on $Dy_2Ti_2O_7$ the removal of two magnetic spins per tetrahedron also removes the second, faster process while not changing the slower process.

Also a temperature-dependent measurement at zero static magnetic field shown in figure 5.20a and the corresponding measurement on $Dy_2Ti_2O_7$ shown in the inset of the same figure show the same qualitative behavior for low frequencies. In gray fits of Curie's law to the 1 Hz measurements on both materials are shown and in the case of $DyYTi_2O_7$ with a constant $C = 9.806(34)$ emu K/mol this agrees very well with the measurements and confirms the paramagnetic nature of $DyYTi_2O_7$. The undoped $Dy_2Ti_2O_7$ also shows an increase of χ' with decreasing temperature but a deviation from Curie's law is observed that has to be attributed to the strong spin-spin correlations in the spin-ice phase. Apart from this the other visible difference between both materials is the prominent kink seen in the 1 kHz curves of $Dy_2Ti_2O_7$, that is well established in literature [84], and absent in the doped compound. This further indicates that the high-frequency contribution plays an important role in the monopole physics in spin-ice.

Another indication against the monopole origin of the low-frequency peak is the curve shape itself. The predicted decay of the monopole density with temperature at low magnetic fields [44] implies a reduction of the monopole signal with temperature in contrast to the increase of the low-frequency contribution measured in $Dy_2Ti_2O_7$ that almost follows Curie's law as discussed before.

Therefore, the nature of the slow peak can be associated with collective spin reorientation that, while changing the magnetization direction, neither breaks the 2-in-2-out ground state nor creates electric dipole moments. One idea for such a

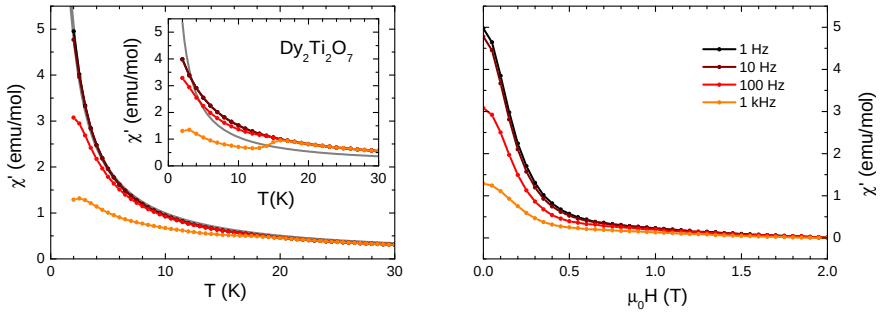

(a) Temperature-dependent measurements in zero magnetic field. In the inset the measurement for $Dy_2Ti_2O_7$ is shown.

(b) Field-dependent susceptibility measurement on $DyYTi_2O_7$ at 2 K.

Figure 5.20: χ_{ac} measurements on $DyYTi_2O_7$ and $Dy_2Ti_2O_7$. (a) Curie's law describes the low frequency measurements on the doped compound very good while deviations are observed for the spin-ice in the inset. (b) The ac susceptibility measurement on $DyYTi_2O_7$ shows no critical behavior in a magnetic field up to 2 T opposed to the observed peak in $Dy_2Ti_2O_7$ shown in figure 5.19.

process is flipping all spins on a closed loop as shown for the smallest loop possible in figure 5.21. In this example the net magnetic moment $\mu_{[111]}$ in [111] direction changes its sign while the net dipole moment remains zero.

5.8 Polarization measurements

Measuring the polarization of $Dy_2Ti_2O_7$ with a Keithley Electrometer at zero field and very low temperatures reveals no switchable polarization as can be seen in figure 5.22. The slope observed in the measurements is connected to the permittivity of the sample with

$$\varepsilon' = \frac{1}{\varepsilon_0}\frac{\mathrm{d}P}{\mathrm{d}E} + 1 \tag{5.4}$$

and using this equation the permittivity can be calculated as $\varepsilon' \approx 77.8$ at both temperatures. This result is in reasonable good agreement with the values obtained from the dielectric spectroscopy measurements.

5.9 Magneto-electric coupling in $Dy_2Ti_2O_7$

The origin of the magneto-electric coupling in spin-ice compounds has been proposed on a microscopic scale as breaking of inversion symmetry in the 3-in-1-out tetrahedrons [39]. On the macroscopic scale many theories concerning the magnetic properties have been proposed that do not make any predictions for either the thermodynamic permittivity or its frequency dependence. From symmetry considerations the simplest magneto-electric coupling allowed is a $< PPMM >$ coupling. As only the magnetization $< M >$ is accessible with measurements some

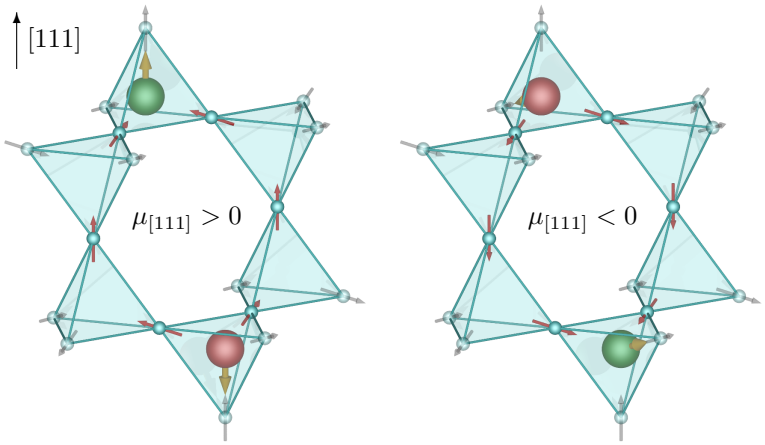

Figure 5.21: Magnetic ring excitation.
Example of a magnetic excitation that does not break the 2-in-2-out ground state. The net magnetic moment $\mu_{[111]}$ of the inner loop (red • arrows) changes its direction from down (left) to up (right).

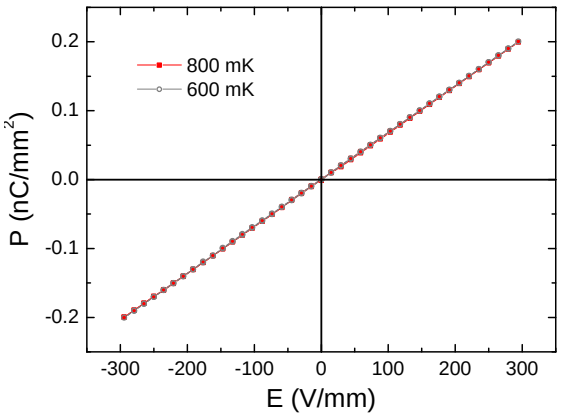

Figure 5.22: Polarization measurements in zero magnetic field.
Both curves show no hysteresis, from the slope of the curves the permittivity of the sample can be calculated as $\varepsilon' \approx 77.8$.

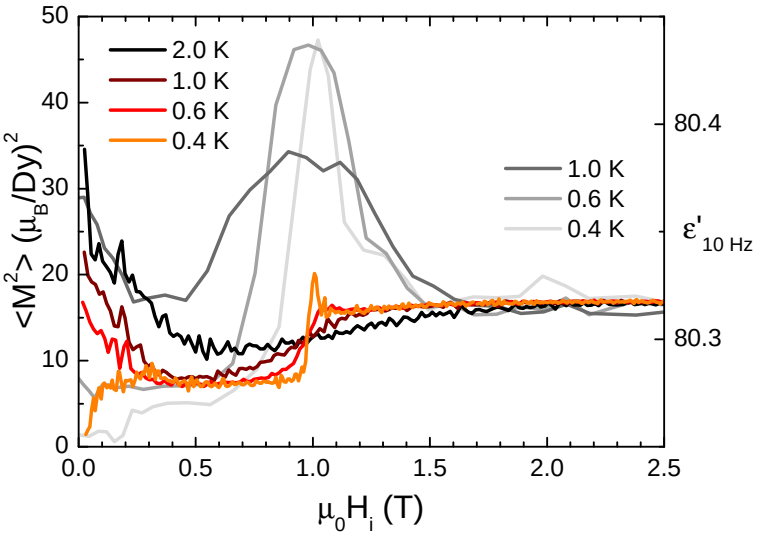

Figure 5.23: Scaled magnetization data.
The scaling described in equation (5.6) applied to the magnetization data from [44]. A comparison with the quasi-static permittivity from figure 5.10 (gray curves) shows that the plateaus are reproduced even without taking interactions between the Dy ions into account.

deliberations have to be made on how to calculate $< M^2 >$ from $< M >$. Therefore, the derivative of the magnetization $< M >$ with respect to the magnetic field is calculated in the limit of non interacting spins

$$\begin{aligned}\frac{\partial}{\partial(\mu_0 H)} < M > &= \frac{\partial}{\partial(\mu_0 H)} \frac{\mathrm{Tr}\left\{\mathrm{e}^{-\beta(E-\mu_0 HM)} M\right\}}{\mathrm{Tr}\left\{\mathrm{e}^{-\beta(E-\mu_0 HM)}\right\}} \\ &= \frac{\mathrm{Tr}\left\{\mathrm{e}^{-\beta(E-\mu_0 HM)} \beta M M\right\}}{\mathrm{Tr}\left\{\mathrm{e}^{-\beta(E-\mu_0 HM)}\right\}} \\ &- \frac{\mathrm{Tr}\left\{\mathrm{e}^{-\beta(E-\mu_0 HM)} M\right\}}{\mathrm{Tr}\left\{\mathrm{e}^{-\beta(E-\mu_0 HM)}\right\}^2} \mathrm{Tr}\left\{\mathrm{e}^{-\beta(E-\mu_0 HM)} \beta M\right\} \\ &= \beta\left(< M^2 > - < M >^2\right) = \chi \end{aligned} \tag{5.5}$$

where $\beta = 1/k_\mathrm{B}T$. With this $< M^2 >$ can be calculated from the measurable magnetization $< M >$ by:

$$< M^2 >= \left(< M^2 > - < M >^2\right) + < M >^2 = k_\mathrm{B}T\chi + < M >^2 \tag{5.6}$$

In figure 5.23 this scaling is applied to the magnetization data from [44] that was also used to calculate the demagnetization of the sample.

Comparing this results to the quasi-static permittivity in figure 5.10 the plateaus at ≈ 0.5 and above 2 T are nicely reproduced. The peak close to the critical field is missing, but this is expected as the assumption of non-interacting spins in equation 5.6 cannot hold close to the phase transition where the correlation length is diverging. A better description of the permittivity close to 1 T should be

achievable when introducing the spin-spin correlations as a perturbation of second order.

5.10 Conclusion

The dynamical properties of $Dy_2Ti_2O_7$ measured with dielectric spectroscopy are strongly linked to the dynamics of magnetic monopoles. All parameters of the fitted curves except the symmetric broadening parameter β_{HN} reproduce the phase diagram of $Dy_2Ti_2O_7$ in [111] magnetic field when plotted as color plots 5.9, 5.12, 5.15b, and 5.16b for temperature and magnetic field.

Comparing the magnetic ac susceptibility to the dielectric measurements shows that the latter only sees the faster of two processes that have been proposed [8]. Measurements on the isostructural compound $DyYTi_2O_7$ show that the slower process remains visible even when removing half the magnetic spin per tetrahedron and the spin-ice physics is destroyed. Only the faster process is effected by this doping and is not present in $DyYTi_2O_7$. Therefore, this process has to originate from the spin-ice physics present only in $Dy_2Ti_2O_7$.

Studying the results from the dielectric spectroscopy measurements close to the critical endpoint of the monopole liquid-gas transition at $T_{\mathrm{c}} = 0.36\,\mathrm{K}$ and $\mu_0 H_{\mathrm{i,c}} = 1\,\mathrm{T}$ reveals anomalous dynamical behavior. At temperatures above T_{c} critical speeding up has been observed. While this was previously reported from measurements of the magnetic ac susceptibility the limited frequency range available for this method prevented measurements at the critical field where the resonance frequency of the observed relaxation is well above 1 kHz. The dynamical critical exponent at the critical field was found to be of the order of -0.7.

While the cause of the speeding up is not established, a possible explanation is coherent movement of the magnetic monopoles close to the critical field. In this case the damping Γ is reduced as the monopole-monopole scattering vanishes and the resonance frequency of the relaxation, $\omega_{\mathrm{R}} = \omega_0^2/\Gamma$, increases.

Taking the water analogy of spin-ice one step further, a second possible explanation is the piston effect. This effect explains the critical speeding up in the thermalization of a gas close to its critical endpoint in zero gravity by an adiabatic process that dominates the thermalization if the compressibility is very high and c_P diverges. In the case of spin-ice the magnetic field plays the role of pressure and the magnetic susceptibility, that diverges at the critical field, corresponds to the specific heat c_P.

Finally, it was shown that the magnetoelectric coupling in $Dy_2Ti_2O_7$ is of $< PPMM >$ type as is evident from the good qualitative agreement between the magnetic and dielectric results.

6 $Y_2Ti_2O_7$

In this chapter the dielectric properties of the non-magnetic compound $Y_2Ti_2O_7$ are discussed. As expected they are independet of the applied magnetic field even at temperatures well below 1 K.

Contents

6.1 Introduction

The non-magnetic compound $Y_2Ti_2O_7$ is not only interesting as an isostructural reference compound for the spin-ice $Dy_2Ti_2O_7$, but interesting for dielectric studies on its own right. Its cubic pyrochlore structure $Fd\bar{3}m$ is isostructural with $Dy_2Ti_2O_7$ and has a lattice constant of about $a = 10.17\,\text{Å}$ [37]. As a member of the titanates $Y_2Ti_2O_7$ is a candidate for quantum paraelectric behavior similar to the famous example $SrTiO_3$. Due to the lack of magnetic ions no influence of the magnetic field is expected.

6.1.1 Sample preparation

For this measurements a disk-shaped $Y_2Ti_2O_7$ sample (JF0115a) with orientation perpendicular to the [111] direction was used. The dimensions of this sample were 3.6 by 5.5 mm with a thickness of 0.74 mm. Onto this sample gold contacts with an area of $7.9\,\text{mm}^2$ were applied that serve as capacitor plates. Due to the orientation on the sample holder both electric and magnetic fields are oriented in [111] direction.

6.2 Temperature-dependent permittivity

To characterize the nature of $Y_2Ti_2O_7$ the permittivity was measured in a wide range of temperatures. The results for the real part ε' are shown in figure 6.1.

Most obvious is the natural stacking of the curves, meaning that the absolute value of ε' increases with decreasing temperature.

The second prominent feature is visible at high temperatures (red): here a step is observed that moves from roughly 1 kHz towards lower frequencies with decreasing temperature. Figure 6.2 shows this relaxation process in detail for four selected temperatures and also gives the corresponding data on the dielectric loss. The latter shows a peak that follows the position of the step in the permittivity towards lower frequencies. Both real and imaginary part can be described in reasonable

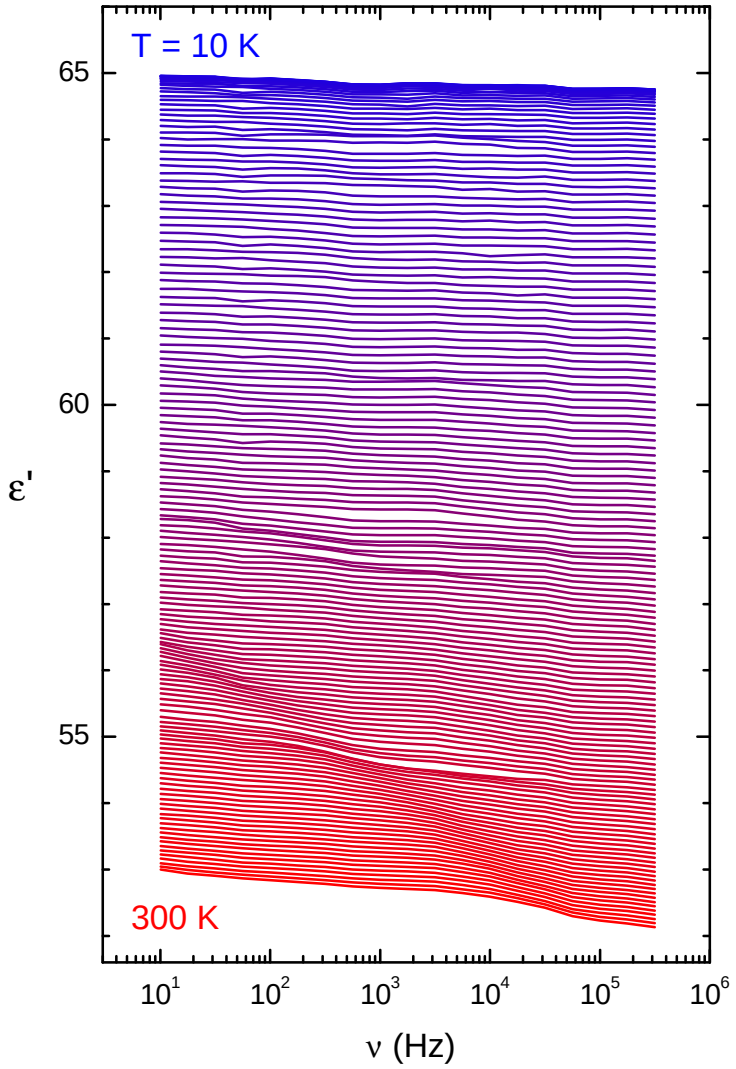

Figure 6.1: High-temperature permittivity.
Frequency sweeps of the permittivity of $Y_2Ti_2O_7$ for various temperatures between 300 and 10 K. Due to the strong temperature dependence no artificial stacking of the curves was used. At high temperatures (red) the shift of a step caused by contact effects through the frequency domain towards lower frequencies is observed, otherwise only a linear slope caused by the materials nearly constant loss is visible.

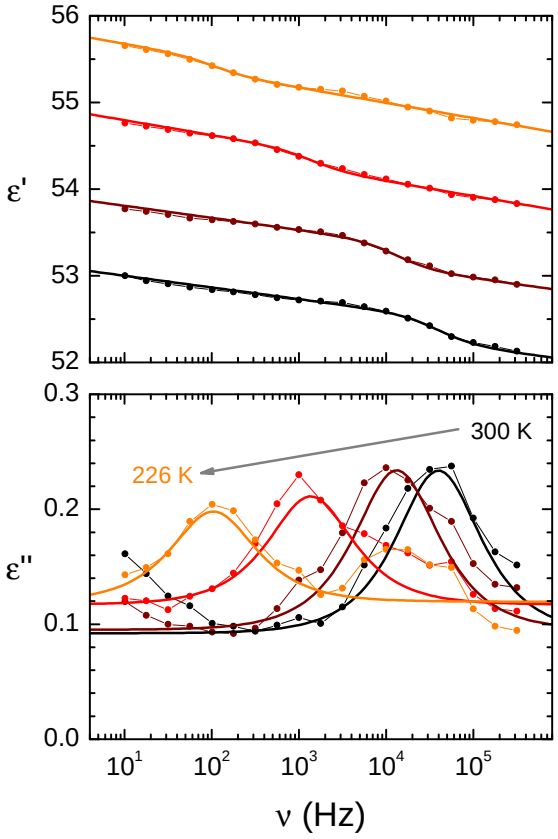

Figure 6.2: High-temperature relaxation.
The high-temperature relaxation in $Y_2Ti_2O_7$ can be described reasonably well with a single Debye relaxation and a constant loss contribution (solid lines). With decreasing temperature both the peak position $1/\tau$ and its area $\Delta\varepsilon$ are reduced until they vanish at roughly 200 K.

agreement by a single Debye relaxation with constant loss contribution (solid lines). Using the temperature-dependent peak positions ν_p and the Arrhenius equation the activation energy for this relaxation process is fitted as $U_\mathrm{b}/k_\mathrm{B} = 2410(130)\,\mathrm{K}$.

This temperature-dependent relaxation process is typical for contact effects that can be either extrinsic, *e.g.* caused by the contact between the metal capacitor plates applied onto the insulating sample, or intrinsic and caused for example by charges located at grain boundaries.

Finally, figure 6.1 also reveals a linear slope in the permittivity that is associated with nearly constant loss that will be discussed in the following section.

6.2.1 Quantum paraelectric behavior

As discussed in chapter 1.6 quantum paraelectric materials are known to show several characteristic properties. In the following sections two of those, the description of the permittivity using the Barrett formula and the nearly constant loss behavior, will be evaluated.

Barrett formula

For a detailed examination of the temperature dependence of the permittivity figure 6.3 shows the temperature dependence for 10 frequencies from 10 Hz to 316 kHz. In the $\log_{10}(T)$ scale used in the main plot the saturation at temperatures below 10 K becomes obvious while the deviation of the lower frequencies above

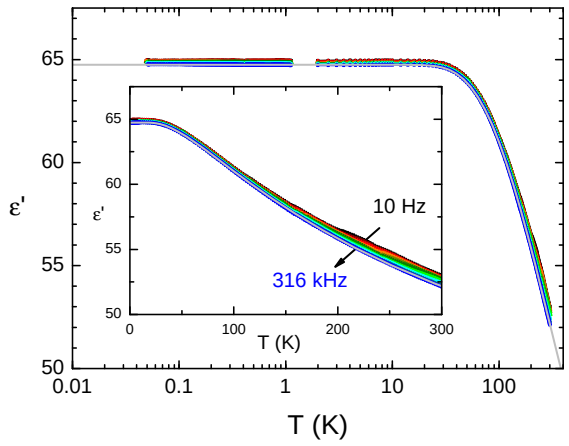

Figure 6.3:
Fit of the Barrett formula.
Temperature-dependent permittivity of $Y_2Ti_2O_7$ for frequencies between 10 Hz and 316 kHz. The gray curve is a fit of the Barrett formula, equation (1.21), to the curve measured at 316 kHz and gives a very good description of the temperature dependence.

100 K are illustrated in the linear plot in the inset.

The fit of the Barrett formula, equation (1.21) on page 13, shown in gray (—) was done for the highest frequency as this curve is not influenced by the relaxation above 100 K and is indeed an excellent description for the temperature dependence of the permittivity. As it is not possible to separate n and μ from this fit the results are given as the product $nk_B\mu^2 = 10\,400(100)\,\mathrm{K}$, $J_0/k_B = -1093(9)\,\mathrm{K}$, $\Omega/k_B = 134.4(5)\,\mathrm{K}$, and $\varepsilon_\infty = 33.2(10)$.

Opposed to the previously discussed $Dy_2Ti_2O_7$ here the description of the permittivity is very good down to the lowest temperatures.

Nearly constant loss

As shown in equation (1.29) on page 15 a nearly constant loss is not only observed in the dielectric loss, but also directly related to a frequency-dependent reduction of the permittivity that is proportional to $\log(\nu)$. This behavior in the permittivity was already seen in figure 6.1 and is shown in figure 6.4 in more detail for measurements at 800 mK that are free of additional contributions. The red curves are plotted from equation (1.29) with $\varepsilon_{\mathrm{c.l.}} = 0.025$ and a constant offset of 67.7 in the real part and provide a good description of the frequency dependence observed in both real and imaginary part of the permittivity.

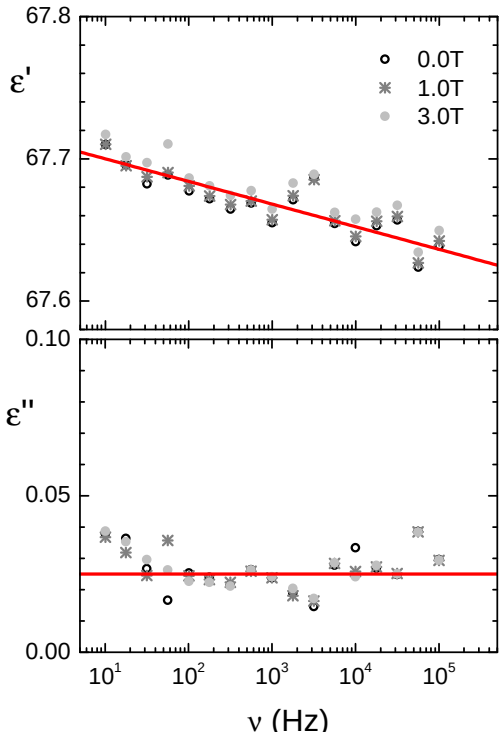

Figure 6.4:
Low-temperature nearly constant loss.
At 0.8 K the nearly constant loss in $Y_2Ti_2O_7$ can be observed. Here also the non-existent magnetic field dependence can be seen as the measurements for fields up to 3 T are identical.

6.3 Conclusion

It could be shown that $Y_2Ti_2O_7$ is a quantum paraelectric material that has the typical properties associated with this type of materials. A relaxation process observed at high temperatures was attributed to contact effects and its temperature activated behavior was modeled with Debye relaxation. The increasing permittivity with decreasing temperature could be described with the Barrett formula and the remaining frequency dependence in ε' could be explained purely by a nearly constant loss contribution.

At very low temperature the magnetic field dependence of the permittivity was examined and its expected lack thereof was confirmed. While this observation itself as unsurprising it was an important part of the reasoning that electric dipoles exist on magnetic monopoles in the previous chapter.

Summary

In the course of this work a setup for two-wire frequency-dependent impedance spectroscopy has been successfully implemented in a top-loading dilution refrigerator. With this setup it is possible to carry out measurements at stable temperatures in the range of 0.025 to 1.2 K and in magnetic fields of up to 13 T. During the construction of the sample platform the easy change of sample holders and interoperability with the setup for higher temperatures in the PPMS was also considered important. This technical goals could be achieved and it is now possible to do measurements with frequencies up to 5 GHz down to lowest temperatures.

Subsequently measurements have been performed at different materials that were presented in chapters 3 - 6:

$TbMnO_3$

Using impedance spectroscopy it was demonstrated that the polaronic nature of the *c*-axis relaxation in $TbMnO_3$ has a strong influence on the switchable polarization at the ferroelectric phase transition. Due to the relaxations distinct temperature dependence the separation of its contributions from that of the ferroelectric fluctuations above and domains below T_c is difficult. With magnetic field-dependent measurements it could be shown that the transition from the paraelectric to the ferroelectric phase can also be driven with the magnetic field while the underlying *c*-axis relaxation is almost independent of the magnetic field. When comparing the switchable polarization far above and below the critical field H_c it was shown that in the ferroelectric phase a small additional contribution to the switchable polarization exists that is observed only for low frequencies.

From high frequency data, 500 kHz to 1 GHz, the evaluation of the dynamical properties of the phase transition was attempted. Here the background was much smaller as the *c*-axis relaxation and contributions of the domains are suppressed in this frequency regime. From the evolution of the relaxation time of fluctuations in the paraelectric phase a critical exponent of $\gamma_{\nu_p} = 0.8(2)$ was extracted. Together with the observation of a 'dispersion' minimum in ε' this critical slowing down at the phase transition is in agreement with the behavior of classical ferroelectric materials. The evaluation of the relaxation strength $\Delta\varepsilon$ lead to a critical exponent $\gamma_{\Delta\varepsilon} \gtrsim 1$ where the choice of the offset for the correction has a significant influence.

The observation of the same critical exponent both for temperature- and magnetic-field-dependent measurements illustrates that in the case of $TbMnO_3$ the slowing down of an electromagnon is observed, similar to the reported behavior in other mangetoelectric materials, *e.g.* the multiferroic $MnWO_4$ [63].

$LiCuVO_4$

For the second material presented in this thesis, $LiCuVO_4$, the low-temperature setup was used to demonstrate the dependence of the polarization on the orientation of both magnetic and electric fields. In this material a planar spin-spiral phase exists at temperatures below 2.3 K that possesses polarization due to the

inverse Dzyaloshinskii-Moriya effect. With magnetic field the spiral spin order can be suppressed in favor of a modulated collinear phase without polarization. The starting point for the measurements was the idea that at very low temperatures close to the critical field quantum fluctuations might cause a change in the fluctuations dynamics.

Therefore, the polarization dynamics of the sample was examined with measurements of $P(E)$ hysteresis loops, the complex impedance at low and high electric fields. With these measurements it could be shown that the magnitude of the saturation polarization depends on the direction of the electric field where $P_{\mathrm{sat}}(H \parallel [001]) > P_{\mathrm{sat}}(H \parallel [100])$. Of special significance were high-frequency measurements of the magnetic field dependent permittivity and dielectric loss where a change in the nature of the observed processes could be observed at temperatures below 0.4 K. Here the previously observed Debye-like process changes into an excitation with a very low energy gap of 12.4 µeV. This observation of a very small gap is in agreement with theoretical predictions of a nearly gapless dielectric response from chiral solitons in $LiCuVO_4$ and here their first experimentally observation is reported.

$Dy_2Ti_2O_7$ and $Y_2Ti_2O_7$

For the spin-ice compound $Dy_2Ti_2O_7$ and its isostructural non-magnetic sister compound $Y_2Ti_2O_7$ measurements of the permittivity from 300 K down to lowest temperatures were performed in the presence of a magnetic field in [111] direction. With magnetic fields of this orientation the phase diagram of the compound has a strong similarity with water ice including a critical endpoint of the so called monopole liquid-to-gas transition. At high temperatures the quantum paraelectric nature of both compounds was demonstrated. This stems from the TiO_6 octahedrons and causes a characteristic increase of ε' towards lower temperatures as well as a nearly constant loss contribution that causes a frequency dependence of the permittivity.

From a comparison of the magnetic ac susceptibility with the complex permittivity and by comparing the magnetic field dependence of the latter for $Dy_2Ti_2O_7$ and the non-magnetic $Y_2Ti_2O_7$ it could be demonstrated that magnetic monopoles carry electric dipoles. Furthermore, magnetic-field- and frequency-dependent measurements of the permittivity were used to demonstrate critical speeding-up of the dipole dynamics at and above the critical endpoint. In this case the available broad frequency range for the dielectric measurements enabled the evaluation of this anomalous dynamics much closer to the critical field as it could previously be done with magnetic ac susceptibility.

While the exact cause of the critical speeding-up is not understood, a possible mechanism is coherent movement of the magnetic monopoles close to the critical point. In this case the monopole-monopole scattering vanishes, thereby reducing the damping Γ of the relaxation process of their movement and increasing the resonance frequency $\omega_{\mathrm{r}} = \omega_0^2/\Gamma$. Also the piston effect—a critical speeding-up of the equilibration in a fluid close to its liquid-vapor critical point—seems to be an interesting starting point to understand the observed dynamics in spin-ice as its analogy to water has often been emphasized in literature.

For all magnetoelectric compounds examined in the course of this thesis the broadband approach possible with dielectric spectroscopy could be used to gain

a deeper understanding of the dynamics of the complex order parameter. The accessibility of higher frequencies compared to magnetic ac susceptibility measurements that are typically limited to the kHz regime enables a more detailed observation of fluctuation dynamics while suppressing the influence of domains and other unwanted effects.

Outlook

For the future the observation of other magnetoelectric materials is interesting and from the results presented here the focus should be on systems that show phase transitions or critical points at very low temperatures. This could be either other spin-½ spin chains similar to $LiCuVO_4$ where the existence of the soliton excitation could be revisited. One possible compound being $LiCu_2O_2$ where the ferroelectric to paraelectric transition at low temperatures is expected at about 12 T and is still in the accessible field range of the low temperature setup. On the other hand it is an interesting question whether the observed critical speeding-up in $Dy_2Ti_2O_7$ also exists in other spin-ice compounds like $Ho_2Ti_2O_7$. Additionally, measurements on the quantum spin-ice compounds $Yb_2Ti_2O_7$ or $Pr_2Zr_2O_7$ should also yield insight into novel dynamical properties.

A Basics

A.1 Binomial coefficients

In the main text a sum of the type

$$\begin{aligned}\sum_{k=0}^{n}\binom{n}{k}\mathrm{e}^{-\mathrm{i}(n-2k)x} &= \binom{n}{0}\mathrm{e}^{-\mathrm{i}(n-0)x} + \binom{n}{1}\mathrm{e}^{-\mathrm{i}(n-2)x} + ...+ \\ &\quad + \binom{n}{n-1}\mathrm{e}^{-\mathrm{i}(n-2(n-1))x} + \binom{n}{n}\mathrm{e}^{-\mathrm{i}(n-2n)x} \\ &= \binom{n}{0}\mathrm{e}^{-\mathrm{i}nx} + \binom{n}{1}\mathrm{e}^{-\mathrm{i}(n-2)x} + ...+ \\ &\quad + \binom{n}{n-1}\mathrm{e}^{\mathrm{i}(n-2)x} + \binom{n}{n}\mathrm{e}^{\mathrm{i}nx}\end{aligned}$$

for $n > 0 \in \mathbb{N}$ has been discussed. Due to the symmetry of the binomial coefficients, $\binom{n}{k} = \binom{n}{n-k}$, this can be shortened to

$$\sum_{k=0}^{n}\binom{n}{k}\mathrm{e}^{-\mathrm{i}(n-2k)x} = \binom{n}{0}(\mathrm{e}^{-\mathrm{i}nx} + e^{\mathrm{i}nx}) + \binom{n}{1}(\mathrm{e}^{-\mathrm{i}(n-2)x} + \mathrm{e}^{-\mathrm{i}(n-2)x}) + ...$$

Now $\mathrm{e}^{-\mathrm{i}nx} + \mathrm{e}^{\mathrm{i}nx}$ can be expressed as $2\cos(nx)$ or, when staying in the complex notation is desired, $2 \cdot \mathrm{Re}[\mathrm{e}^{-\mathrm{i}nx}]$. Note that some elements of the sum are missing where this is not true, namely $k = n/2$ for all even n. This elements are special because here the exponential function is 1 as its argument $(n-2k)$ is zero. Therefore, an additional sum over these elements has to be added:

$$E_{\mathrm{even}} = \sum_{j=1}^{\infty}\binom{n}{n/2}.$$

Combining these results the sum can be rewritten as

$$\begin{aligned}\sum_{k=0}^{n}\binom{n}{k}\mathrm{e}^{-\mathrm{i}(n-2k)x} &= \mathrm{Re}\left[2\binom{n}{0}\mathrm{e}^{-\mathrm{i}nx} + 2\binom{n}{1}\mathrm{e}^{-\mathrm{i}(n-2)x} + ...\right] + E_{\mathrm{even}} \\ &= \mathrm{Re}\left[\sum_{k=0}^{<n/2} 2\binom{n}{k}\mathrm{e}^{-\mathrm{i}(n-2k)x}\right] + E_{\mathrm{even}}. \qquad \text{(A.1)}\end{aligned}$$

A.2 Temperature-dependent dielectric spectra

The derivative of the imaginary part of equation (1.19) is found by using the reciprocal rule:

$$\varepsilon''(\omega,T) = -\frac{\Delta\varepsilon\omega\tau_0 \mathrm{e}^{\frac{U_\mathrm{b}}{k_\mathrm{B}T}}}{1+\omega^2\tau_0^2\mathrm{e}^{\frac{2U_\mathrm{b}}{k_\mathrm{B}T}}}$$

$$\frac{\mathrm{d}}{\mathrm{d}T}\varepsilon''(\omega,T) = -\frac{\Delta\varepsilon\tau_0\omega U_\mathrm{b}\mathrm{e}^{\frac{U_\mathrm{b}}{k_\mathrm{B}T}}\left(\tau_0^2\omega^2\mathrm{e}^{\frac{2U_\mathrm{b}}{k_\mathrm{B}T}}-1\right)}{k_\mathrm{B}\left(\tau_0^2\omega^2T\mathrm{e}^{\frac{U_\mathrm{b}}{k_\mathrm{B}T}}+T\right)} \tag{A.2}$$

To find the maximum the zero of the derivative with respect to the temperature T has to be found. This is relatively simple because all variables used are positive real numbers and the zero can be identified by solving

$$\tau_0^2\omega^2\mathrm{e}^{\frac{2U_\mathrm{b}}{k_\mathrm{B}T_\mathrm{max}}}-1=0$$

for T_max:

$$T_\mathrm{max} = -\frac{U_\mathrm{b}}{k_\mathrm{B}}\cdot\frac{1}{\log\left(\tau_0\omega\right)} \tag{A.3}$$

As long as $\tau_0\omega < 1$, as is typically the case for highly damped relaxation processes, there is always a maximum in the imaginary part at a finite, positive temperature T_max.

B Experimental minutiae

B.1 The Open-Short-Load calibration in detail

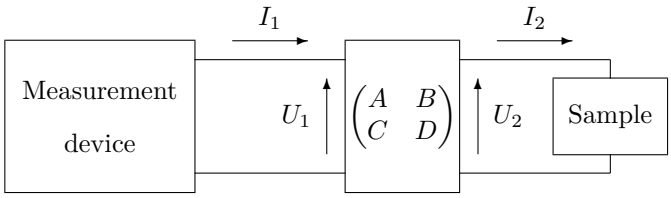

Figure B.1: Four terminal network for the Open-Short-Load calibration.

The mathematical idea for the Open-Short-Load calibration is the transformation of two vectors by matrix multiplication. Using the general approach shown in figure B.1 the probe is represented by an unknown four terminal circuit. This model can be expressed by the equation

$$\begin{pmatrix} U_1 \\ I_1 \end{pmatrix} = \begin{pmatrix} A & B \\ C & D \end{pmatrix} \begin{pmatrix} U_2 \\ I_2 \end{pmatrix}$$

From this equation the relationships between the currents and amplitudes follow as

$$\begin{aligned} U_1 &= AU_2 + BI_2 \\ I_1 &= CU_2 + DI_2 \end{aligned} \tag{B.1}$$

The true impedance $Z = U_2/I_2$ of the sample is related to the measured impedance Z_M by

$$Z_\mathrm{M} = \frac{U_1}{I_1} = \frac{AU_2 + BI_2}{CU_2 + DI_2} = \frac{A \cdot \dfrac{U_2}{I_2} + B}{C \cdot \dfrac{U_2}{I_2} + D} = \frac{AZ + B}{CZ + D} \tag{B.2}$$

While knowing the actual matrix elements might be of theoretical interest, for the application directly measured values are preferable. Therefore, three standard elements are used: Open, Short, and Load.

Open

For the Open standard a measurement of the empty sample holder is performed. Due to the nonexistent electrical connection between both connectors the current I_2 is zero. Than equation (B.2) is reduced to

$$Z_{\mathrm{O}} = \frac{AU_2}{CU_2} = \frac{A}{C}. \tag{B.3}$$

C can now be replaced by A/Z_{O} using the measured impedance Z_{O} of the Open.

Short

The Short measurement uses a shorted out sample holder with no potential difference: $U_2 = 0$. Equation (B.2) now is reduced to

$$Z_{\mathrm{S}} = \frac{BI_2}{DI_2} = \frac{B}{D}. \tag{B.4}$$

The measured impedance Z_{S} of the Short can now be used to replace B by DZ_{S}.

Load

Finding the last two matrix elements A and D requires a slightly more complex standard, the Load. The Load is obtained by mounting a frequency-independent resistor with resistivity $Z_{\mathrm{DCL}} = U_2'/I_2'$ on the sample holder. Using this constriction we get another set of equations similar to equation (B.2):

$$Z_{\mathrm{L}} = \frac{AU_2' + BI_2'}{CU_2' + DI_2'} = \frac{A \cdot \dfrac{U_2'}{I_2'} + B}{C \cdot \dfrac{U_2'}{I_2'} + D} = \frac{AZ_{\mathrm{DCL}} + B}{CZ_{\mathrm{DCL}} + D}$$

With equations (B.3) and (B.4) from the previous standards we can replace B and C:

$$Z_{\mathrm{L}} = \frac{AZ_{\mathrm{DCL}} + DZ_{\mathrm{S}}}{\dfrac{A}{Z_{\mathrm{O}}} \cdot Z_{\mathrm{DCL}} + D} = \frac{AZ_{\mathrm{DCL}} + DZ_{\mathrm{S}}}{AZ_{\mathrm{DCL}} + DZ_{\mathrm{O}}} \cdot Z_{\mathrm{O}}$$

This equation is solved for D:

$$\begin{aligned} Z_{\mathrm{L}}(AZ_{\mathrm{DCL}} + DZ_{\mathrm{O}}) &= (AZ_{\mathrm{DCL}} + DZ_{\mathrm{S}})Z_{\mathrm{O}} \\ D(Z_{\mathrm{O}}Z_{\mathrm{L}} - Z_{\mathrm{S}}Z_{\mathrm{O}}) &= A(Z_{\mathrm{DCL}}Z_{\mathrm{O}} - Z_{\mathrm{DCL}}Z_{\mathrm{L}}) \\ D &= A \cdot \frac{Z_{\mathrm{DCL}}Z_{\mathrm{O}} - Z_{\mathrm{DCL}}Z_{\mathrm{L}}}{Z_{\mathrm{O}}Z_{\mathrm{L}} - Z_{\mathrm{S}}Z_{\mathrm{O}}} \end{aligned} \tag{B.5}$$

Formula for the OSL-correction

Starting from equation (B.2) that contains all four error terminals we use equations (B.3), (B.4), and (B.5) to replace them with the measurements of the standards:

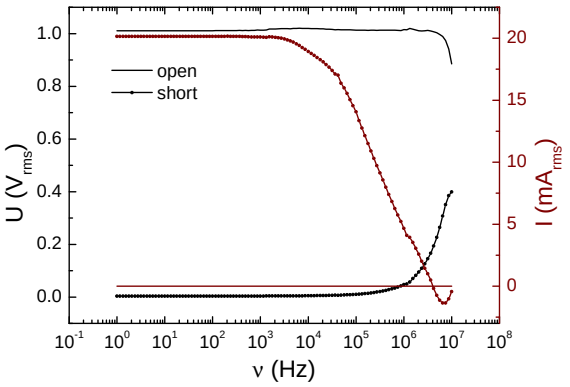

Figure B.2:
Frequency dependence of the open and short standards.
The open (line) is relatively close to the assumption $I_{\text{short}} = 0$. In contrast the assumption of vanishing voltage for the short (dots) is clearly not valid at frequencies above roughly 100 kHz.

$$
\begin{aligned}
Z_{\mathrm{M}} &= \frac{AZ+B}{CZ+D} = \frac{AZ+DZ_{\mathrm{S}}}{AZ+DZ_{\mathrm{O}}} \cdot Z_{\mathrm{O}} \\
&= \frac{AZ + A \cdot \dfrac{Z_{\mathrm{DCL}}Z_{\mathrm{O}} - Z_{\mathrm{DCL}}Z_{\mathrm{L}}}{Z_{\mathrm{O}}Z_{\mathrm{L}} - Z_{\mathrm{S}}Z_{\mathrm{O}}} \cdot Z_{\mathrm{S}}}{AZ + A \cdot \dfrac{Z_{\mathrm{DCL}}Z_{\mathrm{O}} - Z_{\mathrm{DCL}}Z_{\mathrm{L}}}{Z_{\mathrm{O}}Z_{\mathrm{L}} - Z_{\mathrm{S}}Z_{\mathrm{O}}} \cdot Z_{\mathrm{O}}} \cdot Z_{\mathrm{O}} \\
&= \frac{ZZ_{\mathrm{O}}(Z_{\mathrm{L}} - Z_{\mathrm{S}}) + (Z_{\mathrm{O}} - Z_{\mathrm{L}})Z_{\mathrm{DCL}}Z_{\mathrm{S}}}{Z(Z_{\mathrm{L}} - Z_{\mathrm{S}}) + (Z_{\mathrm{O}} - Z_{\mathrm{L}})Z_{\mathrm{DCL}}}
\end{aligned}
$$

Solving this equation for Z yields

$$
Z(\nu) = \frac{Z_{\mathrm{S}}(\nu) - Z_{\mathrm{M}}(\nu)}{Z_{\mathrm{M}}(\nu) - Z_{\mathrm{O}}(\nu)} \cdot \frac{Z_{\mathrm{L}}(\nu) - Z_{\mathrm{O}}(\nu)}{Z_{\mathrm{S}}(\nu) - Z_{\mathrm{L}}(\nu)} \cdot Z_{\mathrm{DCL}} \tag{B.6}
$$

Z	:	true impedance of the sample
Z_{M}	:	uncorrected measurement of the sample
Z_{O}	:	measured value for the Open
Z_{S}	:	measured value for the Short
Z_{L}	:	measured value for the Load
Z_{DCL}	:	DC resistivity of the Load

In practice the production of calibration standards that satisfy the assumptions made in the previous considerations is rather difficult. A frequency-dependent load can easily be compensated for by replacing the constant impedance Z_{DCL} by a frequency-dependent $Z_{\mathrm{DCL}}(\nu)$ that is obtained from either measurements or a simulation of the equivalent circuit. For open and short the implementation of frequency-dependent standards is more complicated. The necessity for this is demonstrated in figure B.2 that shows the frequency-dependent current and voltage of the open and short standards as they were measured when connected directly to the impedance analyzer.
While the open exhibits an almost negligible frequency dependence up to highest frequencies the deviation of the short from the ideal behavior starting at 1 kHz are very pronounced. Therefore, the simple model will be expanded to generalized calibration standards in the following.

B.2 Generalized calibration method

Using the same approach as before the error terms A, B, C,and D can also be found using three arbitrary electrical devices as long as their frequency-dependent impedance is known.

Again, three calibration measurements (Z_{1m},Z_{2m}, and Z_{3m}) are required but no further assumptions for their qualities are made except that their frequency-dependent impedance (Z_1,Z_2, and Z_3) in known.

The starting point of the calculations is equation (B.2) solved for B:

$$B = Z_{1m}(C \cdot Z_1 + D) - A \cdot Z_1. \tag{B.7}$$

The second standard is used to find an expression of A that depends only on C and D.

$$\begin{aligned} A &= -\frac{B}{Z_2} + C \cdot Z_{2m} + D\frac{Z_{2m}}{Z_2} \\ &= -\frac{Z_{1m}(C \cdot Z_1 + D) - A \cdot Z_1}{Z_2} + C \cdot Z_{2m} + D\frac{Z_{2m}}{Z_2} \\ A &= \frac{Z_{2m}Z_2 - Z_{1m}Z_1}{Z_2 - Z_1} \cdot C + \frac{Z_{2m} - Z_{1m}}{Z_2 - Z_1} \cdot D \end{aligned} \tag{B.8}$$

Using the last calibration measurements in combination with equations (B.7) and (B.8) lead to an expression that connects C and D.

$$\begin{aligned} D &= \frac{A \cdot Z_3 + B}{Z_{3m}} - C \cdot Z_3 \\ &= -\frac{Z_{2m}(Z_3 - Z_1)Z_2 + Z_{1m}(Z_2 - Z_3)Z_1 + Z_{3m}(Z_1 - Z_2)Z_3}{Z_{2m}(Z_3 - Z_1) + Z_{1m}(Z_2 - Z_3) + Z_{3m}(Z_1 - Z_2)} \cdot C \\ &= X \cdot C \end{aligned} \tag{B.9}$$

For convenience the fraction is termed X in the following.

The last step is taken by using equation (B.2) for an actual measured sample with impedance Z and measured impedance Z_m. Applying all previous results and solving the equation for Z leads to the final formula for the measurement correction:

$$Z = \frac{Z_1\,(Z_{1m} - Z_{2m})\,(Z_2 + X) + X\,(Z_2 - Z_1)\,(Z_{1m} - Z_m)}{Z_m\,(Z_2 - Z_1) + Z_{1m}\,(Z_1 + X) - Z_{2m}\,(Z_2 + X)} \tag{B.10}$$

Compared to equation (B.6) this result is much more complex and requires the input of six measurements to correct unwanted effects. A further disadvantage is the requirement of precise impedance information for all reference elements used.

If, on the other hand, the measurement device itself is considered to produce reliable results this calibration method is very well suited to remove unwanted additional contributions due to for example the coaxial cables used in the probe. Here the the reference elements are measured first directly with the measurement device with as little coaxial cables as possible giving Z_1, Z_2, and Z_3. In the next step the probe with the references is measured resulting in Z_{1m}, Z_{2m}, and Z_{3m}. Inserting this results in equations (B.9) and (B.10) will now remove the contribution of the probe from all further measurements.

Therefore, in a technical sense this approach is not truly a calibration but should be considered in terms of de-embedding where the influence of the probe on the measurement can be reduced without curing any errors that are caused by the instrument itself.

B.3 Mathematica script for the demagnetization correction

Solving the geometrical demagnetization for a thin slab of material analytically is not possible. Therefore, the Maxwell equations have to solved locally and the demagnetization can be determined by the volume average over the material between the capacitor plates on the sample.

For the calculations the shape of the sample is approximated as a rectangular slab of length a, width b, and thickness c. The magnetic field is assumed to be parallel to the c-axis of the sample and magnetization data for the corresponding crystallographic axis has to be available. The capacitor plates are assumed to be rectangular and centered in the ab-plane. Their size is used to define the volume for averaging.

Using this simplifications of the sample geometry the following script can be used for the calculation with Mathematica 7 and the Radia package[1] from the ESRF. The variables that have to be adjusted are:

VUnit	:	size of the unit cell of the material in m^3
NrIons	:	number of magnetic ions per unit cell
a	:	sample length in a direction
b	:	sample width in b direction
c	:	sample height in c direction (parallel to H)
aContact	:	length of the capacitor plates in a direction
bContact	:	width of the capacitor plates in b direction
maxfield	:	maximum magnetic field for the simulation
inputfile	:	file with the magnetization data
outputfile	:	output file for the paired values of B and $\mu_0 H$

All dimensions should be given in mm and the maximum magnetic field value is expected in Tesla.

[1] O. Chubar, P. Elleaume, J. Chavanne "Radia" (1997)
http://www.esrf.eu/Accelerators/Groups/InsertionDevices/Software/Radia

```
<< Radia`;
\[Mu]B = 9.2740154*10^(-24);
\[Mu]0 = 4 \[Pi] 10^(-7);

VUnit = ;
NrIons = ;
a = ;
b = ;
c = ;
aContact = ;
bContact = ;
maxfield = ;
inputfile = "";
outputfile = "";

radUtiDelAll[];
ConvertToT[{x_, y_}] := {x, y \[Mu]B \[Mu]0 NrIons/VUnit };
MvsHMeas = Map[ConvertToT, MovingAverage[Import[inputfile,
               "Table"], 10]];

HExt = {0, 0, 1.5};

HReduced[x_, y_, z_, HExt_] :=
  Module[
    {magneticfield, material, sample, problem, InteractMatrix},
    magneticfield = radObjBckg[HExt];
    material = radMatSatIso[MvsHMeas];
    sample = radObjRecMag[{0, 0, 0}, {a, b, c}];
    radMatApl[sample, material];
    problem = radObjCnt[{sample, magneticfield}];
    InteractMatrix = radRlxPre[problem];
    radRlxAuto[InteractMatrix, 0.0000001, 200, 4];
    Norm[radFld[problem, "hxhyhz", {x, y, z}]]
  ];

HReducedMeanSample[HExt_] :=
  Integrate[
    HReduced[xi, yi, zi, HExt], {xi, -aContact/2,
     aContact/2}, {yi, -bContact/2, bContact/2}, {zi, - c/2,
     c/2}]/(aContact bContact c);

Plot[HReducedMeanSample[{0, 0, h}], {h, 0, maxfield}]

DataTable = Table[{h, HReducedMeanSample[{0, 0, h}]}, {h, 0,
                  maxfield, 0.01}];

Export[outputfile, DataTable];
```

C $LiCuVO_4$

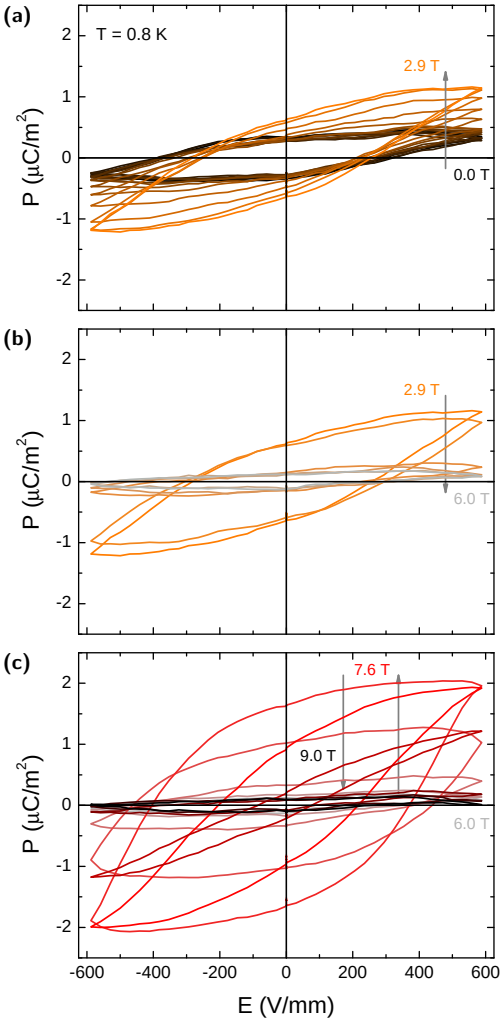

Figure C.1:
$\boldsymbol{H} \parallel [100]$: $\boldsymbol{P(E)}$ at 0.8 K.
Measurements of the $P(E)$ curves of $LiCuVO_4$ at 0.8 K. The different phase transitions can be seen in the opening of the hysteresis loops as the coercive field is reduced in the proximity of the phase transition and more polarization can be switched with the applied electric field.

Bibliography

[1] A. Aharoni. "Demagnetizing factors for rectangular ferromagnetic prisms". In: *J. Appl. Phys.* 83.6 (1998), pp. 3432–3434. DOI: 10.1063/1.367113.

[2] H. Aoki, T. Sakakibara, K. Matsuhira, and Z. Hiroi. "Magnetocaloric Effect Study on the Pyrochlore Spin Ice Compound $Dy_2Ti_2O_7$ in a [111] Magnetic Field". In: *Journal of the Physical Society of Japan* 73.10 (2004), pp. 2851–2856. DOI: 10.1143/JPSJ.73.2851.

[3] J. H. Barrett. "Dielectric Constant in Perovskite Type Crystals". In: *Physical Review* 86.1 (1952), pp. 118–120. DOI: 10.1103/PhysRev.86.118.

[4] G. Blasse. "Antiferromagnetism of the spinel $LiCuVO_4$". In: *Journal of Physics and Chemistry of Solids* 27.3 (1966), pp. 612–613. DOI: 10.1016/0022-3697(66)90206-X.

[5] R. Blinc and B. Žekš. *Soft modes in ferroelectrics and antiferroelectrics*. North-Holland Pub. Co., 1974, p. 317.

[6] H. W. Bode. *Network analysis and feedback amplifier design*. D. van Nostrand Company, Inc., 1945, p. 577. ISBN: 0882752421.

[7] H. Boukari, J. N. Shaumeyer, M. E. Briggs, and R. W. Gammon. "Critical speeding up in pure fluids". In: *Physical Review A* 41.4 (1990), pp. 2260–2263. DOI: 10.1103/PhysRevA.41.2260.

[8] L. Bovo, J. A. Bloxsom, D. Prabhakaran, G. Aeppli, and S. T. Bramwell. "Brownian motion and quantum dynamics of magnetic monopoles in spin ice". In: *Nature communications* 4 (2013), p. 1535. DOI: 10.1038/ncomms2551.

[9] N. Büttgen et al. "Spin-modulated quasi-one-dimensional antiferromagnet $LiCuVO_4$". In: *Physical Review B* 76.1 (2007), pp. 1–11. DOI: 10.1103/PhysRevB.76.014440.

[10] C. Castelnovo, R. Moessner, and S. L. Sondhi. "Magnetic monopoles in spin ice". In: *Nature* 451.7174 (2008), pp. 42–45. DOI: 10.1038/nature06433.

[11] L. F. Chen, C. K. Ong, C. P. Neo, V. V. Varadan, and V. K. Varadan. *Microwave Electronics*. Chichester, UK: John Wiley & Sons, Ltd, 2004, pp. –470. ISBN: 9780470020463. DOI: 10.1002/0470020466.

[12] Y. Chen, H. Yuan, G. Li, G. Tian, and S. Feng. "Crystal growth and magnetic property of orthorhombic $RMnO_3$ (R=Sm-Ho) perovskites by mild hydrothermal synthesis". In: *Journal of Crystal Growth* 305 (2007), pp. 242–248. DOI: 10.1016/j.jcrysgro.2007.03.052.

[13] S.-W. Cheong and M. Mostovoy. "Multiferroics: a magnetic twist for ferroelectricity." In: *Nature materials* 6.1 (2007), pp. 13–20. DOI: 10.1038/nmat1804.

[14] D. Dahl and M. R. Moldover. "Thermal Relaxation near the Critical Point". In: *Physical Review A* 6.5 (1972), pp. 1915–1920. DOI: 10.1103/PhysRevA.6.1915.

[15] D. Dai, H. J. Koo, and M. H. Whangbo. "Investigation of the incommensurate and commensurate magnetic superstructures of $LiCuVO_4$ and CuO on the basis of the isotropic spin exchange and classical spin approximations". In: *Inorganic Chemistry* 43.13 (2004), pp. 4026–4035. DOI: 10.1021/ic035314c.

[16] Y. Deng, T. Garoni, and A. Sokal. "Critical Speeding-Up in the Local Dynamics of the Random-Cluster Model". In: *Physical Review Letters* 98.23 (2007), p. 230602. DOI: 10.1103/PhysRevLett.98.230602.

[17] P. a. M. Dirac. *Quantised Singularities in the Electromagnetic Field*. 1931. DOI: 10.1098/rspa.1931.0130.

[18] P. a. M. Dirac. "The theory of magnetic poles". In: *Physical Review* 74.7 (1948), pp. 817–830. DOI: 10.1103/PhysRev.74.817.

[19] S. Dunsiger et al. "Spin Ice: Magnetic Excitations without Monopole Signatures Using Muon Spin Rotation". In: *Physical Review Letters* 107.20 (2011), p. 207207. DOI: 10.1103/PhysRevLett.107.207207.

[20] I. Dzyaloshinsky. "A thermodynamic theory of "weak" ferromagnetism of antiferromagnetics". In: *Journal of Physics and Chemistry of Solids* 4.4 (1958), pp. 241–255. DOI: 10.1016/0022-3697(58)90076-3.

[21] M. Enderle et al. "Quantum helimagnetism of the frustrated spin-1/2 chain $LiCuVO_4$". In: *Europhysics Letters (EPL)* 70.2 (2005), pp. 237–243. DOI: 10.1209/epl/i2004-10484-x.

[22] M. Enderle et al. "Two-Spinon and Four-Spinon Continuum in a Frustrated Ferromagnetic Spin-1/2 Chain". In: *Physical Review Letters* 104.23 (2010), pp. 2–5. DOI: 10.1103/PhysRevLett.104.237207.

[23] S. Furukawa, M. Sato, and S. Onoda. "Chiral Order and Electromagnetic Dynamics in One-Dimensional Multiferroic Cuprates". In: *Physical Review Letters* 105.25 (2010), p. 257205. DOI: 10.1103/PhysRevLett.105.257205.

[24] S. Furukawa, M. Sato, S. Onoda, and A. Furusaki. "Ground-state phase diagram of a spin-1/2 frustrated ferromagnetic XXZ chain: Haldane dimer phase and gapped/gapless chiral phases". In: *Physical Review B* 86.9 (2012), p. 094417. DOI: 10.1103/PhysRevB.86.094417.

[25] S. Furukawa, M. Sato, Y. Saiga, and S. Onoda. "Quantum Fluctuations of Chirality in One-Dimensional Spin-1/2 Multiferroics: Gapless Dielectric Response from Phasons and Chiral Solitons". In: *Journal of the Physical Society of Japan* 77.12 (2008), p. 123712. DOI: 10.1143/JPSJ.77.123712.

[26] B. Gibson, R. K. Kremer, A. V. Prokofiev, W. Assmus, and G. J. McIntyre. "Incommensurate antiferromagnetic order in the quantum chain compound $LiCuVO_4$". In: *Physica B: Condensed Matter* 350.1-3 (2004), E253–E256. DOI: 10.1016/j.physb.2004.03.064.

[27] T. Goto, T. Kimura, G. Lawes, A. P. Ramirez, and Y. Tokura. "Ferroelectricity and Giant Magnetocapacitance in Perovskite Rare-Earth Manganites". In: *Physical Review Letters* 92.25 (2004), p. 257201. DOI: 10.1103/PhysRevLett.92.257201.

[28] R. Gross and A. Marx. *Festkörperphysik*. München: Oldenbourg Verlag, 2012. ISBN: 978-3-486-71294-0.

[29] M. J. Harris, S. T. Bramwell, D. F. Mcmorrow, T. Zeiske, and K. W. Godfrey. "Geometrical Frustration in the Ferromagnetic Pyrochlore $Ho_2Ti_2O_7$". In: *Physical Review Letters* 79.13 (1997), pp. 2554–7. DOI: 10.1103/PhysRevLett.79.2554.

[30] I. Hatta. "Experimental Study on Dielectric Relaxation in $NaNO_2$". In: *Journal of the Physical Society of Japan* 24.5 (1968), pp. 1043–1053. DOI: 10.1143/JPSJ.24.1043.

[31] S. Havriliak and S. Negami. "A complex plane analysis of α-dispersions in some polymer systems". In: *Journal of Polymer Science Part C: Polymer Symposia* 14.1 (1966), pp. 99–117. DOI: 10.1002/polc.5070140111.

[32] J. Hemberger. *Dielektrische Spektroskopie am Orientierungsglasübergang: lineares und nichtlineares Verhalten in Betain-Mischkristallen*. Aachen: Shaker Verlag, 1997. ISBN: 3826532015.

[33] J. Hemberger et al. "Multiferroic phases of $Eu_{1-x}Y_xMnO_3$". In: *Physical Review B* 75.3 (2007), p. 035118. DOI: 10.1103/PhysRevB.75.035118.

[34] J. Hemberger et al. "Quantum paraelectric and induced ferroelectric states in $SrTiO_3$". In: *Journal of Physics: Condensed Matter* 8 (1996), p. 4673.

[35] G. Hooft. *Magnetic monopoles in unified gauge theories*. 1974. DOI: 10.1016/0550-3213(74)90486-6.

[36] C. Itoi and S. Qin. "Strongly reduced gap in the zigzag spin chain with a ferromagnetic interchain coupling". In: *Physical Review B* 63.22 (2000), p. 224423. DOI: 10.1103/PhysRevB.63.224423.

[37] Y. Jiang, J. R. Smith, and G. Robert Odette. "Prediction of structural, electronic and elastic properties of $Y_2Ti_2O_7$ and Y_2TiO_5". In: *Acta Materialia* 58.5 (2010), pp. 1536–1543. DOI: 10.1016/j.actamat.2009.10.061.

[38] D. I. Khomskii. "Classifying multiferroics: Mechanisms and effects". In: *Physics* 2 (2009). DOI: 10.1103/Physics.2.20.

[39] D. I. Khomskii. "Electric dipoles on magnetic monopoles in spin ice". In: *Nature Communications* 3 (2012), pp. 1–13. DOI: 10.1038/ncomms1904.

[40] T. Kimura, G. Lawes, T. Goto, Y. Tokura, and A. P. Ramirez. "Magnetoelectric phase diagrams of orthorhombic RMnO$_3$ (R=Gd, Tb, and Dy)". In: *Physical Review B* 71.22 (2005), p. 224425. DOI: 10.1103/PhysRevB.71.224425.

[41] T. Kimura et al. "Distorted Perovskite with e_g^1 Configuration as a Frustrated Spin System". In: *Physical Review B* 68.060403 (2003). DOI: 10.1103/PhysRevB.68.060403.

[42] A. Klümper. "The spin-1/2 Heisenberg chain: thermodynamics, quantum criticality and spin-Peierls exponents". In: 685 (1998), pp. 677–685. DOI: 10.1007/s100510050491.

[43] A. Klümper and D. C. Johnston. "Thermodynamics of the Spin-1/2 Antiferromagnetic Uniform Heisenberg Chain". In: 3 (2000), p. 4. DOI: 10.1103/PhysRevLett.84.4701.

[44] G. Kolland. "Thermal Conductivity of the Spin-Ice Compound $Dy_2Ti_2O_7$ and the Spin-Chain System $BaCo_2V_2O_8$". PhD thesis. University of Cologne, 2013.

[45] H.-J. Koo, C. Lee, M.-H. Whangbo, G. J. McIntyre, and R. K. Kremer. "On the nature of the spin frustration in the CuO_2 ribbon chains of $LiCuVO_4$: crystal structure determination at 1.6 K, magnetic susceptibility analysis, and density functional evaluation of the spin exchange constants." In: *Inorganic chemistry* 50.8 (2011), pp. 3582–8. DOI: 10.1021/ic102518t.

[46] L. Kraus. "The demagnetization tensor of a cylinder". In: *Czechoslovak Journal of Physics* 23 (1973), pp. 512–519. DOI: 10.1007/BF01593828.

[47] F. Kremer and A. Schönhals. *Broadband Dielectric Spectroscopy*. Ed. by F. Kremer and A. Schönhals. Vol. null. null. Berlin, Heidelberg: Springer Berlin Heidelberg, 2003, p. 729. ISBN: 978-3-642-62809-2. DOI: 10.1007/978-3-642-56120-7.

[48] H.-A. Krug von Nidda et al. "Anisotropic exchange in $LiCuVO_4$ probed by ESR". In: *Physical Review B* 65.13 (2002), p. 134445. DOI: 10.1103/PhysRevB.65.134445.

[49] M. a. Lafontaine, M. Leblanc, and G. Ferey. "New refinement of the room-temperature structure of $LiCuVO_4$". In: *Acta Crystallographica Section C Crystal Structure Communications* 45.8 (1989), pp. 1205–1206. DOI: 10.1107/S0108270189001551.

[50] J. Liu, H.-J. Koo, H. Xiang, R. K. Kremer, and M.-H. Whangbo. "Most spin-1/2 transition-metal ions do have single ion anisotropy". In: *The Journal of Chemical Physics* 141.12 (2014), p. 124113. DOI: 10.1063/1.4896148.

[51] Y. Matiks, P. Horsch, R. K. Kremer, B. Keimer, and a. V. Boris. "Exciton Doublet in the Mott-Hubbard Insulator $LiCuVO_4$ Identified by Spectral Ellipsometry". In: *Physical Review Letters* 103.18 (2009), pp. 19–21. DOI: 10.1103/PhysRevLett.103.187401.

[52] K. Matsuhira et al. "Spin Dynamics at Very Low Temperature in Spin Ice $Dy_2Ti_2O_7$". In: *Journal of the Physical Society of Japan* 80.12 (2011), p. 123711. DOI: 10.1143/JPSJ.80.123711.

[53] M. J. Matthews et al. "High-temperature onset of field-induced transitions in the spin-ice compound $Dy_2Ti_2O_7$". In: *Physical Review B* 86.21 (2012), p. 214419. DOI: 10.1103/PhysRevB.86.214419.

[54] R. Moessner and S. L. Sondhi. "Theory of the [111] magnetization plateau in spin ice". In: *Physical Review B* 68.6 (2003), p. 064411. DOI: 10.1103/PhysRevB.68.064411.

[55] T. Moriya. "Anisotropic superexchange interaction and weak ferromagnetism". In: *Physical Review* 120.1 (1960), pp. 91–98. DOI: 10.1103/PhysRev.120.91.

[56] D. J. P. Morris et al. "Dirac strings and magnetic monopoles in the spin ice Dy2Ti2O7." In: *Science (New York, N.Y.)* 326.5951 (2009), pp. 411–414. DOI: 10.1126/science.1178868.

[57] M. Mourigal, M. Enderle, R. K. Kremer, J. Law, and B. Fåk. "Ferroelectricity from spin supercurrents in $LiCuVO_4$". In: *Physical Review B* 83.100409 (2011), pp. 1–4. DOI: 10.1103/PhysRevB.83.100409.

[58] K. A. Müller and H. Burkard. "$SrTiO_3$: An intrinsic quantum paraelectric below 4 K". In: *Physical Review B* 19.7 (1979), pp. 3593–3602. DOI: 10.1103/PhysRevB.19.3593.

[59] Y. Naito et al. "Ferroelectric Transition Induced by the Incommensurate Magnetic Ordering in $LiCuVO_4$". In: *Journal of the Physical Society of Japan* 76.2 (2007), p. 023708. DOI: 10.1143/JPSJ.76.023708.

[60] E. Nakamura, K. Deguchi, K. Shimakawa, and Y. Fujimoto. "Dielectric Dispersion in Ferroelectric $Ca_2Sr(C_2H_5CO_2)_6$". In: *Journal of the Physical Society of Japan* 52.1 (1983), pp. 288–294. DOI: 10.1143/JPSJ.52.288.

[61] E. Nakamura and M. Hosoya. "Dielectric Critical Slowing-Down in Ferroelectric $Ca_2Sr(C_2H_5CO_2)_6$". In: *Journal of the Physical Society of Japan* 23.4 (1967), pp. 844–847. DOI: 10.1143/JPSJ.23.844.

[62] A. M. Nicolson and G. F. Ross. "Measurement of the Intrinsic Properties of Materials by Time-Domain Techniques". In: *IEEE Transactions on Instrumentation and Measurement* 19.4 (1970), pp. 377–382. DOI: 10.1109/TIM.1970.4313932.

[63] D. Niermann et al. "Critical Slowing Down near the Multiferroic Phase Transition in $MnWO_4$". In: *Physical Review Letters* 114.January (2015), pp. 1–5. DOI: 10.1103/PhysRevLett.114.037204.

[64] D. Niermann et al. "Domain dynamics in the multiferroic phase of $MnWO_4$". In: *Physical Review B* 89.13 (2014), p. 134412. DOI: 10.1103/PhysRevB.89.134412.

[65] S. Nishimoto et al. "The strength of frustration and quantum fluctuations in $LiVCuO_4$". In: 37007 (2011), p. 7. DOI: 10.1209/0295-5075/98/37007.

[66] A. Onuki, H. Hao, and R. A. Ferrell. "Fast adiabatic equilibration in a single-component fluid near the liquid-vapor critical point". In: *Physical Review A* 41.4 (1990), pp. 2256–2259. DOI: 10.1103/PhysRevA.41.2256.

[67] J. Osborn. "Demagnetizing factors of the general ellipsoid". In: *Physical Review* 67.11-12 (1945), pp. 351–357. DOI: 10.1103/PhysRev.67.351.

[68] F. Pobell. *Matter and Methods at Low Temperatures*. Berlin, Heidelberg: Springer Berlin Heidelberg, 2007. ISBN: 978-3-540-46356-6. DOI: 10.1007/978-3-540-46360-3.

[69] S. Quezel, F. Tcheou, J. Rossat-Mignod, G. Quezel, and E. Roudaut. "Magnetic structure of the perovskite-like compound $TbMnO_3$". In: *Physica B+C* 86-88 (1977), pp. 916–918. DOI: 10.1016/0378-4363(77)90740-9.

[70] J. Ren and J. Sirker. "Spinons and helimagnons in the frustrated Heisenberg chain". In: *Physical Review B* 85.14 (2012), pp. 1–5. DOI: 10.1103/PhysRevB.85.140410.

[71] G. Rose. "Beschreibung einiger neuen Mineralien des Urals". In: *Annalen der Physik* 124.12 (1839), pp. 551–573. DOI: 10.1002/andp.18391241205.

[72] G. Rose. "Ueber einige neue Mineralien des Urals". In: *Journal fuer Praktische Chemie* 19 (1840), pp. 459–468. DOI: 10.1002/prac.18400190179.

[73] W. Rudin. *Principles of Mathematical Analysis*. McGraw-Hill, 1976, p. 342. ISBN: 007054235X.

[74] S. Sachdev and B. Keimer. "Quantum criticality". In: *Physics Today* 64.2 (2011).

[75] M. Saito, R. Higashinaka, and Y. Maeno. "Magnetodielectric response of the spin-ice $Dy_2Ti_2O_7$". In: *Physical Review B* 72.14 (2005), p. 6. DOI: 10.1103/PhysRevB.72.144422.

[76] T. Sakakibara, T. Tayama, Z. Hiroi, K. Matsuhira, and S. Takagi. "Observation of a liquid-gas-type transition in the pyrochlore spin ice compound $Dy_2Ti_2O_7$ in a magnetic field". In: *Physical review letters* 90.20 (2003), p. 207205. DOI: 10.1103/PhysRevLett.90.207205.

[77] C. Sawyer and C. Tower. "Rochelle Salt as a Dielectric". In: *Physical Review* 35.3 (1930), pp. 269–273. DOI: 10.1103/PhysRev.35.269.

[78] M. Schiebl et al. "Order-disorder type critical behavior at the magnetoelectric phase transition in multiferroic $DyMnO_3$". In: *Physical Review B* 91.22 (2015), p. 224205. DOI: 10.1103/PhysRevB.91.224205.

[79] F. Schrettle et al. "Relaxations as Key to the Magnetocapacitive Effects in the Perovskite Manganites". In: *Physical Review Letters* 102.20 (2009), pp. 1–4. DOI: 10.1103/PhysRevLett.102.207208.

[80] F. Schrettle et al. "Switching the ferroelectric polarization in the S=1/2 chain cuprate $LiCuVO_4$ by external magnetic fields". In: *Physical Review B* 77.14 (2008), pp. 1–6. DOI: 10.1103/PhysRevB.77.144101.

[81] R. D. Shannon. "Revised effective ionic radii and systematic studies of interatomic distances in halides and chalcogenides". In: *Acta Crystallographica Section A* 32.5 (1976), pp. 751–767. DOI: 10.1107/S0567739476001551.

[82] A. V. Shtyk and M. V. Feigel'man. "Dynamic Susceptibility of a Spin Ice near the Critical Point". In: *JETP Letters* 92.12 (2011), pp. 799–803. DOI: 10.1134/S0021364010240045.

[83] J. Sirker. "Thermodynamics of multiferroic spin chains". In: *Physical Review B* 81.1 (2010), p. 014419. DOI: 10.1103/PhysRevB.81.014419.

[84] J. Snyder et al. "Low-temperature spin freezing in the $Dy_2Ti_2O_7$ spin ice". In: *Physical Review B* 69.6 (2004), p. 064414. DOI: 10.1103/PhysRevB.69.064414.

[85] M. Subramanian, G. Aravamudan, and G. Subba Rao. "Oxide pyrochlores — A review". In: *Progress in Solid State Chemistry* 15.2 (1983), pp. 55–143. DOI: 10.1016/0079-6786(83)90001-8.

[86] L. E. Svistov et al. "New high magnetic field phase of the frustrated S = 1/2 chain compound $LiCuVO_4$". In: *JETP Letters* 93.1 (2011), pp. 21–25. DOI: 10.1134/S0021364011010073.

[87] H. Takatsu, K. Goto, and H. Otsuka. "Two-Dimensional Monopole Dynamics in the Dipolar Spin Ice $Dy_2Ti_2O_7$". In: *Journal of the Physical Society of Japan* 82 (2013), pp. 1–5. DOI: 10.7566/JPSJ.82.104710.

[88] T. Tanaka, H. Ishida, M. Matsumoto, and S. Wada. "Nuclear Magnetic Resonance Study on Pseudo One-Dimensional Antiferromagnet $LiCuVO_4$". In: *Journal of the Physical Society of Japan* 71.1 (2002), pp. 308–312. DOI: 10.1143/JPSJ.71.308.

[89] J. Toll. "Causality and the Dispersion Relation: Logical Foundations". In: *Physical Review* 104.6 (1956), pp. 1760–1770. DOI: 10.1103/PhysRev.104.1760.

[90] C. Uyeda, K. Sugiyama, and M. Date. "High Field Magnetization of Solid Oxygen." In: *Journal of the Physical Society of Japan* 54.3 (1985), pp. 1107–1115. DOI: 10.1143/JPSJ.54.1107.

[91] W. B. Weir. *Automatic measurement of complex dielectric constant and permeability at microwave frequencies*. 1974. DOI: 10.1109/PROC.1974.9382.

[92] F. Wöhler. "Ueber den Pyrochlor, eine neue Mineralspecies". In: *Annalen der Physik* 83.8 (1826), pp. 417–428. DOI: 10.1002/andp.18260830803.

[93] L. Yaraskavitch et al. "Spin dynamics in the frozen state of the dipolar spin ice material $Dy_2Ti_2O_7$". In: *Physical Review B* 85.2 (2012), 020410(R). DOI: 10.1103/PhysRevB.85.020410.

[94] B. Zappoli et al. "Anomalous heat transport by the piston effect in supercritical fluids under zero gravity". In: *Physical Review A* 41.4 (1990), pp. 2264–2267. DOI: 10.1103/PhysRevA.41.2264.

List of Figures

Danksagung

Wie alle wissenschaftlichen Arbeiten findet auch eine Promotion nicht in ihrem eigenen, abgeschlossenen Universum statt, sondern profitiert besonders vom Austausch mit Kollegen die an ähnlichen Materialien und Fragestellungen forschen. Daher möchte ich mich bei einigen Personen bedanken, die mir besonders geholfen haben.

Zunächst bedanke ich mich bei Prof. Dr. Joachim Hemberger für die Möglichkeit in seiner Arbeitsgruppe zu promovieren. Die Kombination von technischer Arbeit an der Kryostatentechnik und Programmierung von Messprogrammen zusätzlich zu der wissenschaftlichen Arbeit an interessanten Materialien hat mir sehr viel Spaß gemacht. Auch für die jederzeit mögliche Hilfe bei Problemen und der Diskussion der gemessenen Daten bedanke ich mich ganz besonders.

Prof. Dr. Markus Braden danke ich für die Zeit, die er sich genommen hat um meine Arbeit zu begutachten und sowohl ihm als auch Prof. Dr. Simon Trebst danke ich für die Teilnahme an meiner Prüfungskommission bei der Disputation.

Keine der Messungen hätte ohne gute Einkristalle durchgeführt werden können, die ich von verschiedenen Kollegen bekommen habe. Die beiden $TbMnO_3$ Proben – die erste ist bei einer Messung mit Magnetfeld verschwunden und konnte nicht mal als Pulverrest wiedergefunden werden – wurden von Tobias Cronert hergestellt. Für $LiCuVO_4$ wurden die Proben von Prof. Dr. Petra Becker-Bohatý bereitgestellt. Alle Kristalle der untersuchten Pyrochlore hat mir Dr. Martin Valldor für die Messungen in dieser Arbeit zur Verfügung gestellt.

Dr. Harald Kierspel danke ich für seine Einführung in die Mischkryostatentechnik zu Beginn meiner Arbeit sowie die fortwährende technische Unterstützung.

Dr. Markus Garst danke ich für seine geduldigen Erklärungen von allerlei Konzepten aus der theoretischen Seite der Physik, die sich so auch ein Experimentalphysiker erschließen konnte.

Den Mitarbeitern der Werkstätten des Instituts danke ich für die sorgfältige Herstellung der Probenhalter und Messelektronik die im Laufe der Arbeit weiterentwickelt wurden. Besonders Andreas Freimuth und Klaus Lehmann danke ich für ihre Unterstützung bei der technischen Umsetzung an den kniffligeren Stellen.

Allen Kolleginnen und Kollegen danke ich für die immer gute Atmosphäre, die es auch an zähen Tagen erleichtert hat produktiv zu sein und auch die gelegentlichen experimentellen Fehlschläge schnell zu verdrängen. Insbesondere gilt das natürlich für all diejenigen, mit denen ich im Laufe der Zeit das Büro 220 geteilt habe.

Partial publications

[1] C. P. Grams, M. Valldor, M. Garst, and J. Hemberger. "Critical speeding-up in the magnetoelectric response of spin-ice near its monopole liquid-gas transition." In: *Nature communications* 5 (2014), p. 4853. DOI: 10.1038/ncomms5853.

Other publications

[1] M.-R. Li et al. "Designing Polar and Magnetic Oxides: Zn_2FeTaO_6 - in Search of Multiferroics." In: *Journal of the American Chemical Society* 136.24 (2014), pp. 8508–11. DOI: 10.1021/ja502774v.

[2] M.-R. Li et al. "Magnetic-Structure-Stabilized Polarization in an Above-Room-Temperature Ferrimagnet." In: *Angewandte Chemie (International ed. in English)* 53.40 (2014), pp. 10774–10778. DOI: 10.1002/anie.201406180.

[3] M.-R. Li et al. "Mn_2FeWO_6 : a New Ni_3TeO_6 -Type Polar and Magnetic Oxide". In: *Advanced Materials* (2015), pp. 1–5. DOI: 10.1002/adma.201405244.

[4] M.-R. Li et al. "Polar and magnetic Mn_2FeMO_6 (M=Nb, Ta) with $LiNbO_3$-type structure: high-pressure synthesis." In: *Angewandte Chemie (International ed. in English)* 52.32 (2013), pp. 8406–10. DOI: 10.1002/anie.201302775.

[5] B. S. de Lima et al. "Interplay between antiferrodistortive, ferroelectric, and superconducting instabilities in $Sr_{1-x}Ca_xTiO_{3-\delta}$". In: *Physical Review B* 91.4 (2015), p. 045108. DOI: 10.1103/PhysRevB.91.045108.

[6] D. Niermann et al. "Critical Slowing Down near the Multiferroic Phase Transition in $MnWO_4$". In: *Physical Review Letters* 114.January (2015), pp. 1–5. DOI: 10.1103/PhysRevLett.114.037204.

[7] D. Niermann et al. "Domain dynamics in the multiferroic phase of $MnWO_4$". In: *Physical Review B* 89.13 (2014), p. 134412. DOI: 10.1103/PhysRevB.89.134412.

[8] M. Retuerto et al. "Polar and Magnetic Layered A-Site and Rock Salt B-Site-Ordered $NaLnFeWO_6$ (Ln = La, Nd) Perovskites." In: *Inorganic chemistry* 52.21 (2013), pp. 12482–12491. DOI: 10.1021/ic401491y.

Abstract

In this thesis the critical dynamics of several magnetoelectric compounds at their phase transition were examined. Mostly measurements of the dielectric properties in the frequency range of below 1 Hz up to 5 GHz were employed to evaluate the critical exponents for both magnetic field and temperature-dependent measurements. Most of the materials that are part of this work show anomalous behavior, especially at very low temperatures where quantum fluctuations are of the order of or even dominate those induced thermally. This anomalous behavior manifests in different forms.

In $Dy_2Ti_2O_7$ we demonstrate the existence of electric dipoles on magnetic monopoles. Here the dynamics at the critical endpoint located at 0.36 K and in a magnetic field of 1 T parallel to the [111] direction are of special interest. At this critical endpoint the expected critical slowing down of the dynamics could not only not be observed but instead the opposite, critical speeding-up by several orders of magnitude, could be demonstrated. Furthermore, we show that the phase diagram of $Dy_2Ti_2O_7$ in this field direction can be reproduced solely from the dynamical properties, for example the resonance frequency of the observed relaxation that is connected to the monopole movement. Away from this point of the phase diagram the dynamics are slowing-down with reduction of temperature as one would expect. Additional measurements on $Y_2Ti_2O_7$, a structurally identical but non-magnetic material, show only slowing down with reduction of temperature and no additional features. A possible explanation for the observed critical speeding-up is a coherent movement of magnetic monopoles close to the critical field that increases the resonance frequency by reducing the damping of the process.

$LiCuVO_4$ on the other hand behaves normally at its phase transition as long as the temperature is higher than 0.4 K. In this temperature regime the dynamics show critical slowing-down analogous to classical ferroelectric materials. This analogy extends also towards higher frequencies where the permittivity displays a 'dispersion' minimum that is temperature-dependent but of the order of 2 GHz. Below 0.4 K the observed behavior changes drastically. Here we found no longer relaxational behavior but instead an excitation with very low energy. This low energy excitation was predicted by theory and is caused by nearly gapless soliton excitations within the 1D Cu^{2+} chains of $LiCuVO_4$.

Finally, in $TbMnO_3$ the dynamics of the phase transition into the multiferroic phase was observed at roughly 27 K, a much higher temperature compared to the other materials. Here the expected critical slowing-down was observed, even though in low-frequency measurements this transition into the ferroelectric phase is overshadowed by the so-called *c*-axis relaxation. Therefore, only frequencies above 1 MHz could be used to determine the critical exponents for both temperature- and magnetic-field-dependent measurements. This was done for both the peak frequency ν_p as well as the relaxation strength $\Delta\varepsilon$ and resulted in values of $\gamma_{\nu_\mathrm{p}} = 0.8(2)$ and $\gamma_{\Delta\varepsilon} \gtrsim 1$ where the latter is subject to an error due to the choice of the offset correction. In $TbMnO_3$ an electromagnetic soft-mode with small optical weight causes the observed fluctuations, similar to the case of multiferroic $MnWO_4$.

Kurzzusammenfassung

Im Rahmen dieser Arbeit wurde die kritische Dynamik verschiedener magnetoelektrischer Materialien an ihren Phasenübergängen untersucht. Hauptsächlich wurden Messungen der dielektrischen Eigenschaften im Frequenzbereich von unter 1 Hz bis 5 GHz verwendet um die kritischen Exponenten in Ahängigkeit von sowohl Temperatur als auch Magnetfeld zu bestimmen. Die meisten untersuchten Materialien haben, besonders im Bereich der tiefen Temperaturen, bei denen Quantenfluktuationenen dominieren, anormales Verhalten gezeigt, das sich auf verschiedene Art äußert.

Bei $Dy_2Ti_2O_7$ wurde gezeigt, dass magnetische Monopole elektrische Dipole besitzen. Von besonderem Interesse ist bei diesem Material die Dynamik am kritischen Endpunkt bei 0.36 K und einem Magnetfeld von 1 T in [111] Richtung. In der Nähe dieses kritischen Endpunktes wurde nicht die erwartete Verlangsamung der Relaxationsprozesse (*critical slowing down*) beobachtet, sondern das Gegenteil, die Relaxation erfolgt um mehrere Größenordnungen schneller (*critical speeding up*). Zusätzlich wurde gezeigt, dass das Phasendiagramm von $Dy_2Ti_2O_7$ bei dieser Orientierung des Magnetfelds allein aus den Messungen der dynamischen Eigenschaften, wie beispielsweise der mit der Bewegung der Monopole verbundenen Resonanzfrequenz ν_p, reproduziert werden kann. Abseits dieses Punktes im Phasendiagram verlangsamt sich die Dynamik wie erwartet, wenn die Temperatur reduziert wird. Zusätzliche Messungen an $Y_2Ti_2O_7$, einem unmagnetischen isostrukturellen Material, zeigen lediglich das Verlangsamen der Dynamik. Eine mögliche Erklärung für das beobachtete critical speeding up ist eine kohärente Bewegung der magnetischen Monopole in der Nähe des kritischen Feldes. Dadurch würde die Dämpfung der Relaxation reduziert und die Resonanzfrequenz ansteigen.

$LiCuVO_4$ hingegen verhält sich für Temperaturen oberhalb von 0.4 K wie erwartet. Hier zeigt die Dynamik das critical slowing down analog zu klassischen Ferroelektrika. Diese Analogie erstreckt sich auch auf Hochfrequenzmessungen, bei denen das temperaturabhängige 'Dispersions'-Minimum in der Permittivität bei etwa 2 GHz beobachtet wird. Bei Temperaturen unterhalb von 0.4 K ändert sich das beobachtete Verhalten deutlich. Hier wird keine Relaxation beobachtet, sondern eine niederenergetische Anregung, wie sie theoretisch vorhergesagt wurde. Die Ursache dieser Anregung sind Solitonen, Anregungen innerhalb der eindimensionalen Cu-O Ketten in $LiCuVO_4$.

Zuletzt wurde die Dynamik von $TbMnO_3$ an seinem multiferroischen Phasenübergang bei etwa 27 K untersucht. Dort wurde das erwartete critical slowing down beobachtet, obwohl der Phasenübergang bei niedrigen Frequenzen von der sogenannten *c*-Achsen-Relaxation überschattet wird. Daher konnten nur Frequenzen oberhalb von 100 kHz verwendet werden um die kritischen Exponenten temperatur- und magnetfeldanhängig zu bestimmen. Diese wurden sowohl für die Frequenz des Maxmums ν_p als auch aus der Relaxationssträrke $\Delta\varepsilon$ bestimmt und liefern als Ergebnis die Werte $\gamma_{\nu_\mathrm{p}} = 0.8(2)$ beziehungsweise $\gamma_{\Delta\varepsilon} \gtrsim 1$, wobei letzteres einem erhöhten Fehler durch die Wahl des abzuziehenden Untergrundes unterliegt. Die beobachtete Fluktuationsdynamik in $TbMnO_3$ wird von einer elektromagne-

tischen Mode verursacht, die am Phasenübergang weich wird, wie es bereits bei dem Multiferroikum $MnWO_4$ beobachtet wurde.

Erklärung

Gemäß der Promotionsordnung der Mathematisch-Naturwissenschaftlichen Fakultät der Universität zu Köln § 4 Abs. 1 Nr. 9 erkläre ich:

Ich versichere, dass ich die von mir vorgelegte Dissertation selbständig angefertigt, die benutzten Quellen und Hilfsmittel vollständig angegeben und die Stellen der Arbeit - einschließlich Tabellen, Karten und Abbildungen -, die anderen Werken im Wortlaut oder dem Sinn nach entnommen sind, in jedem Einzelfall als Entlehnung kenntlich gemacht habe; dass diese Dissertation noch keiner anderen Fakultät oder Universität zur Prüfung vorgelegen hat; dass sie - abgesehen von unten angegebenen Teilpublikationen - noch nicht veröffentlicht worden ist sowie, dass ich eine solche Veröffentlichung vor Abschluss des Promotionsverfahrens nicht vornehmen werde.

Die Bestimmungen der Promotionsordnung sind mir bekannt.

Die von mir vorgelegte Dissertation ist von Prof. Dr. Joachim Hemberger betreut worden.

Christoph Grams